Analysis for Jet Fluctuation and Acoustic Radiation of Flute-Like Instruments

(エアリード楽器のジェット変動と音響放射に関する解析)

January, 2022

Doctor of Philosophy (Engineering)

Kimie Onogi
(小野木 君枝)

Toyohashi University of Technology

Abstract

To elucidate the mechanism by which the radiated sound changes with conditions of blowing and the instrument's shapes, this study performed numerical simulations and experiments simulating actual conditions. Focusing on the interaction between the airflow and the sound of flute-like instruments, this study proposed an analytical method for sound changes taking into account the jet deflection observed in the simulations. The effects of the blowing conditions on the jet behaviors and the radiated sound were also shown.

First, an analytical method for quantifying jet fluctuations was proposed to determine conditions of blowing or instrument shapes that mainly contributes to sound changes. This method was first utilized for the recorder, which has fewer variable parameters of blowing than the flute. To decompose jet fluctuations into an acoustic and a fluid dynamic oscillations, a formula represents jet fluctuations was proposed by modifying the Fletcher's formula (*JASA*, 1976) based on the jet fluctuations predicted by direct aeroacoustic simulations. This formula takes into account the initial amplitude at the exit and the inclination of jet fluctuation center (time-averaged jet displacement), which were observed in the simulations. The jet fluctuations in the simulations were represented by this formula, and the characteristics of fluctuations (the convection velocity, the amplification rate, the acoustic feedback effects, and the actual jet offset) were quantified. As a result, the difference in the acoustic mode predominancy between the subject recorders seems to be produced by the difference in the amplification rate probably due to a difference in the shapes of jet exit (straight- or arch-shaped). This analytical method seems to be useful for investigating mechanisms of sound changes.

Second, the effects of the jet angle (angle between the jet and the mouth opening) on the harmonic structure and their mechanism were shown for the flute. Blowing parameters were varied independently using an artificial blowing device with reference to the actual blowing condition measured for a flute player. The periodical fluctuation of jet was obtained by phase-averaging measured velocity with a hot-wire anemometer. The radiated

sound showed that, within the practical range of the blowing parameters, the effects of the jet angle on the harmonic structure is less than those of the jet offset and almost equal with those of the flow rate and comparably larger than the exit-edge distance. The effect of the jet angle on timbre seems to be an important consideration for flute players. The flow field showed that, with increasing the jet angle (the jet direction approaches vertical to the mouth opening), the jet fluctuation center was found to incline more inward. This inclination seems to occur because of the deceleration of the fluctuation of jet when changing direction from inward to outward. Due to this inclination, the actual jet offset was found to decrease with increasing the jet angle. This decrease of the actual jet offset was almost consistent with the change of harmonic structure with the jet angle. The ratio of amplitudes of the second and the third mode of jet oscillations was found to affect little. The variation of the harmonic structure with the jet angle is mainly caused by the change of the actual jet offset due to the inward inclination of jet fluctuation center.

Third, the effects of the geometrical relationship between the jet direction and the edge on the jet fluctuations and the sound were investigated by direct aeroacoustic simulations on the flute. The mechanism of the change of the jet fluctuation was investigated from the instantaneous jet direction. From the estimation of the instantaneous jet direction, as the jet offset increases, the jet is expected to be affected by the high pressure around the edge wall from a more upstream position. The visualization showed that the shear layer of the jet is separated and does not fluctuate under the condition of a larger jet offset. This is probably due to the disturbance by the high pressure. As a result of this separation of jet, the higher modes of fluctuation are suppressed, affecting the harmonic structure. Also, as the jet angle increases, the distance between the jet and the inner wall of edge is estimated to decrease; thus, the jet seems to decelerate more, affected by the high pressure near the wall. Due to the effects of the wall, the jet fluctuation changes, resulting in a change of the harmonic structure. To clarify the cause of the change of the jet fluctuation, estimation of the geometrical relationship between the instantaneous jet direction and the edge inclination seems to be useful.

Contents

Nomenclature

Symbol	Description	Unit
A	Amplitude of a jet fluctuation component	mm
b	Half width of jet	mm
d	Jet width in the spanwise direction	mm
f	Frequency	Hz
$\mathscr{F}$	Force produced by volume flow	N
h	Jet exit height (thickness)	mm
i	Imaginary number ($= \sqrt{-1}$)	-
k	Wave number	-
l	Exit-edge distance (the distance from the jet exit to the edge)	mm
L	Resonator length	mm
n	Oscillation mode	-
p	Pressure	Pa
$\bar{p}$	Time-averaged pressure	Pa
p'	Fluctuation component of pressure ($= p - \bar{p}$)	Pa
$\mathscr{P}$	Acoustic power	W
q	Volume flow	mm^3/s
Q	Flow rate	L/min
Re	Reynolds number	-
S	Cross-sectional area	mm^2
Str	Strouhal number	-
t	Time	s
T	Oscillation period	s
U	Streamwise velocity	m/s
$\bar{U}$	Time-averaged streamwise velocity	m/s
U_0	Cross-sectional averaged streamwise velocity at the jet exit	m/s
V	Transverse velocity	m/s

W	Spanwise velocity	m/s
x	Streamwise direction defined geometrically	-
x_j	Streamwise direction defined based on the reference jet direction	-
y	Vertical direction defined geometrically	-
y_j	Vertical direction defined based on the reference jet direction	-
$y_{j,e}$	Jet offset (Relative height of the reference jet direction with respect to the edge)	mm
$y_{a,e}$	Actual jet offset	mm
Y	Admittance	S
z	Spanwise direction defined geometrically	-
z_j	Spanwise direction defined based on the reference jet direction	-
Z	Impedance	Ω

Greek Symbol	**Description**	**Unit**
α	Amplification rate of jet	-
ΔSPL	differential SPL of the second to third harmonic (ΔSPL≡ SPL_2-SPL_3)	dB
η	Jet displacement	mm
$\bar{\eta}$	Jet fluctuation center (Time-averaged displacement of jet)	mm
θ_j	Jet angle	°
θ_i	Inclination angle of reference jet direction with respect to the normal direction of the reference line of jet exit	°
λ	Wavelength	mm
ν	Kinematic viscosity	m^2/s
ξ	Acoustic particle displacement	mm
ρ	Air density	kg/m^3
ω	Angular velocity	rad/s

Subscript	Description
a	Actual
aco	Acoustic
amp	Amplitude
ap	Acoustic particle
b	Blowing
c	Convection
e	Edge
Err	Error
fluid	Fluid dynamic
i	incline
in	Inner wall of the edge
j	Jet
m	Mouth (window) of an instrument
max	Maximum
md	Momentum (pressure) drive
min	Minimum
mo	Mouth opening
out	Outer wall of the edge
p	Pressure
pr	Primary
pt	Measured value by pitot-tube
r	Resonator
ref	Reference
vd	Volume-flow drive
0	Cross section of jet exit
1, 2, 3	First, second, third mode

Acknowledgments

I would like to express my gratitude for the cooperation of many people in this research.

Prof. Akiyoshi Iida from TUT (Toyohashi University of Technology) has provided a precious opportunity to start research on aeroacoustics of the flute in this laboratory. His understanding on this research has been an essential factor in carrying out this research. I am also grateful that he has provided the environment and suggestions for making this research fruitful.

Associate Prof. Hiroshi Yokoyama from TUT has provided a CFD program for the direct aeroacoustic simulation. In carrying out this research, he has given me detailed and insightful suggestions through so many discussions. I would like to express my appreciation for his cooperation.

Prof. Yuji Nakamura from TUT and Prof. Chisachi Kato from Institute of Industrial Science, The University of Tokyo, the members of examination committee of this dissertation, gave me valuable comments to reconstruct the studies I have been involved in as a single dissertation. Prof. Yuji Nakamura, the chairperson of the committee, organized the committee and gave me much advice on the preparation for the examination. I would like to thank them for their support.

I would also like to take this opportunity to thank members of our laboratory. Ai Natsubori collaborated on the experiments. Her careful experiments contributed greatly to this research. Assistant prof. Tsukasa Yoshinaga has cooperated the discussions and helped the preparation for the examination. Kyoko Suzuki, secretary of our laboratory, has supported our research environment and also encouraged me. Our lab members have shared discussions on aeroacoustics and helped equipment management for experiments and simulations.

Yamaha Corporation has provided the artificial blowing device. Discussions with engineers from Yamaha have been always interesting and helped to improve this research.

In addition to their cooperation, I would like to express my great appreciation to my husband, Tomohiro Degawa from Nagoya University. As a researcher of computational

fluid dynamics, he has given me general advice in carrying out this research.

1. Introduction

1.1. Overview of Flute-Like Instruments

Flute-like (flue, air-reed) instruments includes the flute, the recorder, organ pipe, the shakuhachi and panpipes. This kind of instrument does not have a reed. When a player blows air into a flute-like instrument, the sound is produced. This kind of instruments have extremely ancient origin and date back to B.C. [1]. Various types of flute-like instruments have been developed in their long history over the world. For example, some use a windway (flue channel) to form the air (see Fig. 1.1 (a)), like the recorder and an organ pipe, while some use the player's lips (see Fig. 1.1 (b)), like the flute and the shakuhachi. Some are held vertically, like the recorder and the shakuhachi, while some are held horizontally, like the flute [2].

The produced sound depends on playing methods and instrument models. For players, the accurate control of pitch, timbre, and dynamics (the variation in loudness in music) is an essential technique. In case of the flute, the pitch is controlled by changing fingering (opening and closing the tone holes with player's fingers) or changing the speed with the same fingering, like C5 and C6. The timbre and dynamics are controlled by modifying the shapes of lips. Since the control of the air and the formation of embouchure are important considerations for flute playing, playing methods have been studied by various players [3, 4]. Besides playing methods, the shapes of instruments affect the sound, e.g., shapes around the embouchure hole, the position of the head cork affect the pitch and the timbre [2]; therefore, even after the invention of the basic design of the modern flute by Boehm [5] in the 19th century, instrument makers have continued to refine the designs, and numerous models have been released. In addition to players and makers, musical acoustics in flute-like instruments have been studied by researchers across fluid dynamics and acoustics [2, 6-89, 102, 103]. Subsequent sections describe the sound generation mechanism and investigations on conditions of blowing or instrument shapes based on the preceding studies.

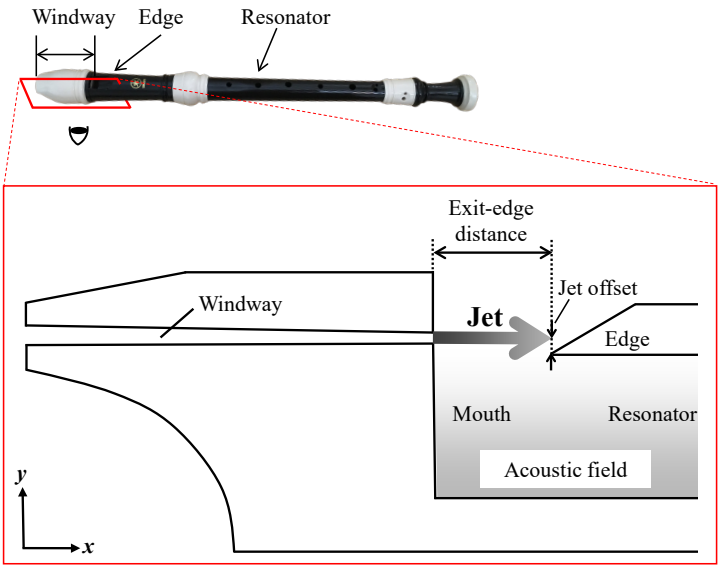

(a) Recorder

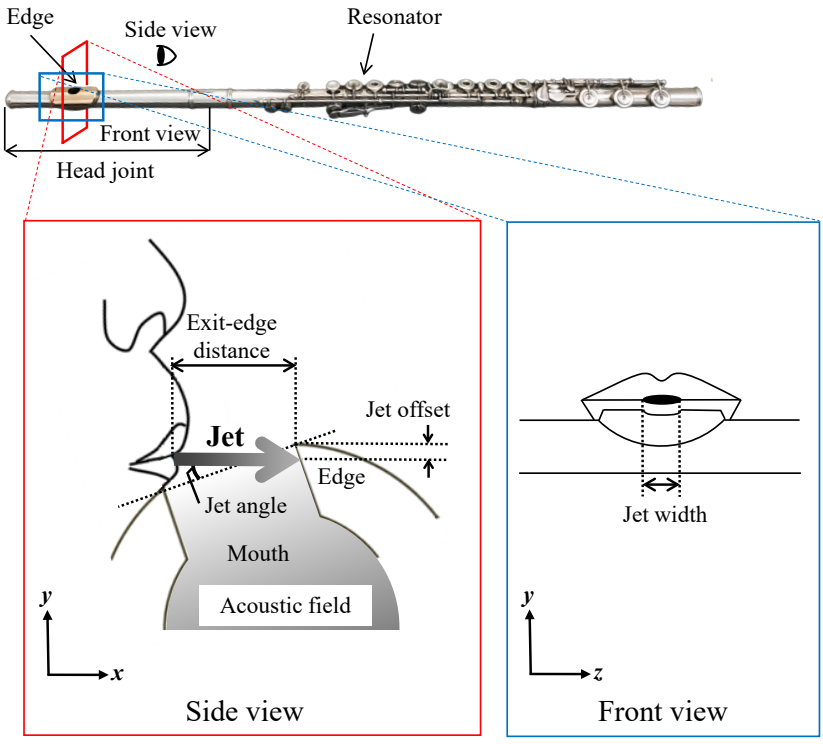

(b) Flute

Figure 1.1 Feedback loop between jet and acoustic field.

1.2. Feedback Loop of Jet and Acoustic Field in Flute-Like instruments

As outlined in Sec. 1.1, in flute-like instruments, the sound is produced by the mutual interaction between the air-jet and the acoustic field in the resonator. The jet emerges from the exit, passes through an opening in the resonator (mouth or window) while fluctuating vertically and periodically, and strikes against the edge. The vertical fluctuations of the jet amplify [6, 7] and delay from the exit to the edge [8, 9, 10] (see Fig. 1.2(a)). The pressure in the resonator also fluctuates periodically. If the jet reaches the edge and enters into the resonator when the pressure in the resonator becomes high, the jet promotes compression of the air in the resonator, and the high pressure in the resonator is further intensified. This phase relation is the optimum for the acoustic power generation [11]. To form this phase relation, the time delay of the jet fluctuation from the exit to the edge is to be almost half a period [12, 13, 14, 15] (see 2.2.1.A). Also, the acoustic oscillations in the resonator induce initial fluctuations of the jet around the exit, which is called acoustic feedback. Then, the feedback loop at one period of a resonance frequency is formed [2, 16, 17] (see Fig. 1.2(b)).

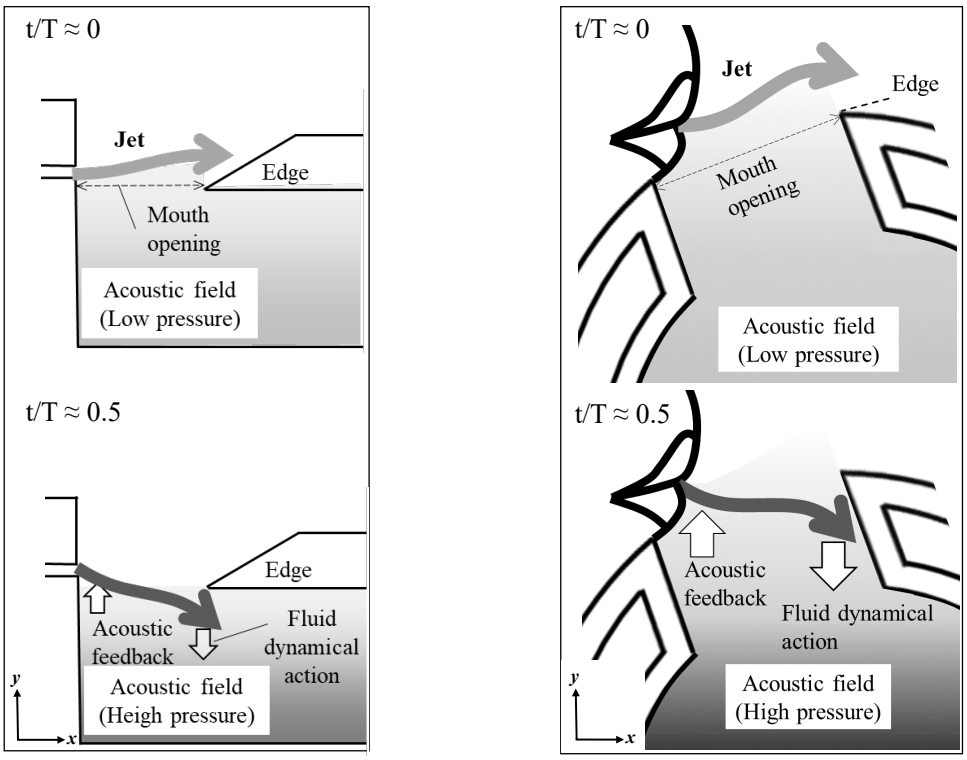

(a-1) Recorder (a-2) Flute

(a) Jet-acoustic field interaction

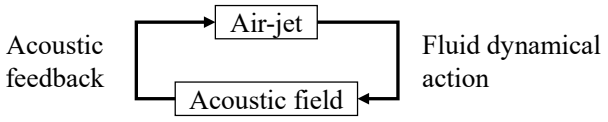

(b) Feedback loop

Figure 1.2 Feedback loop between jet and acoustic field.

1.3. Investigations on Jet Fluctuations

Since the jet fluctuations affect the sound generation in flute-like instruments, they have been investigated by theoretical models, experiments, and simulations.

1.3.1. Numerical Modeling

The jet fluctuations have been formulated on the basis of Rayleigh [18]'s analysis for the instability [9, 19, 20]. Fletcher *et al*. [9] proposed a semi-empirical formula, which

decomposes the jet oscillations at the fundamental mode into two oscillation components: the spatially uniform oscillation with the acoustic oscillations in the resonator, and the spatially propagating oscillation due to the jet instability produced by the acoustic feedback. Near the edge ($x = l$), the amplitude of the spatially propagating oscillation is generally much greater than that of the spatially uniform oscillation; thus, the spatially uniform oscillation can be ignored [9]. De la Cuadra [20] reduced a formula to only a spatially propagating oscillation. The formula by Fletcher *et al*. [9] and de la Cuadra [20] have been confirmed to represent jet oscillations in their experimental results [9, 20].

1.3.2. Experiments

Values of the parameters in the formulas have been estimated by experiments. These estimations allow to quantify jet fluctuations. Thwaites *et al*.'s [21, 22] estimated the convection velocity and the amplification ratio by pressure measurements with a pitot-tube, while Yoshikawa [23] and de la Cuadra [20] estimated them by jet visualizations. De la Cuadra [20] also estimated the initial amplitude of jet. The Fletcher *et al*. [9]'s formula assumes that the initial amplitude of jet is zero and that the initial amplitude of the spatially propagating oscillation is equals to the amplitude of the acoustic particle displacement. The initial amplitude of the spatially propagating oscillation has not yet been measured; however, the measurement for the initial amplitude of the spatially propagating oscillation seems to be useful to quantify the acoustic feedback effect on the jet. Also, the existing formulas assume a straight jet flow, while the jet visualizations in flute-like instruments [24, 25, 26] have observed that the jet inclines during traveling. From these measurements, the formulas seem to require further modifications to represent the actual jet fluctuations more precisely.

1.3.3. Simulations

To predict the jet fluctuations and the generated sound, the following simulations have been performed.

- **Time-domain simulations based on models for flute-like instruments** [13, 27, 28, 29, 30, 31]

In the simulations by Verge *et al*. [27], the jet fluctuations, the sound sources, and the energy loss by the vortex shedding are numerically modeled, and flute-like instruments are represented by a one-dimensional model.

- **Numerical simulations based on computational fluid dynamics (CFD)** [32, 33, 34, 35, 36, 37]

To perform simulations based on the governing equations for fluid, the simulations generally require taking into account of the compressibility. This is because that the flow and the acoustic field in flute-like instruments form the feedback loop. Yokoyama *et al*. [32, 33, 34] have performed direct aeroacoustic simulations based on the governing equations for compressible fluid: the continuity equation, the Navier-Stokes equations, and the energy conservation equation.

These CFD-based simulations for flute-like instruments require enormous computer resources because of the spatial and the temporal scale gaps between the acoustical and the fluid dynamical phenomena: the wavelength of sound wave ($\sim 1\ m$) and jet fluctuations ($\sim 1\ mm$), the sound speed ($\approx 340\ m/s$) and the jet velocity ($\approx 30\ m/s$). Owing to the resent technologies of super computers, various CFD-based simulations have been applied for flute-like instruments - for example, three-dimensional direct aeroacoustic simulations for recorders [35] and a piccolo [36] by Giordano and recorders [32, 33, 34] by Yokoyama *et al.*, two- and three- dimensional compressible LES for flute-like instrument models by Miyamoto *et al*. [37].

These simulations allow to obtain the jet fluctuations precise enough to analyze the effects of blowing conditions or shapes on the jet fluctuations and the sound. Giordano [35] analyzed the effects of chamfers on the transient state of sound generation in recorders. Yokoyama *et al.* [33] analyzed the effects of shapes around the windway exit

on the acoustic mode predominancy of recorders. These simulations may also allow to refine the formula for the jet fluctuations to quantify jet fluctuations more precisely. This refinement seems to be useful to elucidate mechanism whereby the sound changes with conditions of blowing or shapes.

1.4. Investigations on Conditions of Blowing and Instrument's Shapes

The produced sound depends on conditions of blowing or instrument's shapes. This subsection describes the effects of conditions and how players control these conditions.

1.4.1. Effects of Blowing Parameters on Sound

To investigate effects of the conditions on the sound, the conditions are decomposed into geometrically independent parameters and the jet velocity. Figure 1.1 illustrates the definitions of these parameters for the recorder [34] and the flute [38, 39] in this study. The jet thickness is the thickness of the jet at the exit, the jet angle is the angle between the mouth opening and the jet, the exit-edge distance is the distance from the jet exit to the edge, the jet offset is the relative height of jet fluctuation center from the edge, and the jet width is the width of the exit in the spanwise direction. In some studies, the blowing pressure (p_b) is investigated instead of the jet velocity at the exit (U_0), where U_0 can be estimated from p_b using Bernoulli's low: $p_\mathrm{b} = (1/2)\rho U_0^2$. The variable parameters for players depend on the instruments. For the flute, which does not have a windway, players can vary geometrical blowing parameters, like the jet angle, the jet offset, the jet thickness, and the exit-edge distance, in addition to the jet velocity. For the recorder, these geometrical blowing parameters are fixed by the instrument.

Effects of the above-mentioned parameters on the pitch, timbre, and dynamics have been respectively investigated in terms of the fundamental frequency, the harmonic structure (relative sound pressure levels between harmonics [40]), and the sound pressure level. These investigations have been conducted through acoustic excitation experiments

by Coltman [41], artificial blowing experiments by Ando [38, 42], calculations by Fletcher [43]. The effects of the parameters and the mechanisms whereby they affect the sound are summarized below.

· **Fundamental Frequency**

Coltman [8], Ando [38], and Fletcher [43] showed that the fundamental frequency increases and decreases with the jet velocity and the exit-edge distance, respectively. The mechanism for these changes has been explained from the phase condition between the jet and the pressure oscillations (see Sec. 2.2.1.A). Due to the phase condition, the fundamental frequency jumps to another register when the jet velocity increases above (or decreases below) a threshold. The threshold has been shown to depend on the shapes of instruments through artificial blowing experiments by Ségoufin *et al*. [44] and direct aeroacoustic simulations by Yokoyama *et al*. [33] and Onogi *et al*. [34]. Sawada *et al*. [45] showed that the jet angle also affects the transitions of the sounding mode by artificial blowing experiments. These changes of the fundamental register is accompanied by hysteresis [2, 28, 29, 30, 46]. Terrien *et al*. [28] conducted time-domain simulations and artificial blowing experiments, in which the blowing pressure was dynamically controlled [46], to show that the threshold depends on the temporal changes of the blowing pressure.

For the flute, the player's face inclination [48] and the area that the lower lip covers the mouth opening [41, 48] have been also shown to affect the fundamental frequency because they affect the radiation impedance around the mouth. Ernoult *et al*. [47, 48] formulated the radiation impedance taking into account of the face inclination and the mouth opening area [49].

· **Harmonic Structure**

The jet offset has been theoretically and experimentally shown to affect the harmonic structure due to the temporal changes of the volume flow into the resonator (see Sec.2.3). Ando [38] compared the effects of blowing parameters on the harmonic structure of a

flute, showing that the jet offset, the jet velocity and the exit-edge distance affect the harmonic structure more than the jet angle; however, quantitative results have not yet been demonstrated.

- **Sound Pressure**

The exit-edge distance and the jet velocity have been theoretically and experimentally shown to affect the sound pressure because they change the jet admittance (or impedance) for acoustic power generation (see Sec. 2.2.1.A) [8, 50]. Ando's experiments [38] for a flute showed that the jet width also affects the sound pressure. This seems to because that, with increasing the jet width, the lip aperture area increases, which increases the volume flow into the acoustic field (see Sec. 2.2.1) [50, 51].

1.4.2. Control of Blowing Conditions by Players

The actual control of the blowing conditions has been measured for players [20, 41, 52, 53, 54]. Fletcher [52] measured the blowing pressure, the exit-edge distance, and lip aperture shapes of four flute players playing notes in four registers. In his measurement, the blowing pressure was measured by inserting a catheter tube into the lip aperture, and the exit-edge distance and lip aperture shapes were measured from photographs. The photographed lip aperture shapes were almost oval with aspect ratios of 10:1 to 20:1. The jet width was maximized when playing low notes loudly, which was almost the same length as the spanwise length of the mouth opening. The jet width was reduced when producing soft sounds or playing high notes. The blowing pressure and the exit-edge distance were respectively increased and decreased with increasing pitch. The similar control of the blowing pressure and the exit-edge distance were also observed in the measurements by Vauthrin *et al*. [54], which measured the blowing conditions along with respiratory activities during a flute player playing a scale. To control the sound pressure level without affecting the fundamental frequency, flute players seem to control the volume flow into the acoustic field without affecting the jet velocity by opening or closing

the lip aperture [51]. To control the fundamental frequency, they seem to control the phase condition between the jet and the perssure by changing the blowing pressure and the exit-edge distance without affecting the volume flow. These measurements also show that players change several parameters during playing, while the effects of the parameters have been investigated independently.

1.5. Objective

The objective of this study is to elucidate the mechanism by which the radiated sound changes with jet conditions for flute-like instruments, which include blowing conditions, such as the jet angle in a flute, and the instruments shape, such as a windway in a recorder. Focusing on the interaction between the airflow and the sound, this study shows the following:

- An analytical method for quantifying jet fluctuations to clarify the mechanism for sound change.
- The effects of the blowing conditions on the jet behaviors and the radiated sound.

These objectives are based on the motivations below.

Identification of the conditions mainly contributing to sound change

This motivation is for practical use of investigations on the sounding mechanism. In actual performances by human players, the blowing parameters may not always change independently. Identifying blowing parameters that mainly contribute to the sound change may give a cue to improve playing method. In instrument designs, the shapes of multiple parts of instruments vary depending on the instrument's models. Identifying parts that mainly contribute to the sound change may allow to determine which of parts to be reshaped.

For these identifications, quantifying differences of jet fluctuations due to changes of conditions is useful. Direct aeroacoustic simulations probably allow refinement of the formula for jet fluctuations. This study proposes an analytical method that quantify jet

fluctuations with a formula based on results from direct aeroacoustic simulations. This method is proposed for the recorder, which does not include the jet angle as a parameter.

Enhancement of knowledge on how sound changes when conditions change

In addition to the identification, knowledge on how sound changes with conditions of blowing and shapes is useful for instruments playing and designing. Various studies have been conducted to clarify the effects of the blowing conditions on the sound; however, the changes of jet direction in actual flow fields as well as their mechanisms have not yet been fully clarified. When the jet direction is changed, the jet angle and the jet offset change. For these changes, the followings have remained unclear: the effects of jet angle on the harmonic structure, and effects of geometrical relationship between the jet direction and the edge on the jet fluctuations. The jet direction may relate to what flute players perceive as the air-stream direction, which have been considered to be an important consideration for flute players to control pitch and timbre [3, 4]. Also, by changing the jet direction, the angle between the jet and the edge wall changes; thus, the jet direction relates the design of the inclination of the edge wall. Therefore, this study focuses on the jet direction and shows its effects on the sound.

1.6. Thesis Layout

In Chapter 2, the sounding mechanism in flute-like instruments and the control of the radiated sound by players are explained with reference to preceding studies.

In Chapter 3, an analytical method for quantifying jet fluctuations is presented to identify conditions that mainly contribute to the difference in acoustic mode predominancy of two recorders. A formula representing jet fluctuations is proposed based on the results from direct aeroacoustic simulations. This study has been published in 2019 from The Journal of the Acoustical Society of America [34].

In Chapter 4, the effects of the jet angle on the harmonic structure are shown in

comparison with those of other blowing parameters (flow rate, jet offset, exit-edge distance) using an artificial blowing device. The mechanism whereby the harmonic structure changes with the jet angle is also shown in terms of the flow field measured with a hot-wire anemometer. This study has been published in 2021 from Acta Acust. [39].

In Chapter 5, the numerical methods in Chap. 3 are applied to a flute to show the effects of the jet direction on the jet behaviors and the radiated sound. Direct aeroacoustic simulations on the flute are performed under the conditions of two jet offsets. The discussions are applied to the effects of jet angle on the jet shown in Chap. 4.

In Chapter 6, main findings in Chap. 2-5 are summarized.

Please note that, in the current work, the effects of blowing conditions are investigated for the geometrically independent parameters, such as the jet angle and the jet offset, and the jet velocity. How humans actually control them is not included in the scope of this study. Also, the radiated sound is evaluated as follows.

- The sound pressure levels (SPLs) at about twice as high as the frequency of the first acoustic mode are discussed as the second acoustic mode. In the same way, the third and the higher modes are defined. The exact distinction between the second acoustical mode and the second harmonic of the first mode might be a problem for future study.
- The harmonic structure is evaluated from the difference of SPLs of the second to the third harmonic,

$$\Delta\mathrm{SPL}\ (\equiv \mathrm{SPL}_2 - \mathrm{SPL}_3), \tag{1.1}$$

  with reference to Ref. [42], which evaluates the difference of SPLs between even and odd harmonics.

2. Musical Acoustics in Flute-Like Instruments

2.1. Jet Fluctuations

2.1.1. Free Jet Flow

When there is no acoustic field, a free jet flows while entraining the surrounding fluid. At the exit, the initial velocity profile depends on the length and the shape of a channel, in which the boundary layer of the jet is formed on the wall surface [55]. The emitted jet spreads and decelerates as it travels (see Fig. 2.1). The potential core of the jet, where the central velocity is kept constant, vanishes in the development region. In the development region, the velocity profile of the jet is similar [55]; therefore, the velocity and the width are usually nondimensionalized with the maximum velocity and the halfwidth of the velocity profile, respectively. Connecting the outer edges of the velocity profiles in the development region, and extending the connected lines to upstream, the lines intersect at the virtual origin, x_0. This virtual origin is used for investigating jet behavior in the development region.

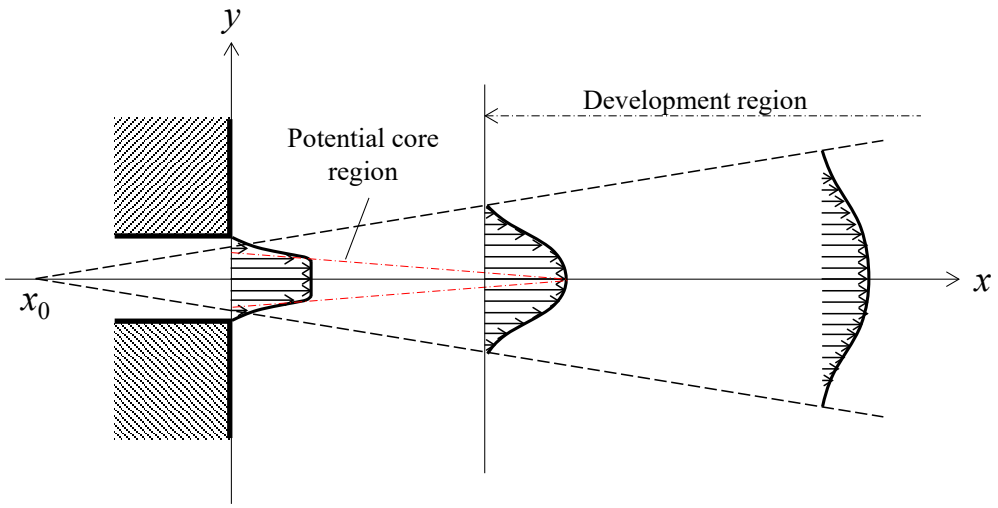

Figure 2.1 Velocity profile of free jet emitted from a channel.

2.1.2. Jet Instability

In flute-like instruments, the jet is disturbed by the acoustic oscillations in the resonator. Rayleigh [18] analyzed the instability of a jet subjected to acoustic disturbances. Under the assumption of the inviscid and incompressible two-dimensional fluid, the instability of the jet is derived from the equation for vorticity conservation around an acoustically disturbed jet. This jet instability is expressed by the following equation using a stream function [6, 16, 18, 19, 56]:

$$\left(U(y)-\frac{\omega}{\alpha}\right)\left(\frac{\partial^2\psi_{\mathrm{amp}}}{\partial y^2}-\alpha^2\psi_{\mathrm{amp}}\right)-\psi_{\mathrm{amp}}\frac{\partial^2 U(y)}{\partial y^2}=0. \tag{2.1}$$

Here, $U(y)$ is the streamwise velocity of an undisturbed jet, and the solution, ψ, is the following stream function:

$$\psi=\psi_{\mathrm{amp}}(y)e^{i(\omega t-\alpha x)}, \tag{2.2}$$

where ψ_{amp} is the amplitude of ψ, ω and α represent the temporal and the spatial periodicity, respectively.

There are two analyses for ψ: the spatial and the temporal analysis. The spatial analysis assumes a spatial development of the jet, in which the coefficients ω and α are a real and a complex ($\alpha=\mathrm{Re}(\alpha)+i\mathrm{Im}(\alpha)$) number respectively. The stream function ψ is written

$$\psi=\psi_{\mathrm{amp}}(y)e^{i\omega\left(t-\frac{\mathrm{Re}(\alpha)}{\omega}x\right)}e^{\mathrm{Im}(\alpha)x}. \tag{2.3}$$

As the jet travels in the streamwise direction (x), the fluctuation of the jet amplifies at the amplification rate $\mathrm{Im}(\alpha)$ and convects at the velocity $U_c=\omega/\mathrm{Re}(\alpha)$. On the other hand, the temporal analysis assumes a temporal development of the jet, in which the variables ω and α are a complex ($\omega=\mathrm{Re}(\omega)+i\mathrm{Re}(\omega)$) and a real number respectively. The stream function ψ is written

$$\psi = \psi_{\mathrm{amp}}(y) e^{-\mathrm{Im}(\omega)t} e^{-\alpha i\left(x-\frac{\mathrm{Re}(\omega)}{\alpha}t\right)}. \tag{2.4}$$

The values for α and ω have been analytically and experimentally studied [6, 18, 57, 58]. Freymuth [6, 57] experimentally investigated them by exciting acoustic disturbances with a loudspeaker and measuring velocity distributions with a hot-wire anemometer. The experimental results of α and ω were compared with those calculated from the spatial and the temporal analysis. As a result, a better agreement was found with the spatial analysis.

2.1.3. Formulas for Jet Fluctuations

The jet fluctuations in flute-like instruments have been formulated on the basis of the spatial analysis. Fletcher *et al*. [9] proposed a semi-empirical formula for the jet displacement:

$$\eta(x,t) = \left(\frac{V_{\mathrm{ap,amp}}}{\omega}\right)\left\{\sin(\omega t) - \cosh(\alpha x)\sin\left[\omega\left(t-\frac{x}{U_{\mathrm{c}}}\right)\right]\right\} \tag{2.5}$$

where $V_{\mathrm{ap,amp}}$ is the amplitude of the transverse acoustic particle velocity in the mouth: $V_{\mathrm{ap}}(t) = V_{\mathrm{ap,amp}}\cos(\omega t)$. Equation (2.5) superposes two components: the spatially uniform displacement (the first term) and the spatially propagating displacement (the second term). The first term represents the jet oscillation with the acoustic particle displacement $\xi(t) = \int_0^t V_{\mathrm{ap}}(s)\mathrm{d}s = \left(V_{\mathrm{ap,amp}} / \omega\right)\sin(\omega t)$. The second term represents the jet instability based on the spatial analysis, which is initiated by the acoustic oscillations at the exit ($x = 0$). The variables ω and α here are the angler velocity and the amplification rate that respectively correspond to ω and $\mathrm{Im}(\alpha)$ in the spatial analysis. Since the spatially uniform and the spatially propagating displacement respectively represent the jet oscillation due to the acoustic oscillation and the fluid dynamical jet instability, they are called the acoustic (η_{aco}) and the fluid-dynamic (η_{fluid}) jet

displacement in this study. The spatial and the temporal behaviors of the jet assumed by Eq. (2.5) are described below.

· **Spatial Behavior: Growth**

Although Rayleigh [18] assumes exponential growth of the jet, Eq. (2.5) uses $\cosh(\alpha x)$ to impose the boundary condition that the jet amplitude at the exit is zero ($\eta(0,t)=0$). Near the edge ($x=l$), the amplitude of the spatially propagating displacement is generally much greater than that of the spatially uniform displacement; thus, the spatially uniform displacement can be ignored [9].

· **Temporal Behavior: Phase of Jet and Pressure**

In Eq. (2.5), the jet oscillations at the distance x, $\eta(x,t)$, delays by $\omega x / U_c$ from those at the exit ($\eta(0,t)$) and the acoustic particle displacement $\xi(t)$. In standing waves, the phase of the pressure in the resonator ($p_r(t)$) delays $\pi/2$ from the acoustic particle velocity ($v_{ap}(t)$) [59]. Since the phase of $\xi(t)\left(=\mathrm{d}v_{ap}/\mathrm{d}t\right)$ also delays $\pi/2$ from $v_{ap}(t)$, $p_r(t)$ and $\xi(t)$ are in-phase. Hence, $\omega x / U_c$ also corresponds to the phase delay of $\eta(x,t)$ from $p_r(t)$. The phase relationship between the jet fluctuations at the edge ($\eta(l,t)$) and the pressure fluctuations ($p_r(t)$) affects the acoustic power generation [2, 51, 60]. The optimum phase relationship is described in Sec. 2.2.1.A.

Although the lack of physical background has been pointed out [2, 61], Eq. (2.5) has been confirmed to be in agreement with the experimental results by Fletcher *et al.*'s [9], except under low jet velocity conditions.

Some studies have proposed variations of formula for the jet displacement [19, 20]. Verge *et al*. [19] proposed a modified version of Eq. (2.5) based on the formula proposed by Powell [62]. De la Cuadra [20] reduced a formula to only a spatially propagating displacement:

$$\eta(x,t) = \eta_{0,\mathrm{amp}} e^{\alpha} e^{i\omega(t - x/U_c)} \tag{2.6}$$

where $\eta_{0,\mathrm{amp}}$ is the initial jet amplitude at the exit. This formula was fitted with the jet visualized by Schlieren method, and the values of $\eta_{0,\mathrm{amp}}$, U_c, and α were estimated [20, 63].

2.1.4. Characteristics of Jet Fluctuations

Values of the parameters in the formulas have been theoretically and experimentally estimated. In addition, jet fluctuation characteristics not included in the above-mentioned formulas have been also discussed.

- **Convection and Amplification**

The convection velocity (U_c) and the amplification rate (α) depend on the ratio of the wavelength and the jet thickness [2, 18]; therefore, U_c and α have been studied as functions of kh, where k and $h(=2b)$ are the wave number and the jet height (or thickness) respectively.

When imposing symmetrical or asymmetrical perturbations on both sides of the jet, varicose or sinuous oscillations appear on the jet (see. Fig. 2.2).

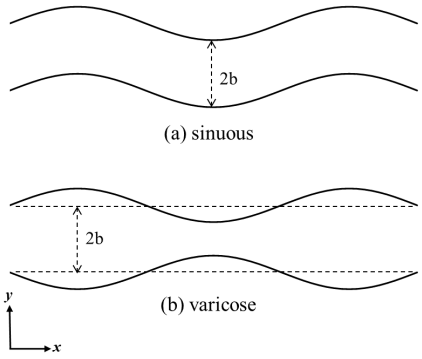

Figure 2.2 Spatial oscillation of jet: sinuous and varicose, where b is the half width of the jet.

Under a standard blowing condition of flute-like instruments, sinuous oscillations are dominant [2, 16]. Rayleigh's analysis [18] for inviscid fluid has been extended to sinuous oscillations, showing that U_c and α monotonically increase with kb.

Taking into account viscous effects, U_c and α for jets with shear layers, like jets with bell-shaped velocity profiles, have been calculated [6, 58, 64, 65]. The calculation by Drazin *et al.* [64] shows that the convection velocity monotonically increases with kb, while the amplification rate increases up to $\alpha b \approx 0.4$ in $kb < 0.6$ and decreases to $\alpha b = 0$ in $kb > 0.6$ like a convex curve with a peak at $kb = 0.6$. These calculations do not take into account other effects of viscosity on the jet, such as the spreading of the velocity profile, where the jets are assumed to keep the same velocity profiles during traveling. Fletcher and Thwaites [10, 21, 22] studied the effects of the spreading on U_c and α. They formulated U_c as a function of integration of the nondimensionalized momentum flux along a velocity profile, $J = M / \rho = \int_{-\infty}^{\infty} U^2 \mathrm{d}y$, which is assumed to be conserved along the jet. They estimated $U_c(J)$ by measuring jet velocities in an organ pipe with a pitot tube, showing that U_c decreases with $x^{-1/2}$. Based on the principles of similarity and self-preservation, the maximum velocity of the jet, $U_{max}(x)$, also decreases with $x^{-1/2}$ [66]. From these, the ratio of the convection velocity to the jet central velocity, $U_c / U_{max}(x)$ is estimated to be constant along the jet. Thwaites *et al.*'s obtained the jet velocity by pressure measurements with a pitot-tube, showing that $U_c / U_{max}(x)$ is almost 0.5 [21]. Their measurements for α showed that α increases up to a peak value $\alpha b = 0.5$ around $kb = 0.6$ and then decreases toward zero [22]. This tendency, a convex curve like behavior of αb with a peak around $kb = 0.6$, is consistent with the calculation for non-spreading jet [64]. Yoshikawa [23] conducted jet visualizations for organ pipes and showed that the convection velocity nondimensionalized with the maximum velocity at the exit, $U_c / U_{0,max}$, is estimated to be almost 0.4 near the midpoint between the exit and the edge.

The values of U_c and α have been shown to depend on channel geometries [20, 23, 67]. De la Cuadra [20] investigated the effects of channel length and chamfer shapes on

U_c and α by visualizing jets emitted into an acoustically disturbed field. Analysis from Schlieren images in $0.1 < \mathrm{Str}_h (\equiv fh / U = kb / \pi) < 1.1$ showed that $U_c / U_{0,\max}$ are respectively almost 0.5 and 0.3 for a short and a long channel and hardly change depending on chamfer shapes. As the channel gets longer, the shear layer of jet develops more due to viscosity. The convection velocity seems to depend on the shear layer formation of the jet [20, 67], rather than chamfer shapes. The image analysis also showed that α changes with Str_h like a convex curve, as observed in the calculations [58, 64] and the measurements [22]. The peaks of α were around $\alpha h \approx 0.6$ near $\mathrm{Str}_h = 0.4$ to 0.6, depending on chamfer shapes. The amplification rate seems to depend on chamfer shapes, rather than channel length [20].

· **Inclination of Jet Fluctuation Center**

The formulas for the jet fluctuations in Sec. 2.1.3, Eqs. (2.5) and (2.6) assume that the jet oscillates symmetrical with respect to the vertical center of the exit ($y = 0$), *i.e.*, the time-averaged value of η (jet fluctuation center) is always zero ($\overline{\eta} = 0$). However, due to the Coanda effect caused by the entrainment of the surrounding air, the pressure gradients around the jet seem to change the direction of jet near the edge [24, 68]. The changes of $\overline{\eta}$ in the streamwise direction have been observed in the visualizations for the jet in a recorder-like instrument [24, 25] and a stopped pipe [26]. Also, the jet fluctuation center possibly changes with increasing the jet velocity [68].

· **Initial Fluctuation Induced by Acoustic Feedback**

The acoustic oscillations around the exit produce initial fluctuations of the jet, called acoustic feedback. At the exit ($x = 0$), Eq. (2.5) assumes the followings to impose the boundary condition $\eta(0, t) = 0$:

- The feedback effects appear in η_{fluid} at the exit.
- The initial amplitude of η_{fluid} at the exit is the same with the amplitude of η_{aco}.
- The phase of η_{fluid} at the exit is opposite to that of η_{aco}.

However, the definition of the exit varies with studies; some studies define the exit as the starting position of a chamfer [34], while some define as the ending position of a chamfer [20]. The behaviors of the jet at the exit probably do not always be consistent with the assumptions in Eq. (2.5). Taking into account that there are some fluctuations of the jet at the geometrically defined exit ($\eta(0,t) \neq 0$), some formulas, like Eq. (2.6), have an initial amplitude at the exit.

2.2. Sound Source and Energy Loss

The jet interacts with the acoustic field around the edge to generate and maintain acoustic radiation. The sound source produced by the jet has been modeled: the jet-drive models for thin jets and the discrete vortex models for thick jets. The acoustic energy is dissipated by the flow separation and vortex shedding around the edge. These productions and dissipations have been studied theoretically.

2.2.1. Jet-Drive Model

The jet-drive models assume that the jet fluctuations around the edge drive the acoustic oscillations in the resonator [16, 18, 69, 70, 71, 72]. There are two theories for the driving mechanism: the volume-flow drive and the momentum (pressure) drive.

The volume-flow drive [70, 73] was first proposed by Helmholtz [70], assuming that the jet provides the acoustic field with the volume flow $q_{\mathrm{vd}}(t)$:

$$q_{\mathrm{vd}}(t) \approx -U_{\mathrm{e}} d\eta(l,t) = U_{\mathrm{e}} S_{\mathrm{j}}(t), \tag{2.7}$$

where U_{e} is the jet velocity at the edge, d is the spanwise width of the jet, l is the exit-edge distance, and S_{j} is the cross-sectional area of the jet entering the resonator ($S_{\mathrm{j}}(\mathrm{t}) = -d\eta(l,t)$). When the jet deflects inside the edge ($\eta < 0$), the volume flow is provided to the resonator ($q_{\mathrm{vd}}(t) > 0$).

The momentum drive assumes that the jet provides the acoustic field with the pressure

produced by the momentum exchange with air in the resonator:

$$p_{r,\mathrm{md}}(t) = \rho U_{\mathrm{e}}^2 \left(S_{\mathrm{j}}(t) \,/\, S_{\mathrm{r}} \right), \tag{2.8}$$

where ρ is the air density, and S_{r} is the cross-sectional area of the resonator [2, 72].

Elder [69] and Fletcher [71] have shown that both the two driving mechanisms contribute to the sound production. Combining the two contributions, the volume flow provided into the resonator was formulated by Elder [69] and simplified by Fletcher [2, 71]:

$$Q_{\mathrm{r}}(t) = \frac{p_{r,\mathrm{md}}(t)}{Z_{\mathrm{s}}} + \frac{Z_{\mathrm{m}} q_{\mathrm{vd}}(t)}{Z_{\mathrm{s}}} = \frac{(\rho U_{\mathrm{e}} + i\rho\omega\Delta L) U_{\mathrm{e}} S_{\mathrm{j}}(t)}{S_{\mathrm{r}} Z_{\mathrm{s}}}, \tag{2.9}$$

where Z_{s} is the impedance that connects the impedances of the resonator Z_{r} and the mouth $Z_{\mathrm{m}} = i\rho\omega\Delta L \,/\, S_{\mathrm{r}}$ in parallel ($Z_{\mathrm{s}} = Z_{\mathrm{r}} + Z_{\mathrm{m}}$), and ΔL is the end-correction length at the mouth. The first and the second term are the volume flow provided by the momentum and the volume-flow drive, respectively.

2.2.1.A. Phase Relation between Jet and Acoustic Field

The response of the acoustic field in the resonator to the jet has been studied from equivalent circuit models [69, 74]. In these models, the jet is assumed to be a generator. The admittance (or impedance) of the jet has been discussed by Cremer and Ising [73] and measured by Coltman [8, 50, 75, 76] and Thwaites *et al.* [74]. The following jet admittance is derived from the Fletcher *et al.* [9]'s formula for the jet displacement (Eq. (2.5)) based on the equivalent circuit model connecting the admittances of the jet (Y_{j}), the mouth (Y_{m}), and the resonator (Y_{r}) in parallel (See Fig. 2.3).

$$Y_{\mathrm{j}} \approx \frac{U_{\mathrm{e}} d}{\rho\omega^2 \Delta L} \left(\frac{S_{\mathrm{r}}}{S_{\mathrm{m}}} \right) \cosh(\alpha l) \exp\left[-i \left(\frac{\omega l}{U_{\mathrm{c}}} + \phi \right) \right], \phi = \tan^{-1}(U_{\mathrm{e}} \,/\, \omega\Delta L), \tag{2.10}$$

where S_{m} is the cross-sectional area of the mouth excluding S_{j}, the phase ϕ depends

on the ratio of the contributions of the two driving mechanisms to Q_r. Except for high blowing pressure conditions, the volume-flow drive is predominant to the momentum drive ($\omega\Delta L > U_e$); thus, the phase ϕ is small under practical conditions [2]. The jet admittance Y_j as a function of ω, l, and the jet velocity at the exit U_0 draws a spiral as shown in Fig. 2.4, where U_c is assumed to increase in proportion to U_0. This spiral-like behavior of Y_j has been also observed in the measurements [8, 50, 74, 75, 76].

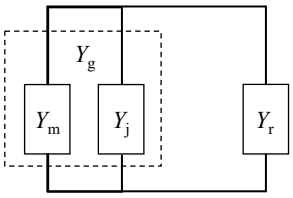

Figure 2.3 Equivalent circuit model connecting the admittances of the jet (Y_j), the mouth (Y_m), and the resonator (Y_r) in parallel, where the admittance of the generator (Y_g) consists of Y_j and Y_m [2, 74].

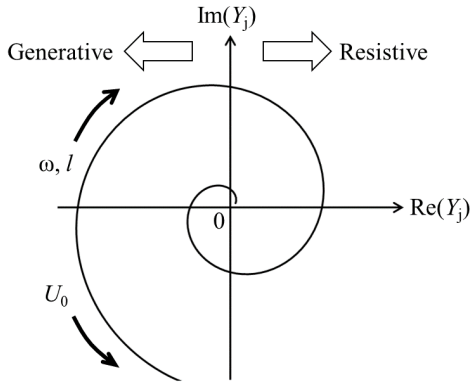

Figure 2.4 Qualitative behavior of jet admittance Y_j [51].

· **Optimum Condition**

There is a limit to the range of $\omega l / U_c$ that the jet generates acoustic power. When ignoring ϕ, the range for the acoustic power generation is $\pi / 2 < \omega l / U_c < 3\pi / 2$ [60], where Y_j has a negative real part. Under the condition that the exit-edge distance corresponds to almost the half wavelength ($\omega l / U_c = \pi$), the jet admittance Y_j is a

negative real quantity. This is the optimal condition for the acoustic power generation [2, 51].*

Figure 2.5 summarizes the phase relationship between the pressure in the resonator ($p_r(t)$), the acoustic particle velocity ($V_{ap}(t)$) and displacement ($\xi(t)$), the jet displacement at the exit ($\eta(0,t)$) and the edge ($\eta(l,t)$), the volume flow by the jet ($q_{vd}(t)$), and the force produced by the volume flow ($\mathcal{F}(t)$) in Sec. 2.2.1.B under the optimum condition of the jet and the pressure. At the optimum condition, $\eta(l,t)$ delays π from $p_r(t)$, where $\omega l / U_c$ is the phase delay of $\eta(l,t)$ from $p_r(t)$ (see Sec. 2.1.3). From Eq. (2.7), this anti-phase relationship corresponds to the in-phase relationship between $p_r(t)$ and $q_{vd}(t)$. Under the optimum condition, the jet deflects inside the edge when the pressure in the resonator becomes high, further promoting the compression of the air in the resonator (see Fig. 1.2). This anti-phase relationship between $\eta(l,t)$ and $p_r(t)$ has been also observed in the visualizations for the jet in a flute-like instrument model [77] and an organ pipe [11].

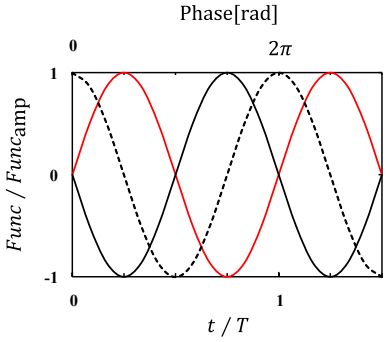

	Func				
	Pressure	Aco.particle	Jet	Vol. flow	Force
———	$p_r(t)$	$\xi(t)$	$\eta(0,t)$	$q_{vd}(t)$	
- - - -		$V_{ap}(t)$			$\mathcal{F}(t)$
———			$\eta(l,t)$		

Figure 2.5 Phase relationship between the pressure (p_r), the acoustic particle displacement (ξ) and velocity (V_{ap}), the jet displacement (η), the volume flow (q_{vd}), and the force produced by the volume flow ($\mathcal{F}$) under the optimum phase condition of jet and pressure.

* Describing by time, the range of the convection time, $t_c(= l / U_c)$ for the acoustic power generation is $0.25 < t_c / T < 0.75$, and the optimum condition is $t_c / T = 0.5$.

· **Effects on Resonance Frequency**

In the equivalent circuit model in Fig. 2.3, the stability condition for the acoustic resonance is $Y_{\mathrm{j}} + Y_{\mathrm{m}} + Y_{\mathrm{j}} = 0$. The imaginary parts of Y_{m} and Y_{r} are

$$\mathrm{Im}(Y_{\mathrm{m}}) = -\frac{S_{\mathrm{r}}}{\rho\omega\Delta L} < 0, \tag{2.11}$$

$$\mathrm{Im}(Y_{\mathrm{r}}) = -\frac{S_{\mathrm{r}}}{\rho L}\cot\,(kL), \tag{2.12}$$

where L is the resonator length. The change of $\mathrm{Im}(Y_{\mathrm{r}})$ with ω is shown in Fig. 2.6.

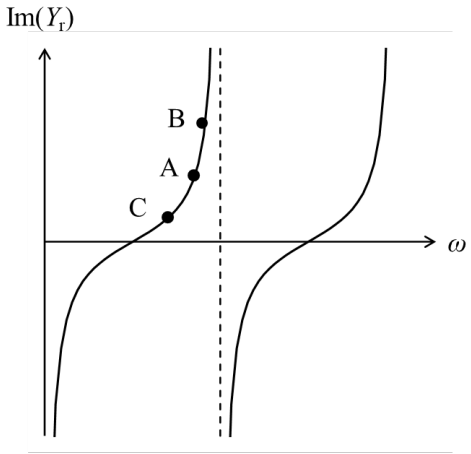

Figure 2.6 Qualitative behavior of imaginary part of resonator admittance Y_{r} [2].

At the optimal condition ($\mathrm{Im}(Y_{\mathrm{j}}) = 0$), $\mathrm{Im}(Y_{\mathrm{r}})$ is positive to hold the stability condition, as shown at point A in Fig. 2.6. When the jet velocity increases from the optimal condition, $\mathrm{Im}(Y_{\mathrm{j}})$ decreases, and $\mathrm{Im}(Y_{\mathrm{r}})$ for the stability condition increases (point B in Fig. 2.6); thus, the resonance frequency ($\omega = 2\pi f$) increases. When the jet velocity decreases from the optimal condition, the resonance frequency decreases (point C in Fig. 2.6). There is a limit to the resonance frequency that can be produced with a certain length of the resonator. When the jet velocity increases (decreases) beyond a threshold, the resonance frequency jumps to the next (former) acoustic mode [2].

2.2.1.B. Acoustic Power Generation

The jet-drive models take into account the two volume flow injections by the jet: $q_{\mathrm{vd}}(t)$ and $-q_{\mathrm{vd}}(t)$ on both sides of the edge (see Fig. 2.7).

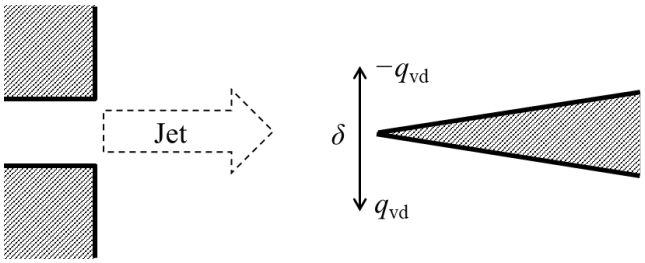

Figure 2.7 Volume flow injections in jet-drive model [16].

Alternate motions of the air mass between $q_{\mathrm{vd}}(t)$ and $-q_{\mathrm{vd}}(t)$ are assumed to act on the acoustic field. The force produced by these motions, $\mathscr{F}$, can be written in terms of a pressure difference acting across the mouth:

$$\frac{\mathscr{F}}{S_{\mathrm{mo}}} = \Delta p = -\frac{\rho}{S_{\mathrm{mo}}}\delta\frac{dq_{\mathrm{vd}}}{\mathrm{d}t}, \tag{2.13}$$

where δ is the effective distance between $q_{\mathrm{vd}}(t)$ and $-q_{\mathrm{vd}}(t)$, and S_{mo} is the cross-section of the mouth opening ($S_{\mathrm{mo}} = ld$).

The power generated by the jet drive is calculated by assuming that the volume flow is locally a two-dimensional incompressible flow and that Δp is in-phase with the acoustic volume flow of the acoustic particle on the mouth opening, $q_{\mathrm{ap}}(t) = V_{\mathrm{ap}}(t)S_{\mathrm{mo}}$, which corresponds to the optimum phase condition (see Fig. 2.5). The averaged acoustic power generated over an oscillation period T is

$$\overline{\mathscr{P}_{\mathrm{J}}} = \overline{\Delta p q_{\mathrm{ap}}} = \frac{2}{T}\int_0^{T/2}\Delta p q_{\mathrm{ap}}\mathrm{d}t, \tag{2.14}$$

where the jet is assumed to deflect inside the edge for half a period [16, 25, 77].

2.2.2. Discrete vortex model

As the jet becomes thick, the upside and the downside of shear layers of the jet behave independently; thus, the jet-drive model is not applicable. For thick jets, discrete vortex models have been applied [13, 77, 78, 79] - for instance, Holger *et al.* [78, 79] and Dequand *et al.* [77] respectively estimated the sound produced in edge tones and flutes based on discrete vortex models.

A discrete vortex model was proposed by Howe [80] based on a two-dimensional theory. In Meissner [81]'s description, the shear layers on the upper and the lower side of the jet are described as discrete vortices. The discrete vortices are generated from the flow separation point of the exit, where the vorticities are modulated, and assumed to drive the acoustic oscillations in the resonator. When discrete vortices are convected toward the edge, the following force vector is generated by the vorticity vector $\boldsymbol{\omega}$ of a discrete vortex and the velocity vector $\boldsymbol{V}$ of the local fluid:

$$\boldsymbol{\mathcal{F}} = -\rho(\boldsymbol{\omega} \times \boldsymbol{V}), \tag{2.15}$$

where $\boldsymbol{\mathcal{F}}$ is the force per unit volume, $\boldsymbol{V}$ consists of the mean velocity $\bar{\boldsymbol{V}}$ and the fluctuating component of the velocity $\boldsymbol{V}_{\mathrm{ap}}$: $\boldsymbol{V} = \bar{\boldsymbol{V}} + \boldsymbol{V}_{\mathrm{ap}}$. The acoustic power generated by the vortices is calculated by Howe's energy corollary [82]. The power density acting on the acoustic field is $\boldsymbol{\mathcal{F}} \bullet \boldsymbol{V}_{\mathrm{ap}}$. The averaged acoustic power generated over an oscillation period T is

$$\overline{\mathcal{P}_{\mathrm{D}}} = \frac{1}{T}\int_0^T \int_{V_{\mathrm{s}}} \boldsymbol{\mathcal{F}} \bullet \boldsymbol{V}_{\mathrm{ap}} \mathrm{d}V_{\mathrm{s}} \mathrm{d}t, \tag{2.16}$$

where the volume integration is taken over the source volume V_{s} that $\boldsymbol{\mathcal{F}} \bullet \boldsymbol{V}_{\mathrm{ap}}$ is not vanish [16, 68, 72, 77].

2.2.3. Criteria for model application

The criteria at which of the two models should be applied have been proposed based on aspect ratios of the jet. Dequand *et al.* [77] conducted pressure measurements and jet visualizations for flute-like instrument models and proposed the criterion based on the geometrical aspect ratio: $l / h > 2$ for a jet-drive model and $l / h < 2$ for a discrete vortex model. For recorders, the geometrical aspect ratio is generally around $l / h = 4$, where a jet-drive model is applicable. Auvray *et al.* [13] performed time-domain simulations and extended the criterion to the fluid dynamic aspect ratio of the jet $\lambda_{\mathrm{fluid}} / h$, where λ_{fluid} is the fluid dynamic wavelength of the jet.

For flute-like instruments, jet-drive models are generally applied. In fact, vertical jet fluctuations have been observed in flow visualizations for flute-like instruments [20, 23, 32, 33]. However, discrete vortex models seem to be useful to investigate the effects of edge shapes on the sound production [13, 16, 17]. The aspect ratios of the flute and the recorders investigated in this study are almost $l / h = 4$ to 6 and $\lambda_{\mathrm{fluid}} / h = 12$, where the jet-drive models are applicable [13].

2.2.4. Loss of Kinetic Energy of Jet

In addition to the linear behavior of the jet assumed in the jet-drive model, nonlinear behaviors should be taken into account to predict the oscillation amplitude in flute-like instruments. A nonlinear behavior is caused by vortex shedding at the edge. The interaction of the jet and the acoustic oscillation at the edge causes a flow separation, resulting in the formations of vortices. Verge *et al.* [83] and Fabre *et al.* [84] conducted flow visualizations and pressure measurements and respectively showed that the vortex shedding at the edge affects the attack transient and the generation of high harmonics. The pressure drop by the vortex shedding is formulated as

$$\Delta p = -\frac{1}{2}\rho\left(\frac{V_{\mathrm{ap}}}{\gamma}\right)^2 \mathrm{sgn}\left(V_{\mathrm{ap}}\right), \tag{2.17}$$

where γ is the vena-contracta factor of the jet ($\gamma = 0.6$ for a sharp edge). This pressure drop opposes V_{ap} and thus limits the oscillation amplitudes of the acoustic field. The vortex shedding dissipates the kinetic energy of the jet [16, 27, 85]. This effect of the vortex shedding has been taken into account in the prediction of the oscillation amplitude in an organ pipe by Fabre *et al.* [84, 86].

2.3. Harmonic Generation

The generation of harmonics by the jet-drive has been studied in terms of the temporal changes of the volume flow entering the resonator [2, 12, 87]. When the jet reaches the edge, the jet fluctuation center $(\overline{\eta})$ does not always hit the tip of the edge; there can be an offset between the jet fluctuation center and the edge. The calculations [12, 43, 87] and time-domain simulations [88] have been shown that this offset, jet offset (relative height of the jet fluctuation center from the edge), $y_{\mathrm{j,e}}$, affects the harmonic generation. Since the jet fluctuates temporally, the volume flow entering the resonator, $q_{\mathrm{vd}}(t)$, also changes temporally:

$$q_{\mathrm{vd}}(t) = \int_{-\infty}^{y_{\mathrm{j,e}}} dU_{\mathrm{e}}(y,t)\mathrm{d}y. \tag{2.18}$$

Harmonics in $q_{\mathrm{vd}}(t)$ is calculated by Fourier transform $q_{\mathrm{vd}}(t)$ [2, 12, 87]. Fletcher *et al.* [12] have calculated the internal source spectrum in an organ pipe, assuming that the velocity profile of the jet has the following bell-shaped profile [89]:

$$U_{\mathrm{e}}(y,t) = U_0 \,\mathrm{sech}^2[\{y - \eta(l,t)\} \,/\, h_{\mathrm{ref}}] \tag{2.19}$$

where h_{ref} is a reference jet thickness, and the jet is assumed to go straight toward the edge without bending.

Yoshikawa [87] has developed a filter function for the internal source spectrum to derive the radiated sound spectrum shown in Fig. 2.8. The SPLs of even number

harmonics are zero under the condition that the jet fluctuates symmetrically to the edge ($y_{j,e} = 0$) and increase as the jet fluctuates asymmetrical to the edge (as $|y_{j,e}|$ increases) almost within the range that the jet offset does not exceed the reference jet thickness ($\left|y_{j,e} / h_{ref}\right| \leq 1.0$). Conversely, the SPLs of odd number harmonics are maximum at $y_{j,e} = 0$ and decrease as $|y_{j,e}|$ increases almost within $\left|y_{j,e} / h_{ref}\right| \leq 1.0$.

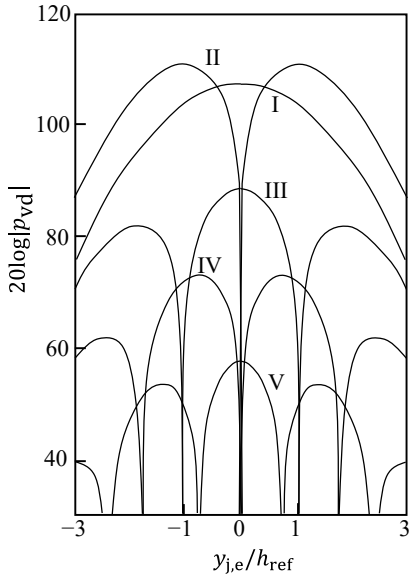

Figure 2.8 Sound pressure spectrum radiated from an organ pipe, where $p_{vd}(t)$ is the radiated sound pressure by the volume-flow drive. The value of dB is given by subtracting 26 from $20\log|p_{vd}|$. (Calculated by Yoshikawa [87])

This tendency, in which SPLs of odd and even number harmonics behave in almost opposite ways within a certain range of the jet offset, was also observed in the time-domain simulations for a flute by Coltman [88]; however, in the measurements for an organ pipe by Fletcher *et al.* [12], the SPLs of the even and odd harmonics were not completely zero for any of $y_{j,e}$ provably because of incomplete symmetry in actual jets and edge shapes. As mentioned in Sec. 2.1.4, the jet fluctuation center can be changed with distance [24, 25, 26, 68]; thus, the actual jet offset can be different from the jet offset

assuming a straight jet flow ($y_{j,e}$). These differences between the actual jet and the assumptions can cause inconsistencies between the measured SPLs and the calculations.

3. Analysis for Sound Change Mechanism: Formulation and Quantification of Jet Fluctuations by Direct Aeroacoustic Simulations

3.1. Introduction

To determine which of condition of blowing and shapes mainly contribute to a sound change, this chapter proposes an analytical method for quantifying jet fluctuation characteristics by representing predicted jet fluctuations from direct aeroacoustic simulations with a formula. This method is utilized to clarify the mechanisms by which two recorders have different acoustic mode predominancy in a certain velocity range.

3.2. Chapter Layout

In Sec. 3.3, the geometries and the radiated sounds of two subject recorders are presented. In Sec. 3.4, the methods for the computations. In Sec. 3.5, the formula proposed to represent the jet fluctuations is described along with its verification. In Sec. 3.6, the quantified jet fluctuation characteristics are compared between the two recorders to discuss the relevance of acoustic mode predominancy.

3.3. Flow Conditions

The flow and the acoustic fields around two different recorders that have different acoustic mode predominancy in a certain velocity range [33] were analyzed based on the results of direct aeroacoustic simulations. To reduce the computational cost, the recorders have only three opened tone holes, as shown in Fig. 3.1. Their resonator length from the mouth (window) opening to the resonator end is $L = 198$ mm. It is noted that these

configurations were the same as those in the experiments and computations in Ref. [33].

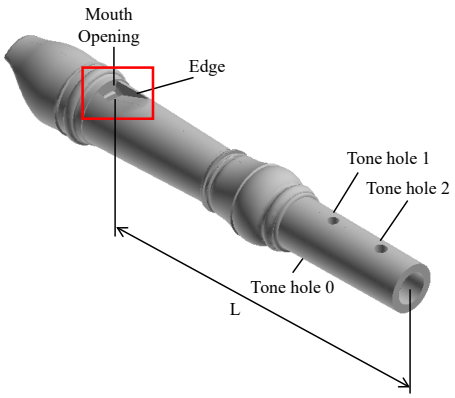

Figure 3.1 Short recorder with three tone holes.

The main difference between the two recorders are the geometries around the jet (channel or windway) exit and the edge. As shown in Fig. 3.2, the recorders have a straight- and an arch-shaped exit and edge, and are called the straight- and the arch-shaped recorder respectively. Table 3.1 shows the dimensions of the exit height, h, the mouth opening distance from the exit to the edge, l, and the vertical position of the edge, y_e, where h is nondimensionalized with the edge thickness, h_e. The origin of the coordinate system was located at the center of the exit, which is the starting point of the chamfering. The streamwise direction is the x-axis, its vertical direction is the y-axis, and the spanwise direction intersecting with those two axes is the z-axis.

(a) Straight-shaped recorder. (b) Arch-shaped recorder.

Figure 3.2 Close-up around the jet exit and the edge.

Table 3.1 Dimensions of recorders

Recorder	Jet exit height h / h_e	Exit-edge distance l / h	Edge position y_e / h
Straight	3.67	4.08	−0.269
Arch	3.04	4.59	−0.374

h_e: the edge thickness

Simulations were performed under the conditions of $10 \leq U_0 \leq 65$ m/s, where U_0 is the cross-sectional averaged streamwise velocity at the exit ($x = 0$). While the first mode was predominant in SPLs for the two recorders at 20 m/s, the first and the second mode were found to be predominant in the arch- and the straight-shaped recorder at 35 m/s respectively [33]. The results at $U_0 = 20$ and 35 m/s are mainly discussed in this paper. Reynolds number ($\mathrm{Re} \equiv U_0 h / \nu$) is shown in Table 3.2, where ν is kinematic viscosity.

Table 3.2 Reynolds number of recorders.

Recorder	Reynolds number $\mathrm{Re} \equiv U_0 h / \nu$		Maximum velocity at exit $U_{0,\max}$[m/s]	
	$U_0 = 20$ m/s	$U_0 = 35$ m/s	$U_0 = 20$ m/s	$U_0 = 35$ m/s
Straight	1699	2974	26.2	45.8
Arch	1407	2463	28.1	47.8

3.4. Computational Methodologies and Results

3.4.1. Governing Equations and Finite-Difference Formulation

The governing equations for the simulations of the interactions between the flow and the acoustic field are based on the continuity equation, the three-dimensional compressible Navier-Stokes equations, and the energy conservation equation. A volume-

penalization (VP) method [90, 91], which is a kind of immersed-boundary methods [92], was used to reproduce the complex shapes of the recorder on a rectangular grid. The governing equations are expressed as follows:

$$\boldsymbol{Q}_t + (\boldsymbol{H}_x - \boldsymbol{G}_x)_x + \left(\boldsymbol{H}_y - \boldsymbol{G}_y\right)_y + (\boldsymbol{H}_z - \boldsymbol{G}_z)_z = \boldsymbol{F}, \tag{3.1}$$

where $\boldsymbol{Q}$ is the vector of the conservative variables, $\boldsymbol{H}$ is the inviscid flux vectors, $\boldsymbol{G}$ is the viscous flux vectors, $\boldsymbol{F}$ is the penalization term:

$$\boldsymbol{Q} = \begin{pmatrix} \rho \\ \rho u \\ \rho v \\ \rho w \\ \rho E \end{pmatrix}, \ \boldsymbol{H}_x = \begin{pmatrix} \rho u \\ \rho uu + p \\ \rho vu \\ \rho wu \\ (\rho E + p)u \end{pmatrix}, \ \boldsymbol{H}_y = \begin{pmatrix} \rho v \\ \rho uv \\ \rho vv + p \\ \rho wv \\ (\rho E + p)v \end{pmatrix}, \ \boldsymbol{H}_z = \begin{pmatrix} \rho w \\ \rho uw \\ \rho vw \\ \rho ww + p \\ (\rho E + p)w \end{pmatrix},$$

$$\boldsymbol{G}_x = \begin{pmatrix} 0 \\ \tau_{xx} \\ \tau_{yx} \\ \tau_{zx} \\ G_{x5} \end{pmatrix}, \ \boldsymbol{G}_y = \begin{pmatrix} 0 \\ \tau_{xy} \\ \tau_{yy} \\ \tau_{zy} \\ G_{y5} \end{pmatrix}, \ \boldsymbol{G}_z = \begin{pmatrix} 0 \\ \tau_{xz} \\ \tau_{yz} \\ \tau_{zz} \\ G_{z5} \end{pmatrix}, \ G_{i5} = u_j \tau_{ij} - q_i, \tag{3.2}$$

$$\boldsymbol{F} = -\left(\frac{1}{\Omega} - 1\right)\chi \begin{pmatrix} \partial \rho u_{\mathrm{i}} / \partial x_{\mathrm{i}} \\ 0 \\ 0 \\ 0 \\ 0 \end{pmatrix}, \ \Omega = 0.25,$$

where u, v and w are the velocities in the x, y, and z direction in the computational space, E is the total energy, τ_{ij} is the viscous stress tensor, q_i is the heat flux. The indexes i, j follow the Einstein summation convention. The parameter Ω was adjusted to 0.25 for the approximately perfect reflection of the sound wave on the objects without the computational unsteadiness. The mask function χ is

$$\chi = \begin{cases} 1(\text{inside object}) \\ 0(\text{outside object}) \end{cases}. \tag{3.3}$$

Spatial derivatives were evaluated by the sixth-order compact finite-difference scheme (fourth-order accuracy at boundaries) [93]. Time integration was performed by the third-order Runge-Kutta method [94].

To reduce computational instability [95], the following 10th-order spatial filter was used:

$$\alpha'_{\mathrm{f}}\hat{\zeta}_{i-1} + \hat{\zeta}_i + \alpha'_{\mathrm{f}}\hat{\zeta}_{i+1} = \sum_{n=0}^{5} \frac{\beta'_n}{2}(\zeta_{i+n} + \zeta_{i-n}) \tag{3.4}$$

where ζ and $\hat{\zeta}$ are a conservative and a filtered quantity respectively. Coefficient β'_n has the same value as that used by Gaitonde and Visbal [96], and the value of α'_{f} is 0.45.

3.4.2. Computational Grid

The computational domain, shown in Fig. 3.3, was divided into three regions: a vortex region, a sound region, and a buffer region. The shape of the computational grid is rectangular. The grid spacing varied between the regions and was smoothly stretched from the vortex region to the buffer region.

In the vortex region, the minimum grid spacings were $\Delta x = \Delta y = 0.05$ mm, $\Delta z = 0.15$ mm around the exit and the edge, as in Refs. [32, 33], where these spacings have been confirmed to be sufficiently fine to capture the jet fluctuations and vortices around the edge [32]. In the sound region, more than 10 grid points were used per fundamental wavelength to capture the propagation of acoustic waves. In the buffer region, the grid was stretched to attenuate acoustic waves to prevent intense reflections of the acoustic waves on the boundaries [97]. The total number of grid points was approximately 7.7×10^7.

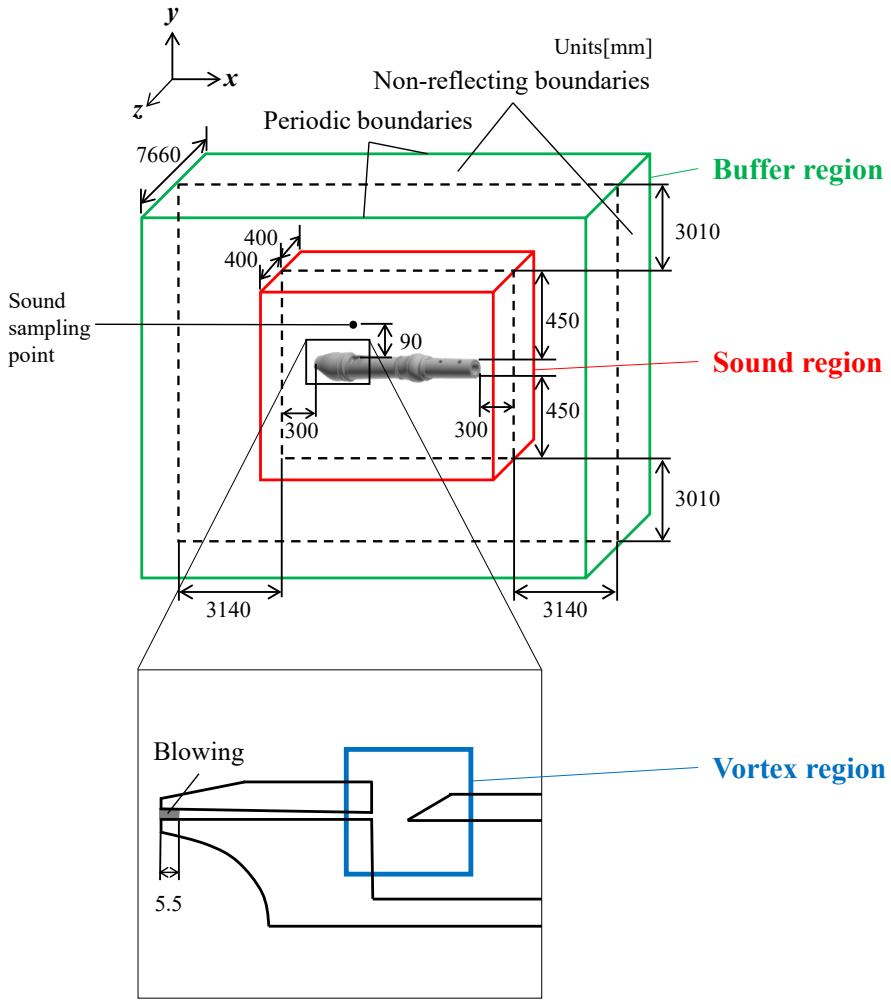

Figure 3.3 Computational domain and boundary conditions.

3.4.3. Boundary and Initial Conditions

The boundary conditions of the computation are shown in Fig. 3.3. Non-reflecting boundaries [98, 99, 100] were used at the boundaries of the x- and y- directions, and periodic boundary conditions were adopted in the z-direction. To reproduce the jet from the windway, the blowing velocity was imposed in the inlet region of the windway, as shown in gray color in Fig. 3.3.

3.4.4. Validation of Computational Methods

The above-mentioned computational methods have been validated in Ref. [33] by comparing the predicted jet fluctuations with those measured by particle image velocimetry along with the comparison of predicted and measured sound spectra.

Figure 3.4 shows the variation of the fundamental frequency (frequency with the largest SPL), f_{pr}, with the jet velocity (U_0), predicted and measured for the two recorders. The predicted fundamental frequencies approximately agreed with the measured values. The measured fundamental frequency shifts from the first to the second mode around $U_0 = 30, 50$ m/s in the straight- and the arch-shaped recorder, respectively. The present simulations correctly predict the feature that the shift of the fundamental mode occurs at a higher jet velocity in the arch-shaped recorder than in the straight-shaped recorder.

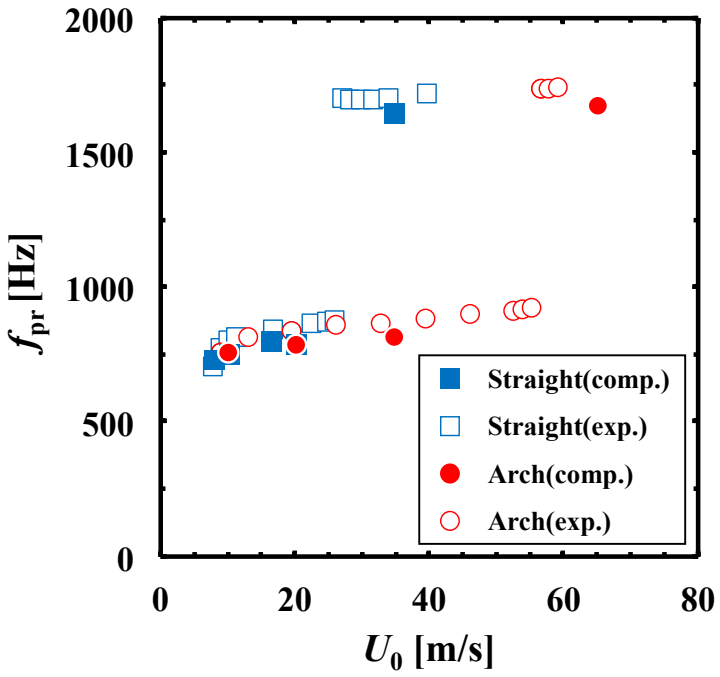

Figure 3.4 Predicted and measured variation of the fundamental frequency (frequency with the largest SPL) f_{pr} with the jet velocity U_0 [33].

3.4.5. Results

3.4.5.A. Radiated Sound

The radiated sound pressure spectra were measured at a distance of 90 mm from the exit ($x = 0$ mm, $y = 90$ mm, $z = 0$ mm) (see Fig. 3.3). The predicted sound pressure spectra by the direct aeroacoustic simulations at $U_0 = 20$ and 35 m/s are shown in Fig. 3.5. The frequency resolution was 78 Hz. At both the velocities, the frequencies of the first modes of the two recorders are around 800 Hz, and the SPLs of the first modes are almost the same. The frequencies of the second modes of the two recorders are around 1600 Hz, and the SPLs of the second modes are more intense in the straight-shaped recorder than that in the arch-shaped recorder. In the straight-shaped recorder, the SPL of the second acoustic mode is more intense than of the first mode at $U_0 = 35$ m/s, where the radiation for the second acoustic mode is predominant.

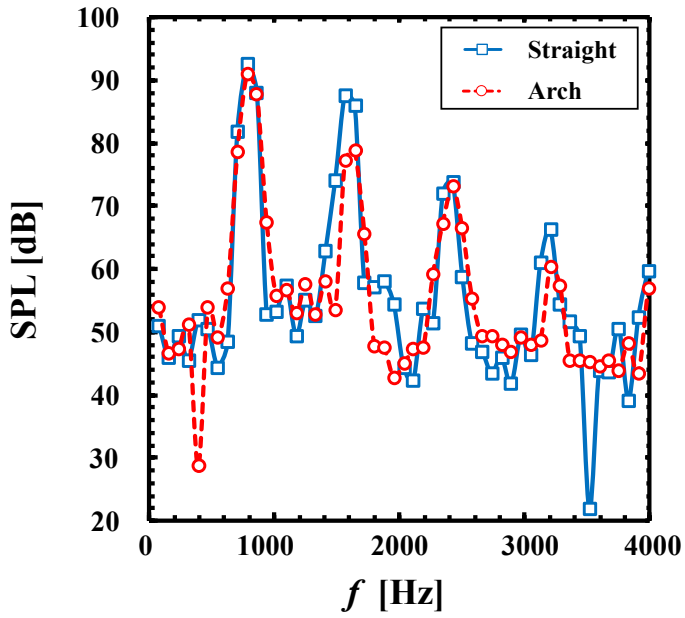

(a) $U_0 = 20$ m/s

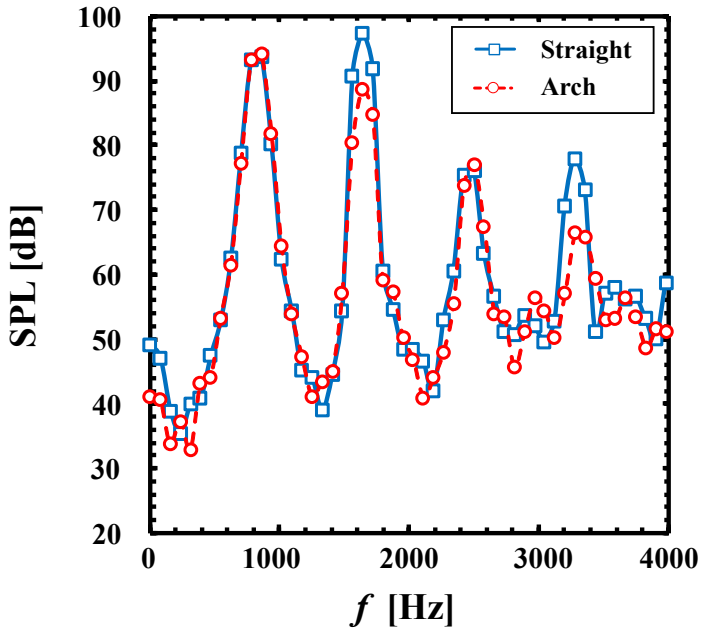

(b) $U_0 = 35$ m/s

Figure 3.5 Sound pressure spectra ($x = 0$ mm, $y = 90$ mm, $z = 0$ mm).

3.4.5.B. Pressure Amplitude in Resonator

This study evaluates the standing waves by the pressure fluctuations along the line connecting the center lines of the resonator and the mouth opening shown in Fig. 3.6, where the x_s-axis is the direction from the mouth to the resonator end along this line and the origin is the intersection of the center lines. Figure 3.7 shows the nondimensional amplitudes of the first mode (half-wavelength acoustic mode) and the second mode (one-wavelength acoustic mode) of the pressure fluctuations (p') along the path of standing waves, $p'_{amp} / p'_{amp,1,max}$, where values are nondimensionalized with the maximum amplitude of the first mode. At both the velocities, the nondimensional pressure amplitude of the second mode is larger in the straight-shaped recorder than in the arch-shaped recorder. With increasing the jet velocity from $U_0 = 20$ and 35 m/s, the relative pressure amplitude of the second to the first mode is more increased in the straight-shaped recorder than in the arch-shaped recorder. Inside the resonator (between the mouth opening and the tone hole 0), the pressure amplitude of the first mode is predominant in both the recorders under $U_0 = 20$ and 35 m/s. Outside the resonator, the pressure amplitude of the second mode is larger than of the first mode in the straight-shaped recorder at $U_0 = 35$ m/s; therefore, the radiation for the second acoustic mode is predominant, as shown in Fig. 3.5(b).

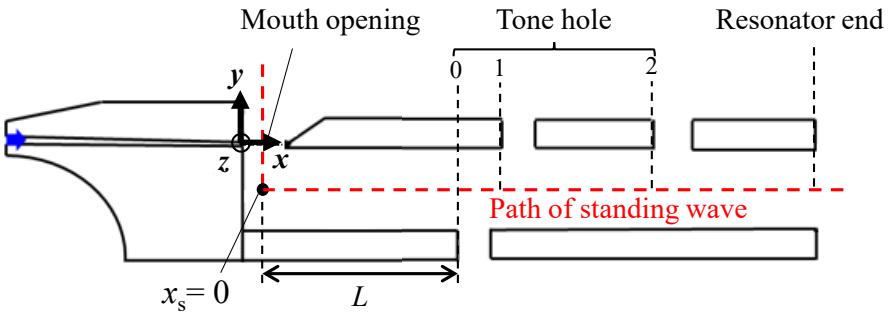

Figure 3.6 Definition of the path of standing wave, where the x_s-axis is the direction from the mouth to the resonator end along the path and the origin is the intersection of the center lines of the resonator and the mouth opening.

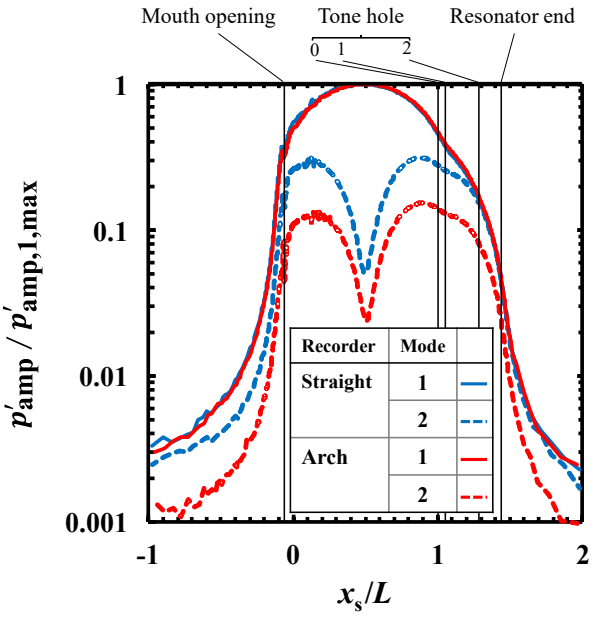

(a) $U_0 = 20$ m/s

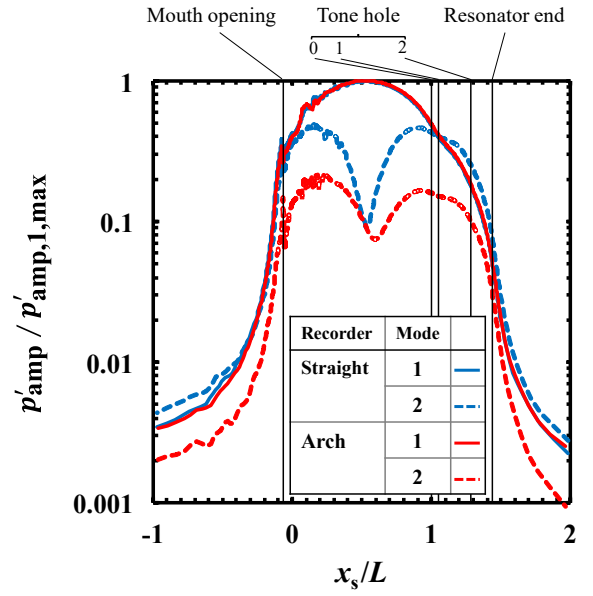

(b) $U_0 = 35$ m/s

Figure 3.7 Nondimensional amplitude of the first and the second mode of pressure fluctuations along the path of standing waves, where values are nondimensionalized with the maximum amplitude of the first mode of pressure fluctuations. Black lines show tone hole positions.

3.4.5.C. Velocity Profile of Jet

Figure 3.8 shows the profiles of the time-averaged streamwise velocity $\bar{U}$ at the spanwise center of the exit ($x = 0,\ z = 0$), where the values are nondimensionalized with the maximum velocity at the spanwise center of the exit, $U_{0,\max}$. The velocity profiles of the two recorders are similar.

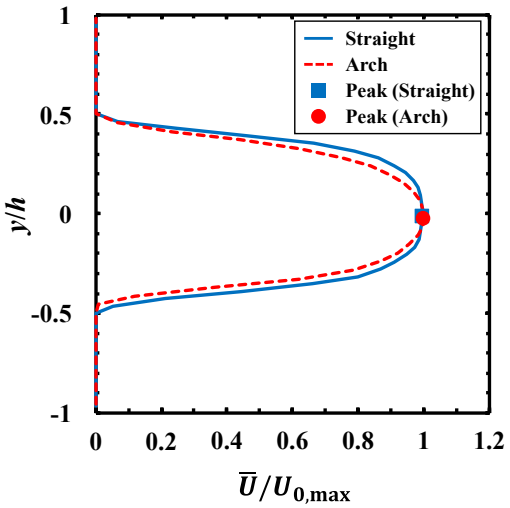

(a) $U_0 = 20$ m/s

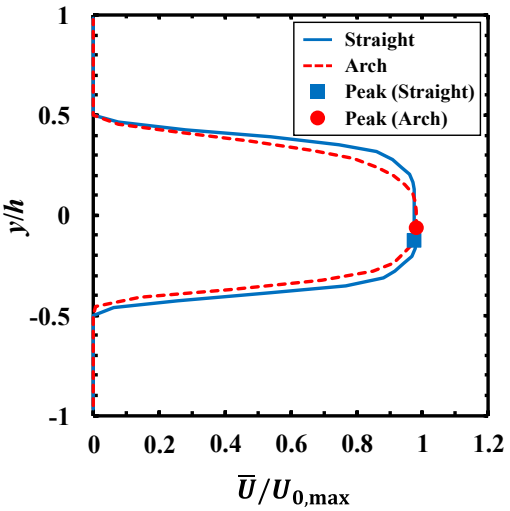

(b) $U_0 = 35$ m/s

Figure 3.8 Profiles of the time-averaged streamwise velocity at the spanwise center of exit ($x = 0,\ z = 0$).

3.5. Formulation of Jet Oscillations

3.5.1.A. Formulation of Jet Displacement

As described in Sec. 2.1.3, Fletcher's formula [9] for the fluctuations of jet displacement (Eq. (2.5)) consists of the two components: the fluid dynamic and the acoustic jet displacement. This decomposition of jet displacement can allow the quantifications of the spatial and the temporal relationship between the fluid dynamic oscillations of the jet and the acoustic oscillations in the resonator, e.g., the acoustic feedback effects on jet, the phase relation between the jet and the acoustic oscillations. Also, Eq. (2.5) has been confirmed to be in agreement with the experimental results [9]. Modifying this formula, this study proposes a formula that fits jet fluctuations predicted by the computations.

The computational results are shown in Figs. 3.9 and 3.10. Figure 3.9 shows the temporal variation of the profile of predicted streamwise velocity at the spanwise center of the exit ($x = 0, z = 0$), where T_1 is the period of the first acoustic mode and $t = 0$ is the instant of expansion in the resonator evaluated at the antinode on the standing wave path in Fig. 3.6. The peak of each velocity profile was obtained by a polynomial approximation to determine the peak from the outline of the profile, not from the unevenness of the local flow velocity. The instantaneous peak position changes with time. This indicates that the amplitude of jet fluctuations at the exit is not zero, whereas the initial jet amplitude at the exit ($x = 0$) is assumed to be zero in Eq. (2.5). Figure 3.10 shows the contours of the time-averaged streamwise velocity at the spanwise center ($z = 0$). The distributions of velocity inclines inside the resonator. This indicates that the time-averaged position of jet inclines as it approaches the edge, while Eq. (2.5) assumes a symmetrical oscillation of the jet with respect to the center height of the exit ($y = 0$). These behaviors of jet, the initial jet amplitude and the inclination of time-averaged position of jet, were observed in both the recorders under the conditions of $U_0 = 20$ and 35 m/s.

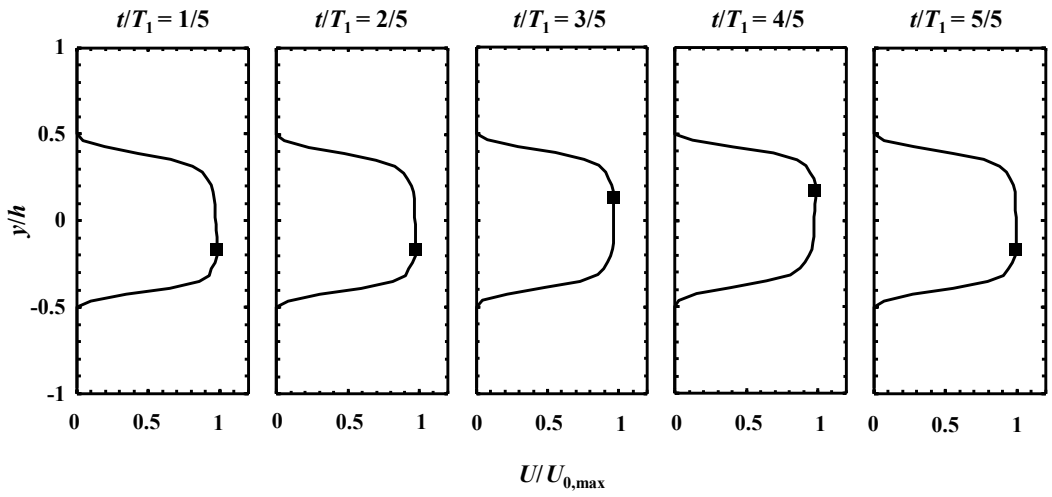

Figure 3.9 Predicted temporal variations of streamwise velocity profile at spanwise center of the exit ($x = 0$, $z = 0$) in the straight-shaped recorder under condition of $U_0 =$ 35 m/s, where T_1 is the period of the first acoustic mode and $t = 0$ is the instant of expansion in the resonator evaluated at the antinode on the standing wave path in Fig. 3.6.

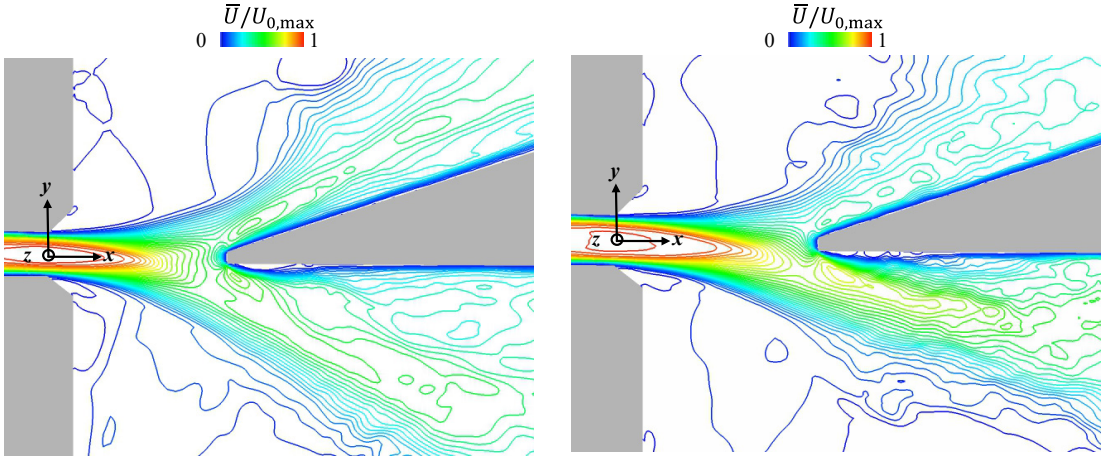

(a) $U_0 = 20$ m/s (b) $U_0 = 35$ m/s

Figure 3.10 Predicted time-averaged streamwise velocity at the spanwise center ($z =$ 0) in the straight-shaped recorder.

Taking into these characteristics, this study proposes a formula taking into account that the time-averaged value of the jet displacement (jet fluctuation center, $\bar{\eta}(x)$) varies in the x-direction and that the jet amplitude at the exit ($x = 0$) is not zero. The formulation of the proposed formula is as follows:

$$\eta(x,t) = \sum_n \eta_n(x,t) + \bar{\eta}(x) = \sum_n \left\{ \eta_{\mathrm{fluid},n}(x,t) + \eta_{\mathrm{aco},n}(t) \right\} + \bar{\eta}(x), \quad (3.5)$$

The definitions of parameters in Eqs. (3.5)-(3.7) are shown in Table 3.3. The jet fluctuations with multiple modes are expressed as the superposition of the oscillation at each mode. The jet oscillation at the nth mode consists of the fluid dynamic jet displacement, $\eta_{\mathrm{fluid},n}$, and the acoustic jet displacement, $\eta_{\mathrm{aco},n}$, with $\bar{\eta}(x)$ as the jet fluctuation center. The formulations of $\eta_{\mathrm{fluid},n}$ and $\eta_{\mathrm{aco},n}$ are

$$\eta_{\mathrm{fluid},n}(x,t) = e^{\alpha_n x} A_{\mathrm{fluid},n} \sin\left[\frac{2\pi}{T_n} \left\{ t - \left(t_{\mathrm{c},n}(x) + t_{0,n} + t_{\mathrm{aco},n} + t_{\mathrm{p},n} \right) \right\} - \frac{\pi}{2} \right], \quad (3.6)$$

$$\eta_{\mathrm{aco},n}(t) = A_{\mathrm{aco},n} \sin\left[\frac{2\pi}{T_n} \left\{ t - \left(t_{\mathrm{aco},n} + t_{\mathrm{p},n} \right) \right\} - \frac{\pi}{2} \right]. \quad (3.7)$$

The spatial behaviors of these displacements are as follows. These two displacements have amplitudes at the exit: $A_{\mathrm{fluid},n}$ for the fluid dynamic displacement, $A_{\mathrm{aco},n}$ for the acoustic jet displacement. As the jet travels downstream, the amplitude of the fluid dynamic jet displacement amplifies at the amplification rate α_n, while the amplitude of the acoustic jet displacement is constant. The temporal behaviors are as follows. The acoustic jet displacement ($\eta_{\mathrm{aco},n}$) is in-phase with the acoustic particle displacement ($\xi_n(t) = \left(V_{\mathrm{ap},n,\mathrm{amp}} / \omega_n \right) \sin\left[2\pi / T_n \left\{ t - \left(t_{\mathrm{aco},n} + t_{\mathrm{p},n} \right) \right\} - \pi / 2 \right]$). Here, ξ_n delays from the nth mode of pressure oscillation by $t_{\mathrm{aco},n}$, where the nth mode of pressure oscillation is assumed to delay by $t_{\mathrm{p},n}$ from its first mode. The fluid dynamic jet displacement ($\eta_{\mathrm{fluid},n}$) delays from the acoustic jet displacement by $t_{0,n}$ at the exit. As this oscillation is convected, the oscillation delays by $t_{\mathrm{c},n}(x)$.

Table 3.3 Definitions of parameters in Eqs. (3.5)-(3.7).

Parameter	Definition
n	Mode of jet fluctuation
α_n	Streamwise amplification rate of the fluid dynamic jet displacement
$A_{\mathrm{fluid},n}$	Initial amplitude of the fluid dynamic jet displacement
$A_{\mathrm{aco},n}$	Amplitude of the acoustic jet displacement
T_n	Time period of nth acoustic mode
$t_{\mathrm{p},n}$	Time delay of nth mode of the pressure fluctuations in the resonator ($p'_{\mathrm{r},n}$) from its first mode ($p'_{\mathrm{r},1}$)
$t_{\mathrm{aco},n}$	Time delay of acoustic jet displacement ($\eta_{\mathrm{aco},n}$) from $p'_{\mathrm{r},n}$
$t_{0,n}$	Time delay of fluid dynamic jet displacement at the exit ($\eta_{\mathrm{fluid},n}(0,t)$) from $\eta_{\mathrm{aco},n}$
$t_{\mathrm{c},n}(x)$	Time delay of fluid dynamic jet displacement at each streamwise position ($\eta_{\mathrm{fluid},n}(x,t)$) from that at the exit ($\eta_{\mathrm{fluid},n}(0,t)$)

From these definitions, the values for $t_{\mathrm{p},1}$ and $t_{\mathrm{c},n}(0)$ are zero. The reference time ($t = 0$) is the instant when $p'_{\mathrm{r},1}$ exhibits its minimum. The acoustic jet displacement ($\eta_{\mathrm{aco},n}$) is assumed to be in-phase relation with the fluctuations of the acoustic particle displacement around the mouth (ξ_n), referring to Eq. (2.5).

The relation between $t_{\mathrm{c},n}(x)$ and the convection velocity is:

$$t_{\mathrm{c},n}(x) = \int_0^x 1 / U_{\mathrm{c},n}(s)\mathrm{d}s, \tag{3.8}$$

where s is a distance in the x-direction. In Eq. (3.6), the convection velocity of the fluid dynamic jet displacements ($U_{\mathrm{c},n}$) is the function of x, while $U_{\mathrm{c},n}$ is constant in Fletcher's formula [9]. This modification takes into account that the convection velocity may decrease with x, as observed in the jet visualization for organ pipes by Yoshikawa [23].

3.5.1.B. Estimation of Blowing Parameters

The parameters in Eqs. (3.5)-(3.7) were estimated by fitting the computational results to the formula. In preliminary operations, the fluctuations of the jet displacement ($\eta(x,t)$), the pressure ($p'_{\mathrm{r},n}$), and the acoustic particle velocity ($V_{\mathrm{ap},n}$) were evaluated from the computational results in the following manner:

- The jet displacement was evaluated from the velocity distributions on the cross section of the spanwise center ($z = 0$) because the jet behaviors are almost two-dimensional along the spanwise extent of the exit. This study defines the jet displacement ($\eta(x,t)$) as the y-coordinate value of the instantaneous peak position of a velocity profile.
- The specific mode of fluctuations was extracted by performing Fourier transformation of the fluctuation, imposing zero on the amplitudes of the other modes, and performing an inverse Fourier transformation.
- The nth mode of the pressure fluctuations ($p'_{\mathrm{r},n}$) was evaluated at its antinode on the standing wave path in Fig. 3.6.
- The acoustic particle velocity around the mouth ($V_{\mathrm{ap},n}$) was evaluated by averaging the vertical velocity (V) in the mouth field close to the exit ($x/h \approx 1, -7 < y/h < -2$), where the effects of the jet fluctuations are negligible. The amplitude of $V_{\mathrm{ap},n}$ was evaluated from $\sqrt{2}$ of the rms value of $V_{\mathrm{ap},n}$: $V_{\mathrm{ap},n,\mathrm{amp}} = \sqrt{2}V_{\mathrm{ap},n,\mathrm{RMS}}$. The acoustic particle displacement ($\xi_n(t) = \left(V_{\mathrm{ap},n,\mathrm{amp}} / \omega_n\right)\sin\left[(2\pi / T_n)\left\{t - \left(t_{\mathrm{aco},n} + t_{\mathrm{p},n}\right)\right\} - \pi/2\right]$) was calculated from $V_{\mathrm{ap}}(t) = V_{\mathrm{ap},n,\mathrm{amp}}\sin\left[(2\pi / T_n)\left\{t - \left(t_{\mathrm{aco},n} + t_{\mathrm{p},n}\right)\right\}\right]$.

The time delay of $\eta_{\mathrm{aco},n}$ from $p'_{\mathrm{r},n}$ ($t_{\mathrm{aco},n}$) was estimated from ξ_n and $p'_{\mathrm{r},n}$, where $\eta_{\mathrm{aco},n}$ and ξ_n are assumed to be in-phase. The jet fluctuation center ($\bar{\eta}(x)$) was calculated by time averaging η over one fundamental period. The other parameters, α_n, $A_{\mathrm{fluid},n}$, $A_{\mathrm{aco},n}$, $t_{0,n}$, and $t_{\mathrm{c},n}(x)$, were obtained by the following fitting procedure:

1. To reduce the number of parameters, the differential jet displacement from the exit, which cancels out the acoustic jet displacement, was derived from Eq. (3.6):

$$\eta_{\mathrm{diff},n}(x,t) = \eta_n(x,t) - \eta_n(0,t) = \eta_{\mathrm{fluid},n}(x,t) - \eta_{\mathrm{fluid},n}(0,t). \tag{3.9}$$

The amplitude of $\eta_{\mathrm{diff},n}$ is written as

$$\eta_{\mathrm{diff},n,\mathrm{amp}}(x,t) = \left[e^{2\alpha_n x} A_{\mathrm{fluid},n}^2 - 2e^{\alpha_n x} A_{\mathrm{fluid},n}^2 \cos\left\{ 2\pi t_{\mathrm{c},n}(x) \,/\, T_n \right\} + A_{\mathrm{fluid},n}^2 \right]^{1/2}. \tag{3.10}$$

The computational results of $\eta_{\mathrm{diff},n,\mathrm{amp}}(x,t)$ were fitted to Eq. (3.10) to obtain $A_{\mathrm{fluid},n}$ and α_n. Here, the initial value for $t_{\mathrm{c},n}(x)$ was determined from Eq. (3.8), assuming $U_{\mathrm{c},n} = 0.4U_{0,\max}$ [23]. In the second and the subsequent iterations of the procedure, the obtained value of $t_{\mathrm{c},n}(x)$ in the previous step was given.

2. The parameters $t_{0,n}$ and $A_{\mathrm{aco},n}$ were obtained by fitting the jet displacements of the computational results at the exit to $\eta_n(0,t)$.
3. The time delay $t_{\mathrm{c},n}(x)$ was obtained by fitting the jet displacements at each streamwise position to $\eta_n(x,t)$.
4. The amplification rate α_n was corrected by fitting the jet amplitudes of the computational results to the numerical expression for the jet amplitude:

$$\eta_{n,\mathrm{amp}}(x,t) = \left[e^{2\alpha_n x} A_{\mathrm{fluid},n}^2 - 2e^{\alpha_n x} A_{\mathrm{fluid},n} A_{\mathrm{aco},n} \cos\left\{ 2\pi \left(t_{\mathrm{c},n}(x) + t_{0,n} \right) \,/\, T_n \right\} + A_{\mathrm{aco},n}^2 \right]^{1/2}. \tag{3.11}$$

The parameters (α_n, $A_{\mathrm{fluid},n}$, $A_{\mathrm{aco},n}$, $t_{0,n}$, and $t_{\mathrm{c},n}(x)$) were solved by an iteration method. This procedure was repeated until the change rate of each parameter, a, at nth fitting, $|(a^n - a^{n-1}) \,/\, a^n|$, was reduced to about 2%.

3.5.1.C. Validation for Proposed Formula

Figures 3.11 and 3.12 show the spatial and the temporal variations of the first and the second mode of the jet displacement in the straight-shaped recorder at $U_0 = 35$ m/s. The square symbols show the jet displacement predicted by the direct aeroacoustic simulations. The curves show the jet displacement by the formula. The cross symbols show the jet fluctuation centers. The spatial and the temporal variations of the jet displacement predicted by the direct aeroacoustic simulations fitted well with the formula.

Figure 3.13 shows the jet amplitudes of the first and the second mode and the error rate of the formula to the computational results. The averaged error rate was almost within 10%. The error rate in the second mode is higher than in the first mode. The error rate seems to increase as the jet amplitude becomes small. The jet amplitude of the second mode in the arch-shaped recorder at $U_0 = 20$ m/s was too small to give accurate fitting results; therefore, the jet fluctuations are compared between the two recorders in terms of the first mode at $U_0 = 20$ m/s and the first and second mode at $U_0 = 35$ m/s.

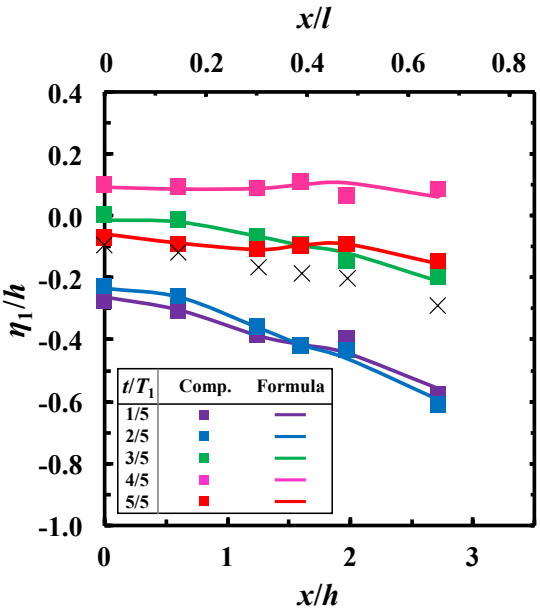

(a) First mode

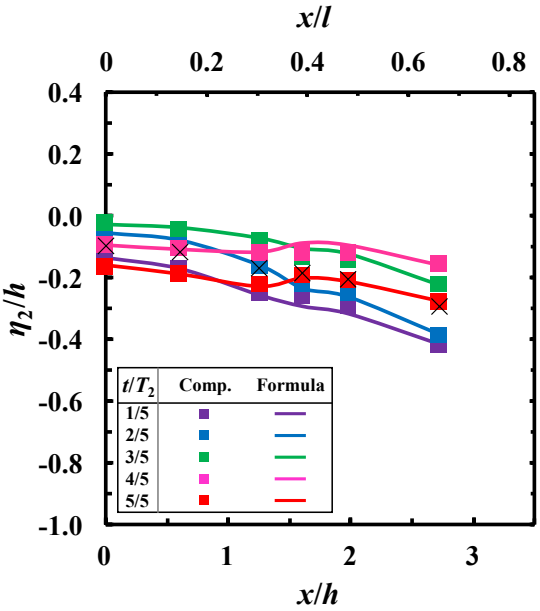

(b) Second mode

Figure 3.11 Spatial variations of the jet displacement for the straight-shaped recorder at $U_0 = 35$ m/s, where cross symbols indicate positions of the jet fluctuation center, and T_1 and T_2 represent the time periods of the first and second modes.

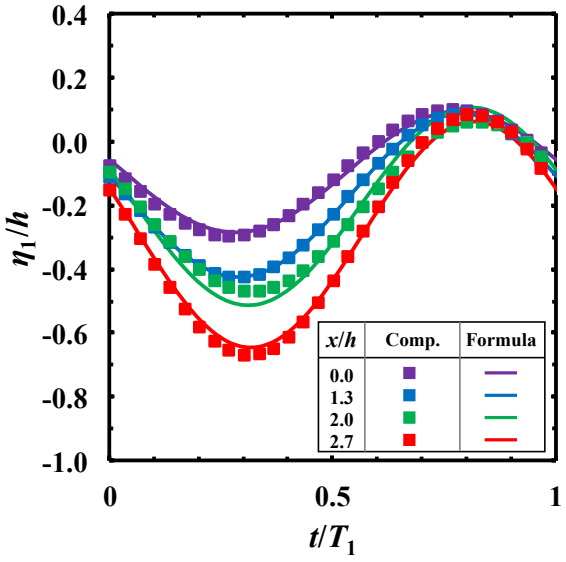

(a) First mode

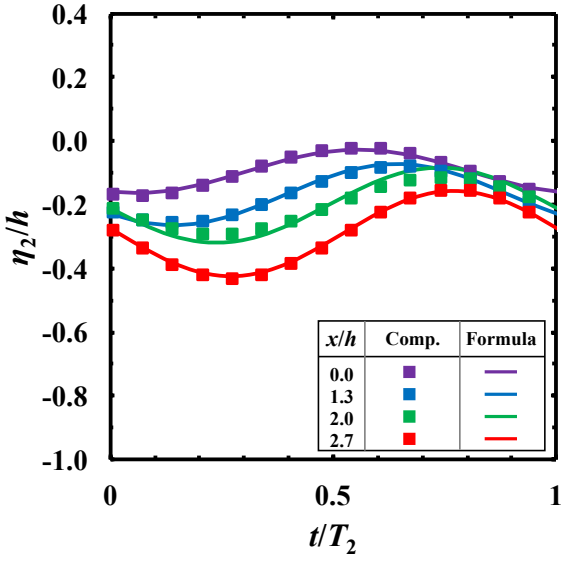

(b) Second mode

Figure 3.12 Temporal variations of the jet displacement for the straight-shaped recorder at $U_0 = 35$ m/s, where T_1 and T_2 represent the time periods of the first and second modes.

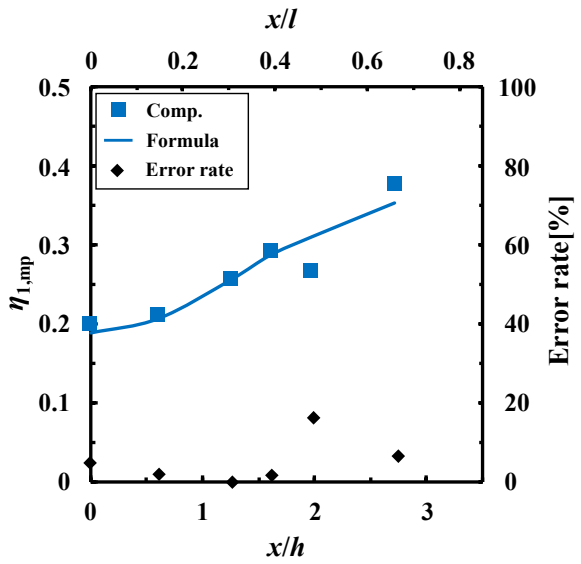

(a) First mode

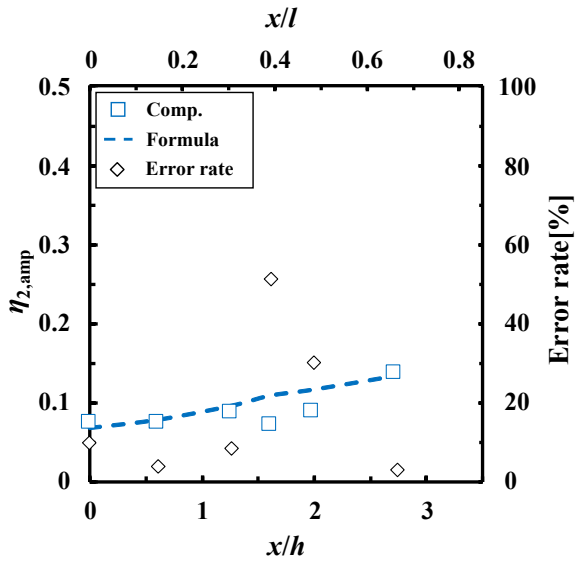

(b) Second mode

Figure 3.13 Jet amplitude and error rate in the straight-shaped recorder at $U_0 = 35$ m/s.

3.6. Analysis of Jet Fluctuations

The jet fluctuation characteristics are quantified based on the obtained values of the parameters to discuss the difference in the acoustic mode predominancy of the two recorders.

3.6.1.A. Jet Offset

Figure 3.14 shows the spatial distributions of the jet fluctuation centers ($\overline{\eta}$). In all cases, the jet fluctuation center inclines to the inside the resonator as the jet approaches the edge.

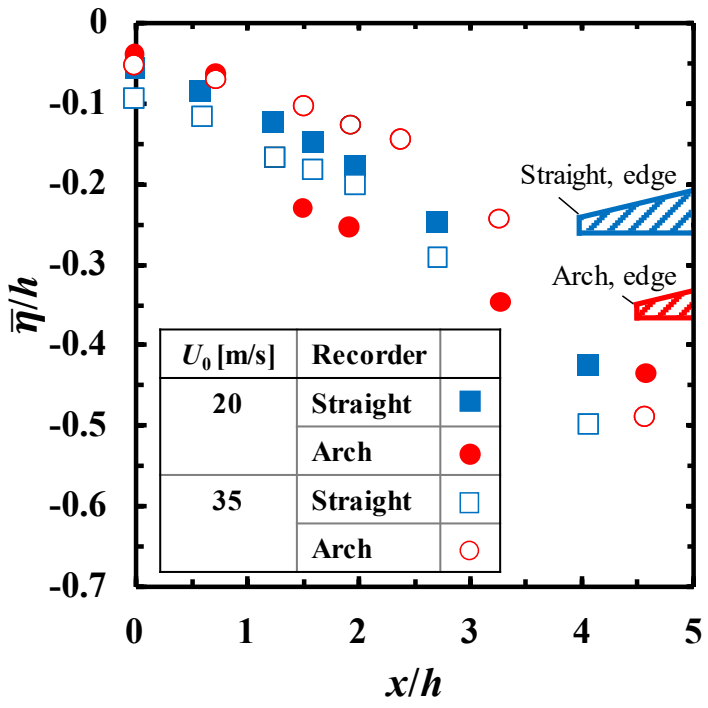

Figure 3.14 Spatial distributions of jet oscillation centers, where the edge positions are the positions in Table 3.1.

In both the recorders, the jet fluctuation centers at the edge were around $\overline{\eta}/h = -0.4$ and -0.5 at $U_0 = 20$ and 35 m/s respectively. The vertical positions of jet fluctuation center at the edge are almost the same in the two recorders. The actual jet offsets (relative height of $\overline{\eta}$ from the edge), $y_{a,e}$, are shown in Table 3.4. Since the edge height of the

straight-shaped recorder is higher than of the arch-shaped recorder (see Table 3.1), $|y_{a,e} / h|$ was about 0.1 larger in the straight-shaped recorder than in the arch-shaped recorder at both the jet velocities. The theoretical calculations for organ pipes [12, 87] have shown that the SPL of the second harmonic becomes intense with the increase of the absolute value of the jet offset within the range of the actual jet offset in the present cases ($|y_{a,e} / h| < 0.25$). This difference of $y_{a,e}$ due to the edge height can be a factor of the difference in the acoustic mode predominancy. This possibility is verified by an additional simulation in Sec. 3.6.2.

Table 3.4 Nondimensional actual jet offset.

U_0 [m/s]	Recorder	Actual jet offset $y_{a,e} / h$
20	Straight	−0.16
	Arch	−0.06
35	Straight	−0.23
	Arch	−0.12

3.6.1.B. Phase of Jet and Pressure

Table 3.5 shows the initial amplitudes and the time delays of the fluid dynamic and the acoustic jet displacement at the exit. The time delay of the fluid dynamic to the acoustic jet displacement was in the range of $t_{0,n} / T_n = 0.6\text{-}0.75$ for both the first and the second mode of the two recorders. Although the two displacements were not completely in the opposite phase, the sign of the fluid dynamic displacement can be opposite to that of the acoustic displacement. This supports the generation of a negative fluid dynamic fluctuations of the jet due to the acoustic particle fluctuations at the exit, as assumed in Fletcher's formula [9]. Also as seen in Table 3.5, at the exit, $A_{aco,n}$ can be comparable to $A_{fluid,n}$, indicating that the acoustic jet displacement is not negligible. The evaluation of

the acoustic jet displacement allows obtaining the net value of the convection velocity of the fluid dynamic jet displacement.

Table 3.5 Nondimensional blowing parameters in Eqs. (3.5)-(3.7).

U_0 [m/s]	Recorder	Mode n	Fluid dynamic jet displacement ($x = 0$)		Acoustic jet displacement ($x = 0$)
			Amplitude $A_{\mathrm{fluid},n} / h$	Time delay to acoustic displacement $t_{0,n} / T_n$	Amplitude $A_{\mathrm{aco},n} / h$
20	Straight	1	0.118	0.653	0.103
	Arch	1	0.070	0.608	0.081
35	Straight	1	0.093	0.750	0.166
		2	0.071	0.708	0.015
	Arch	1	0.075	0.750	0.067
		2	0.042	0.675	0.001

The convection velocities ($U_{\mathrm{c},n}$) around the middle of the mouth opening ($x / h = 2.0$) were obtained from Eq. (3.8). Table 3.6 shows the convection velocities nondimensionalized with the maximum jet velocity at the exit ($U_{\mathrm{c},n} / U_{0,\max}$). The values of $U_{\mathrm{c},n} / U_{0,\max}$ varies from 0.4 to 0.64. These values are almost within the range of the convection velocities measured in Refs. [20, 23]; the obtained $U_{\mathrm{c},n} / U_{0,\max}$ seems to be reasonable.

Table 3.6 Nondimensional convection velocity around $x / h = 2.0$, where values are nondimensionalized with the maximum jet velocity at exit.

U_0[m/s]	Recorder	Mode n	Convection velocity $U_{c,n} / U_{0,max}$
20	Straight	1	0.545
	Arch	1	0.502
35	Straight	1	0.569
		2	0.640
	Arch	1	0.435
		2	0.566

Table 3.7 shows the phase difference between the fluid dynamic displacement of the jet at the edge ($\eta_{\mathrm{fluid},n}(l,t)$) and the pressure oscillations in the resonator ($p'_n(t)$), which corresponds to $-(t_{c,n}(l) + t_{0,n} + t_{aco,n}) / T_n$ based on Eq. (3.6). This phase difference relates to the threshold for the acoustic power generation [2] and the anti-phase relation is favorable [11], as described in Sec. 2.2.1.A. The phase difference varies from 0.33 to 0.52. This range is within the threshold for the acoustic power generation of 0.25-0.75 [2]. The results for the first and the second mode at $U_0 = 35$ m/s support the multi-mode resonances in the two recorders, shown in Fig. 3.5. However, since the convection velocity is almost the same in the recorders, this seems to affect little the difference in the acoustic mode predominancy.

Table 3.7 Phase difference of the fluid dynamic jet displacement at the edge from the pressure oscillation in resonator.

U_0 [m/s]	Recorder	Mode n	Phase difference $-(t_{c,n}(l) + t_{0,n} + t_{aco,n}) / T_n$
20	Straight	1	0.36
	Arch	1	0.33
35	Straight	1	0.34
		2	0.52
	Arch	1	0.33
		2	0.48

3.6.1.C. Acoustic Feedback Effect on Jet

The acoustic feedback effect on the jet was evaluated based on the nondimensional amplitude of the fluid dynamic jet displacement ($\eta_{\mathrm{fluid}.n}$) to the acoustic particle displacement (ξ_n), $\left|A_{\mathrm{fluid},n} \,/\, \left(\sqrt{2}V \,/\, \omega_n\right)\right|$. Figure 3.15 shows the spatial variation of the nondimensional amplitude of $\eta_{\mathrm{fluid}.n}$. The jet receives the acoustic feedback mainly around the exit [13, 72]. Since the value of $\left|A_{\mathrm{fluid},n} \,/\, \left(\sqrt{2}V_{\mathrm{RMS},n} \,/\, \omega_n\right)\right|$ at the exit are almost the same in the two recorders, the acoustic feedback effect in the two seems to be almost the same; thus, this affect little the difference in the acoustic mode predominancy. The acoustic feedback effect possibly depends on the velocity profile at the exit [20, 44]. In the two recorders, the acoustic feedback induces the initial amplitude of the fluid dynamic displacement at almost the same magnitude probably because that the velocity profiles at the exit are similar (see Fig. 3.8).

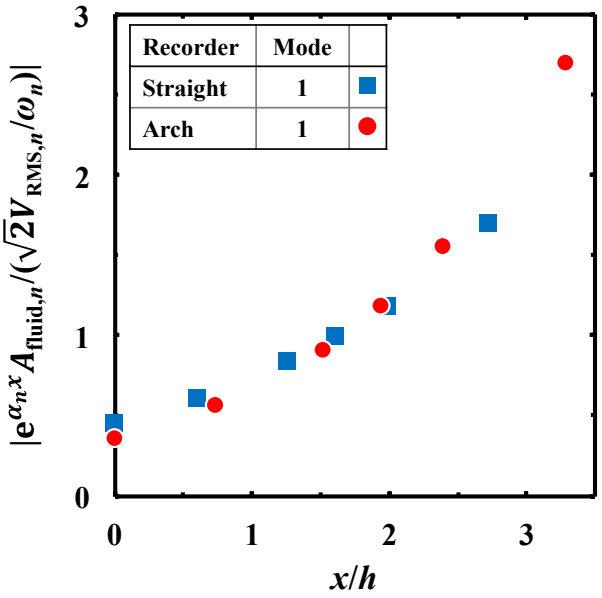

(a) $U_0 = 20$ m/s

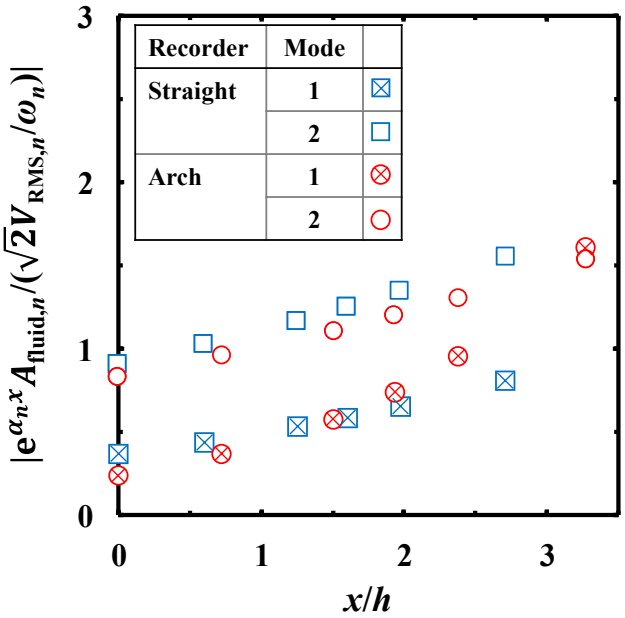

(b) $U_0 = 35$ m/s

Figure 3.15 Spatial variations of the nondimensional amplitude of the fluid dynamic jet displacement to the acoustic particle displacement.

3.6.1.D. Amplification of Jet

Figure 3.16 shows the nondimensional amplitude of the second to the first mode of jet displacement at the edge ($x / l = 1.0$), $|\eta_{\text{amp},2}| / |\eta_{\text{amp},1}|$, where this displacement includes both the fluid dynamic and the acoustic jet displacement. The nondimensional amplitude of the second mode is larger in the straight-shaped recorder than in the arch-shaped recorder. This relative intensification of the second mode can relatively promote the acoustic power generation of the second mode, which can contribute to the predominance of the radiation of the second acoustic mode.

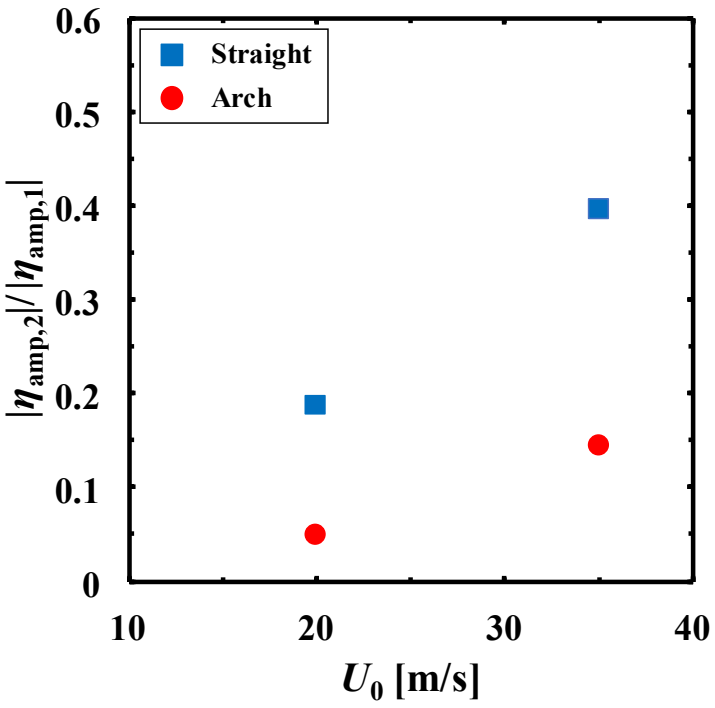

Figure 3.16 Relative amplitude of the second to the first mode of the jet displacement at the edge ($x / l = 1.0$).

Figure 3.17 shows the spatial variations of the fluid dynamic jet amplitude nondimensionalized with the exit height, $|e^{\alpha_n x} A_{\text{fluid},n} / h|$. At $U_0 = 20$ m/s, $|e^{\alpha_n x} A_{\text{fluid},n} / h|$ of the first mode are almost the same in both the recorders. When U_0 increases to $U_0 = 35$ m/s, $|e^{\alpha_n x} A_{\text{fluid},n} / h|$ of the first mode decreases significantly in

the straight-shaped recorder, while it remains almost the same magnitude in the arch-shaped recorder. At $U_0 = 35$ m/s, $\left|e^{\alpha_n x} A_{\text{fluid},n} / h\right|$ of the second mode is larger in the straight-shaped recorder than in the arch-shaped recorder. Thus, the relative $\left|e^{\alpha_n x} A_{\text{fluid},n} / h\right|$ of the second to the first mode at $U_0 = 35$ m/s is larger in the straight-shaped recorder. Since the fluid dynamic jet fluctuations are dominant to the acoustic jet fluctuations near the edge, this difference in the relative $\left|e^{\alpha_n x} A_{\text{fluid},n} / h\right|$ of the second mode between the recorders seems to produce the difference in $\left|\eta_{\text{amp},2}\right| / \left|\eta_{\text{amp},1}\right|$.

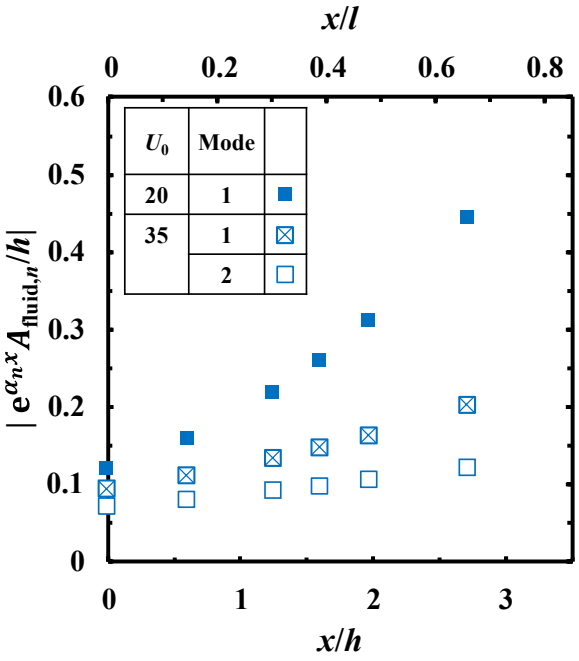

(a) Straight-shaped recorder

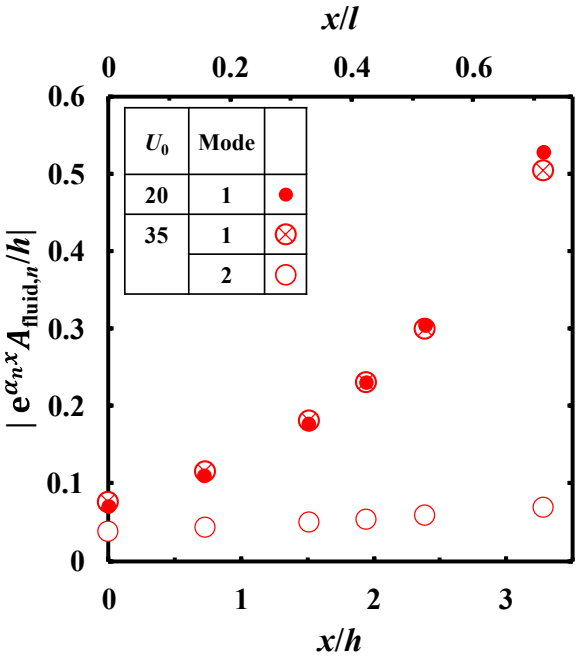

(b) Arch-shaped recorder

Figure 3.17 Spatial variations of the fluid dynamic jet amplitude nondimensionalized with the exit height.

The fluid dynamic jet amplitude grows in the streamwise direction with the amplification rate, α_n. Figure 3.18 shows the relationship between the Strouhal number $\mathrm{Str}_h \equiv f_1 h / U_{0,\max}$ and the amplification rate nondimensionalized with the exit height, $\alpha_n h$. Theoretical analysis [58] and experiments [20] have shown that $\alpha_n h$ draws a convex curve. In Fig. 3.18, the nondimensional amplification rate changes from increase to decrease with Str_h. Assuming that $\alpha_n h$ draws a convex curve, the curve for the straight-shaped recorder seems to locate in a higher-frequency region than for the arch-shaped recorder. This means that the peak of $\alpha_n h$ for the straight-shaped recorder appears at a lower jet velocity. Therefore, when U_0 increases 20 to 35 m/s, the amplification rate for the first mode decreases more in the straight-shaped recorder, resulting in the increase of the relative $\left|e^{\alpha_n x} A_{\mathrm{fluid},n} / h\right|$ of the second mode.

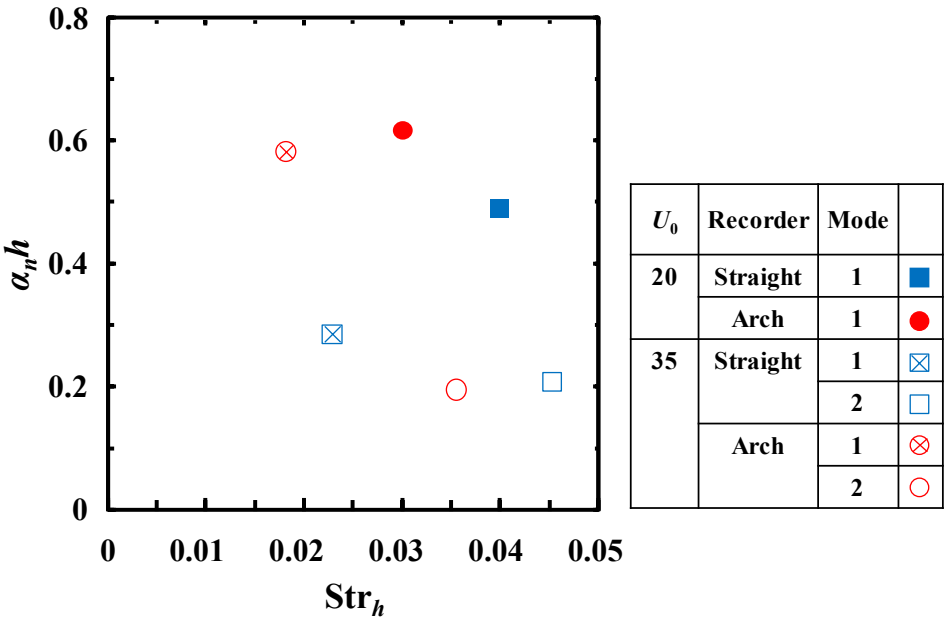

Figure 3.18 Relation between the amplification rate nondimensionalized with the exit height and Str_h

The jet visualization for flute-like instrument models with different windway lengths and chamfers [20] have shown that the amplification rate does not seem to depend on the

channel length but chamfer shapes. Based on this, the difference in the amplification rate in the current study is probably caused by the differences of the exit shape (straight- or arch-shaped).

To investigate the cause of the difference in the amplification rate, Fig. 3.19 shows the time-averaged velocity distribution in the spanwise direction at the exit ($x / l = 0$) and near the edge ($x / l = 0.8$) under the condition of $U_0 = 35$ m/s, where the streamwise velocity is nondimensionalized with the maximum velocity at the exit, $\bar{U} / U_{0,\max}$. In the straight-shaped recorder, near the edge, the lower side of the distribution is curved toward the resonator. Since the upper side keeps a flat shape similar to the distribution at the exit, the lower side curved due to the effect of the acoustic oscillations in the resonator. The arch-shaped recorder keeps the arched curve on both sides of the distribution, even near the edge. The instability seems to appear more in the jet in the straight-shaped recorder; therefore, the fluctuations at higher modes become predominant at lower velocity in the straight-shaped recorder than in the arch-shaped recorder. However, the reason why the flat shape is more susceptible to the acoustic disturbances cannot be determined from the current results.

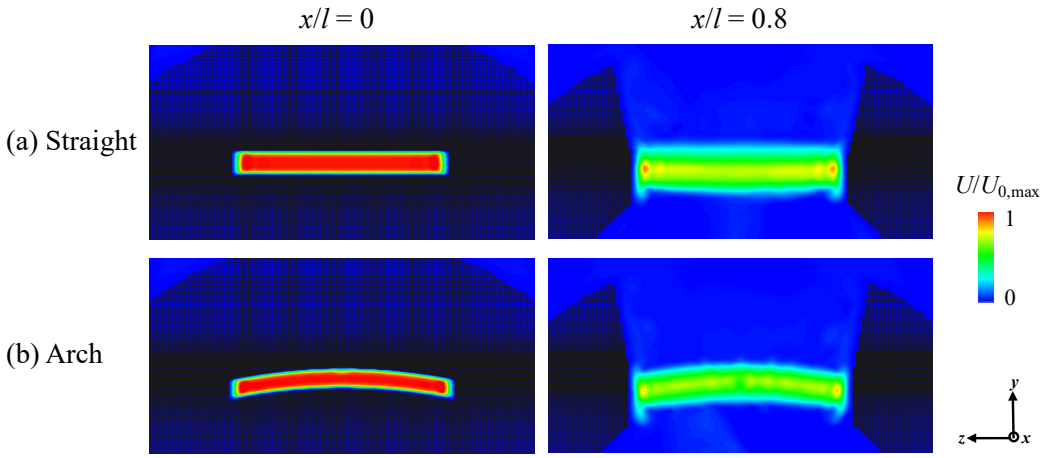

Figure 3.19 Time-averaged velocity distribution in the spanwise direction at the exit ($x / l = 0$) and near the edge ($x / l = 0.8$) under the condition of $U_0 = 35$ m/s, where the streamwise velocity is nondimensionalized with the maximum velocity at the exit, $\bar{U} / U_{0,\max}$.

3.6.2. Additional Computation

From the results in Sec. 3.6.1, the difference in the jet offset and the amplification rate possibly contribute to the difference in the acoustic mode predominancy between the two recorders, where the phase relationship and the feedback effect were almost comparable in the two recorders. The jet offset and the amplification rate mainly depend on the edge height and the exit shape (straight- or arch-shaped), respectively. To verify which of them affect more on the mode predominancy, an additional simulation for a recorder was performed. The recorder for the simulation is called P-arch and has the arch-shaped windway and edge as in the arch-shaped recorder, while its dimensions (*i.e.*, the edge height, the exit height and the exit-edge distance) are the same as those of the straight-shaped recorder. The jet velocity was $U_0 = 35$ m/s.

The radiated sound from the P-arch is shown in Fig. 3.20. The SPLs of the first and the second acoustic mode of the P-arch recorder are almost comparable to those of the arch-shaped recorder. From this result, the differences of the exit shape (straight- or arch-shaped) probably contribute more on the difference in the mode predominancy rather than the dimensions including the edge height.

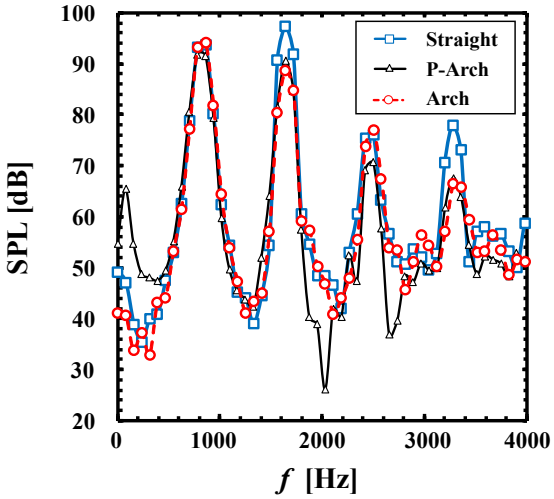

Figure 3.20 Sound pressure spectra under the condition of $U_0 = 35$ m/s ($x = 0$ mm, $y = 90$ mm, $z = 0$ mm).

3.7. Conclusion

This chapter proposed an analytical method for quantifying jet fluctuations. This method was applied to the two recorders that differ in the acoustic mode predominancy. The flow and the acoustic fields in the two recorders were predicted by direct aeroacoustic simulations. The first and the second mode of the jet fluctuations were represented by the formula proposed by modifying Fletcher's formula [9] based on the current computational results. By these, the jet fluctuations were decomposed into the fluid dynamic and the acoustic oscillations, and the values of the jet characteristics, *viz*., the phase condition between the jet and the pressure, the amplitude of jet fluctuations at the edge, the jet offset, and the acoustic feedback effect, were quantified to compare them between the two recorders. From the results of quantifications and the additional computation, the difference in the exit shape between the recorders seems to mainly contribute to the difference in the acoustic mode predominancy. The quantification of jet fluctuations by the proposed formula allowed to investigating the mechanism for sound changes. Since the sounding mechanisms in flute-like instruments are similar, the computational method and the formula may be applicable to other flute-like instruments. For the applications, sufficient accuracy of data is required to capture the initial jet fluctuations at the exit and the jet fluctuations at the mode to be analyzed. When the formula is applied to experimental results, it may be required to estimate the jet fluctuations around the exit. Also, the proposed formula represents the jet fluctuations, which is the result of receiving acoustic feedback. Quantifying the interaction between the flow and the acoustic field requires further investigations on the amount of work done by the flow and the acoustic field, which is a future work.

4. Effects of Blowing Parameters on Harmonic Structure and Jet Fluctuations in the Flute

4.1. Introduction

This chapter shows the effects of the blowing parameters, the jet offset, the exit-edge distance, and the flow rate, on the harmonic structure. Also, the mechanism whereby the harmonic structure changes with the jet angle is discussed in terms of both the radiated sound and the flow field. In the experiments, an actual blowing condition is measured for a human player by the Schlieren method. With reference the measured condition, the blowing parameters are varied independently using an artificial blowing device. The flow field is measured with a hot-wire anemometer. These measurements are conducted on a flute head joint. To confirm the generality of this study, the radiated sound is also measured for a flute with a body and a foot joint.

4.2. Chapter Layout

The definitions of the blowing parameters are shown in Sec. 4.3. The experimental methods for measuring a blowing condition of a human player are shown in Sec. 4.4.1. The experimental methods for measuring the radiated sounds and the flow fields are shown in Sec. 4.4.2. Based on the results, the effects of the jet angle on harmonic structure are compared with those of other blowing parameters in Sec. 4.5.1. The mechanism whereby the harmonic structure changes with the jet angle is discussed in Sec. 4.5.2. The radiated sound is also measured for a flute with a body and a foot joint in Sec. 4.5.3.

4.3. Blowing Parameters

The geometrical relationship between the jet and the flute depends on the following blowing parameters: the jet angle, θ_j, the jet offset from the edge, $y_{j,e}$, and the exit-edge distance, l [38]. The definitions of the blowing parameters for the measurements are shown in Fig. 4.1, based on the definitions in Sec. 1.4.1. The parameters are defined on the center plane of the mouth opening in the longitudinal direction of the flute ($z_j = 0$), as shown by AA' line in Fig. 4.1(a). The exit-edge distance is the distance from the cavity exit center (o_j) to the edge. The jet angle (θ_j) and the jet offset ($y_{j,e}$) are defined based on the reference jet direction measured without a flute head joint in the preliminary experiments described below. The jet angle (θ_j) is the angle between the horizontal line of the mouth opening and the reference jet direction. The jet offset ($y_{j,e}$) is the value on the axis normal to the reference jet direction, where the origin is at the edge and outside the edge is positive ($y_{j,e} > 0$). The reference jet direction is the x_j-axis, its vertical direction is the y_j-axis, and the longitudinal direction of the flute is the z_j-axis. The origin (o_j) is the center of the cavity exit, where this origin is on the line connecting the ending point of the cavity taper. The values on the axes are nondimensionalized with the throat height of the cavity exit, h. The z_j-direction centers of the mouth opening and the cavity exit are on the same plane ($z_j = 0$). The shape of the edge is thicker than that of recorders.

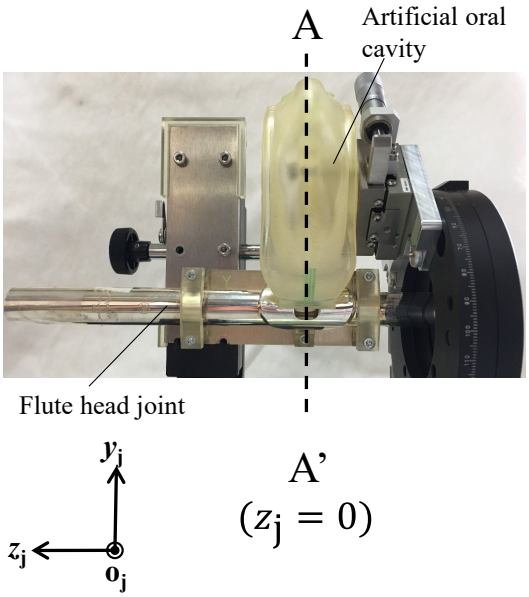

(a) Whole view of artificial oral device

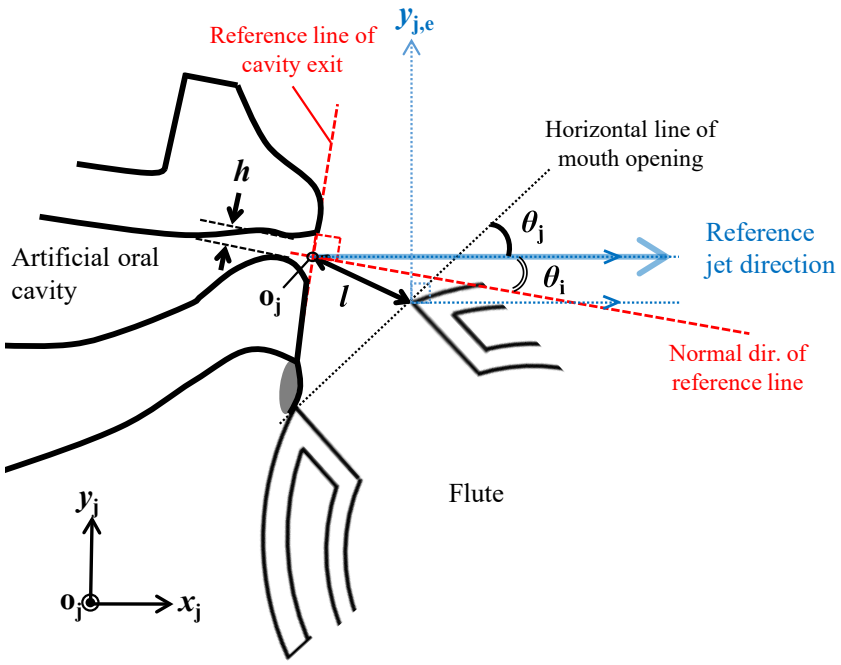

(b) AA' view ($z_j = 0$)

Figure 4.1 Definition of blowing parameters.

The reference jet direction was measured without an instrument in preliminary experiments by a pitot-tube (see Fig. 4.2). In this figure, the measurement direction of the

pitot-tube is the y_{pt}-axis, its vertical direction is the x_{pt}-axis, and the origin is the cavity exit center (o_j). The measurement line was $x_{pt}/h = 1.0$. The artificial oral cavity was initially set at the state that the reference line of cavity exit, which connects the tips of the upper and the lower lip, is parallel to the y_{pt}-axis. The jet velocities were measured by tilting the artificial oral cavity to change the angle of the measurement line with respect to the reference line of cavity exit $\theta_i = 12°$ to $15°$. Figure 4.3 shows the measured velocity profile by the pitot-tube, U_{pt}, where U_0 is the cross-sectional mean jet velocity at cavity exit in Table 4.1. The profile for $\theta_i = 14°$ is symmetrical with respect to $y_{pt}/h = 0$, which indicates that the reference jet direction is inclined at $\theta_i = 14°$ to the normal direction of the reference line of cavity exit.

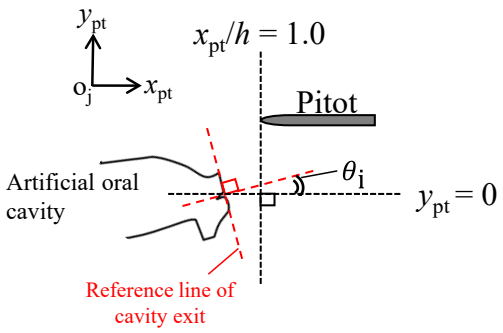

Figure 4.2 Measurement for reference jet direction.

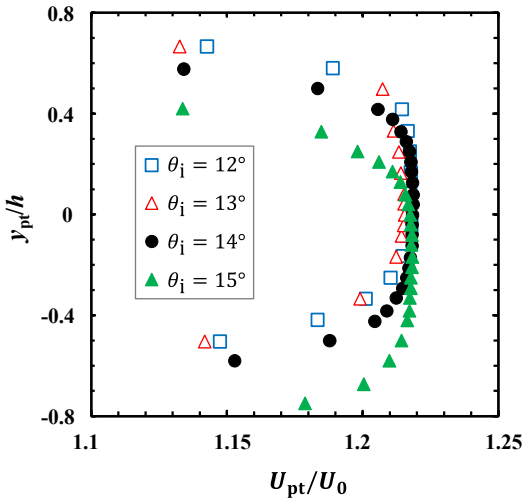

Figure 4.3 Velocity profile measured without instrument at $x_{pt}/h = 1.0$.

4.4. Experimental Methods

4.4.1. Measurements of Actual Blowing Condition

An actual blowing condition was measured for a human player. Since blowing conditions can vary depending on several factors, one of the conditions that can occur during playing was investigated to determine a reference condition.

The jet was visualized by the Schlieren method to estimate the jet angle (θ_j). Figure 4.4 illustrates the experimental setup. The Schlieren method allows visualization of the density variation of the flow field, in which light and dark areas in an image are produced by the variations in the refraction factor of light due to density variations [101]. A human player blew a flute head joint 4000 mm from a concave mirror. The beam was reflected on the concave mirror, bent 90° by a beam splitter, and cut off by a pinhole at the focal point to obtain a sharp and even image. The contrast between light and dark was photographed by a camera.

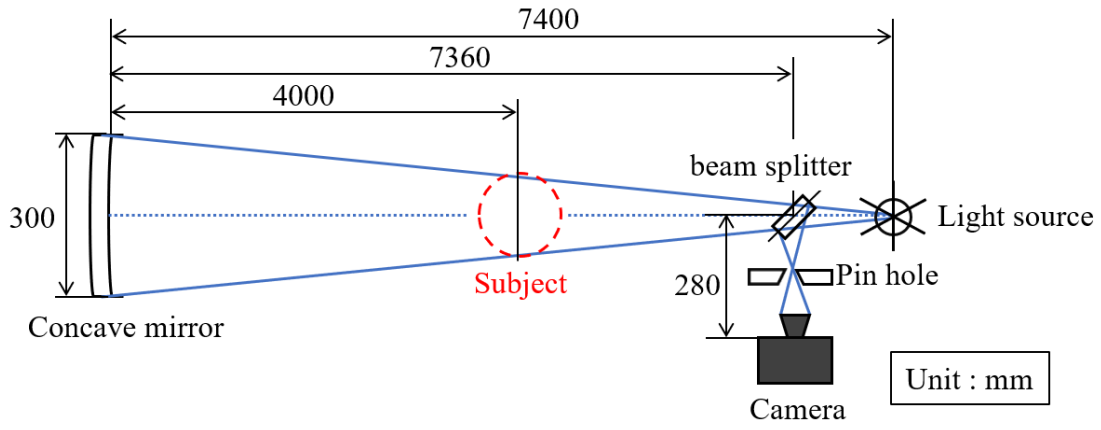

Figure 4.4 Experimental setup for Schlieren method.

Figure 4.5 shows the photographed Schlieren image of a human player. The head joint was fixed to a tool to ensure that the horizontal line of the mouth opening remained parallel to the reference line of mouth opening. To measure the reference jet direction

without the head joint, the player blew the fixed head joint at the dynamics of almost *mf* (mezzo forte), and then the head joint was slid into the horizontal direction of the mouth opening and released from the player's lips. During this time, the player kept the same blowing state. Schlieren images were taken after the radiated sound was stopped. Since there is a temperature difference between the air blown by a human and the ambient air, there is a density gradient around the jet. Due to the gradient, the jet appears black on the images, as shown in Fig. 4.5. The average jet angle for 6 images was $\theta_j = 39°$, with a variation, $\theta_{j,err}$, of $\pm 2°$.

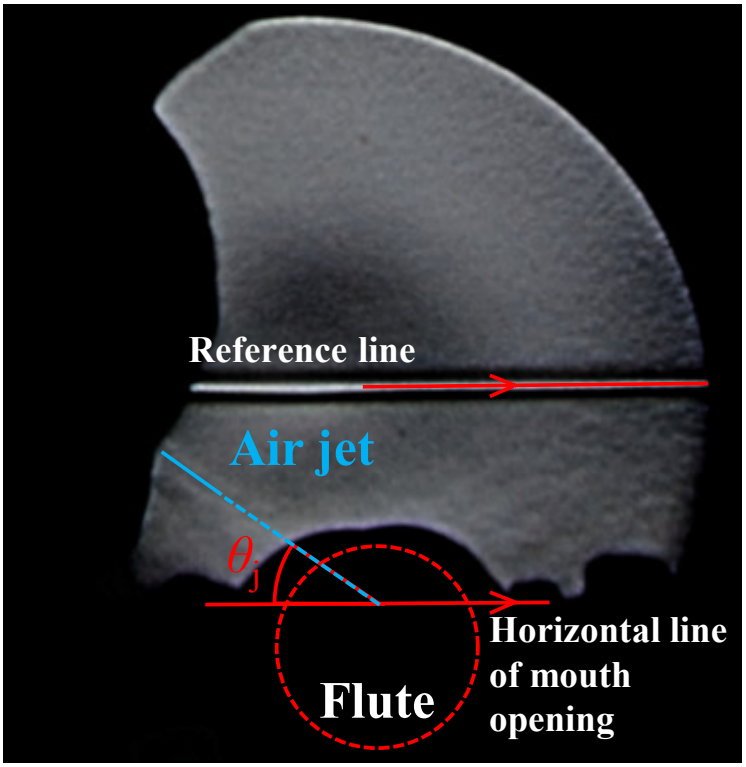

Figure 4.5 Jet visualization by Schlieren method.

The cavity exit height (h) and the exit-edge distance (l) were measured from photographs shown in Fig. 4.6. In the measurement for the exit height (h), photographs were taken from the front of the human player blowing the head joint (see Fig. 4.6 (a)). The height was found to be $h = 1.2 \pm 0.1$ mm. In the measurement for l, photographs of

the human player blowing the fixed head joint were taken from the side (see Fig. 4.6 (b)). Since the edge tip at $z_j = 0$ is hidden by the lip plate, the edge tip was determined on the basis of the tip position of a 15-mm-heigh strip of masking tape placed at $z_j = 0$. The exit-edge distance was found to be $l / h = 5.6 \pm 0.42$. The jet offset, which was calculated geometrically from θ_j and l, was $y_{j,e} / h = 0.24 \pm 0.25$.

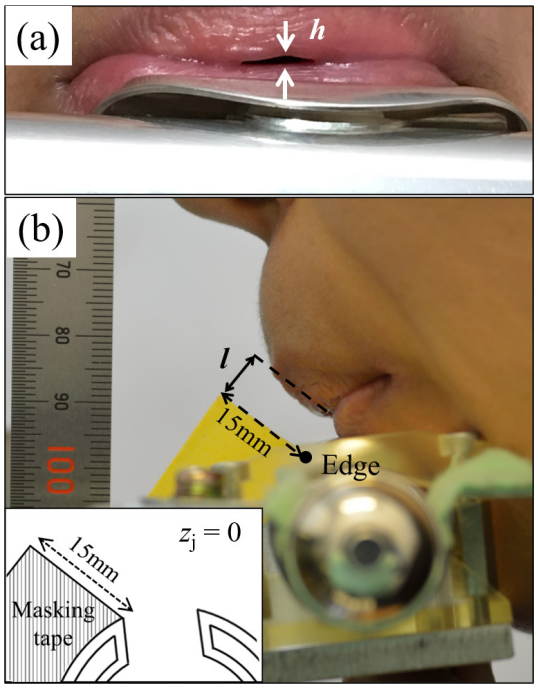

Figure 4.6 Photographic measurement for cavity exit height (a) and exit-edge distance (b).

The flow rate (Q) was adjusted so that the radiated sound of the artificial blowing device satisfies the following conditions when the blowing parameters for the device are set to the measured values ($\theta_j = 39°, y_{j,e} / h = 0.24, l / h = 5.6$): almost the same fundamental frequency with that of the sound blown by the human is reproduced, and ΔSPL ($\equiv$ SPL_2–SPL_3) is the closest to ΔSPL of the sound blown by the human.

The actual blowing condition is summarized in Table 4.1. The radiated sound spectra of the human and device are shown in Fig. 4.7, where the frequency resolution was 1.22

Hz, and the blowing parameters for the device were set to the values in Table 4.1. The fundamental frequency was well reproduced by the device. The values of ΔSPL were 18.7 and 3.9 dB for the human and the device, respectively. Within the range of the flow rate that the device almost reproduced the fundamental frequency of the sound blown by the human (16.0 - 20.0 L/min), the maximum ΔSPL of the device was 3.9 dB at $Q = 16$ L/min; therefore, the device's flow rate was adjusted to $Q = 16$ L/min. At this flow rate, the cross-sectional mean jet velocity at the cavity exit ($x_j = 0$), $U_0 (= Q / S_0)$, is 21.5 m/s, where $S_0 (= 12.4\ \text{mm}^2)$ is the area of the cavity exit. Experiments were performed with reference to the actual blowing condition in Table 4.1. These values and variations of the parameters are within the ranges shown in Refs. [20, 38, 54].

Table 4.1 Actual blowing condition and experimental range

Parameter	Actual blowing condition of human		Experimental range for device	Practical range
	Value	Variation		
Jet angle θ_j [º]	39	±2	35 - 90	35 - 65
Exit-edge distance l / h	5.6	±0.42	5.0 - 9.17	5.0 - 6.25
Jet offset $y_{j,e} / h$	0.24	±0.25	−0.83 - 1.5	0 - 1.5
Flow rate Q [L/min]	16.0	±2	2.0 - 38.0	16.0 - 20.0
Cavity exit height h [mm]	1.2	±0.1	1.2	
Cross-sectional mean jet velocity at cavity exit $U_0 (= Q / S_0)$ [m/s]	21.5	±2.7	2.69 - 51.1	21.5 - 26.9

S_0 [m^2]: Cavity exit area

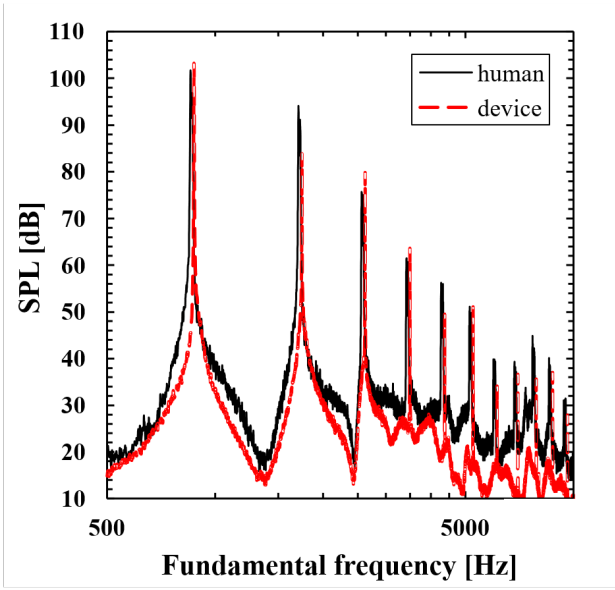

Figure 4.7 Sound pressure spectra of radiated sound produced by human player and artificial blowing device, where blowing parameters for the device were set to the values in Table 4.1 ($\theta_j = 39°, y_{j,e} / h = 0.24, l / h = 5.6, Q = 16$ L/min).

4.4.2. Measurements of Acoustic and Flow Field

4.4.2.A. Artificial Blowing

This study used the artificial blowing device [102] shown in Fig. 4.8. Using this device, the blowing parameters were varied independently within the experimental range shown in Table 4.1. A flute head joint and an artificial oral cavity are installed on the device. The fundamental frequency of the head joint is around 880 Hz, and this head joint model is the same as in Ref. [102]. The cavity was fabricated with a 3D printer from MRI images around the oral cavity of a human player blowing a plastic head joint. Since the cavity is made of plastic, shapes of the cavity, including h and S_0, are constant. In actual performances by human players, the cavity shapes can change during playing; however, in this study, the cavity shapes were fabricated to be constant to investigate the effects of the blowing parameters independent from the cavity shapes. Between the cavity and the head joint, there is a gap, whose size depends on blowing conditions (see Fig. 4.8 (b)). In preliminary experiments, the radiated fundamental frequency obtained without covering

the gap was about 25 Hz higher than the fundamental frequency range measured for a human (875 – 885 Hz), whereas it was within this range when a seal was placed on the gap. Further, the seal made of aluminum tape and clay shown in Fig. 4.8 (b) was found to be better to reproduce the fundamental frequency range and assure the reproducibility of experiments than a seal made of silicon, clay, or tape. For these reasons, the seal made of aluminum tape and clay was placed on the gap. In an actual performance by a human, part of the lower lip interferes with (occludes) the mouth opening of the flute. Thus, the opening area of the mouth depends on blowing conditions. This opening area can affect the radiation impedance around the mouth and the fundamental frequency [48]. To avoid these effects, the seal corresponding to the size of gap was positioned not to interfere with the mouth opening. In three experiments, the reproducibility of sound was about ±4 Hz (0.5%) in terms of the fundamental frequency and about ±1 dB in terms of the SPLs of the fundamental frequency and the second and the third harmonic.

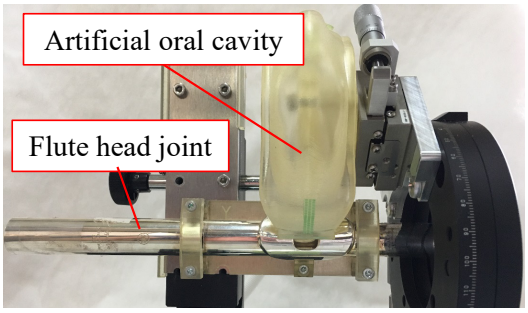

(a) Front view

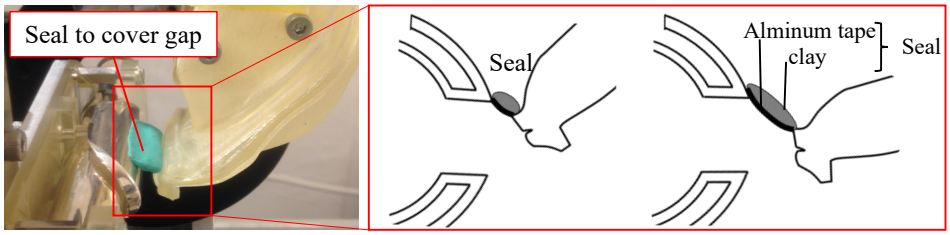

(b) Side view Small jet angle Large jet angle

(b) Side view

Figure 4.8 Experimental setup for artificial blowing.

Figure 4.9 illustrates the experimental setup. The air supplied from the compressor (PAOCK SOL-2039) was depressurized to the experimental pressure value with a precision regulator (SMC IR2000). The air was supplied into the artificial oral cavity through a needle valve (KOFLOC 2412), a flowmeter (SMC PFM750S-01-C-M), and a pressure gauge (SMC ZSE30AF-01-C-L).

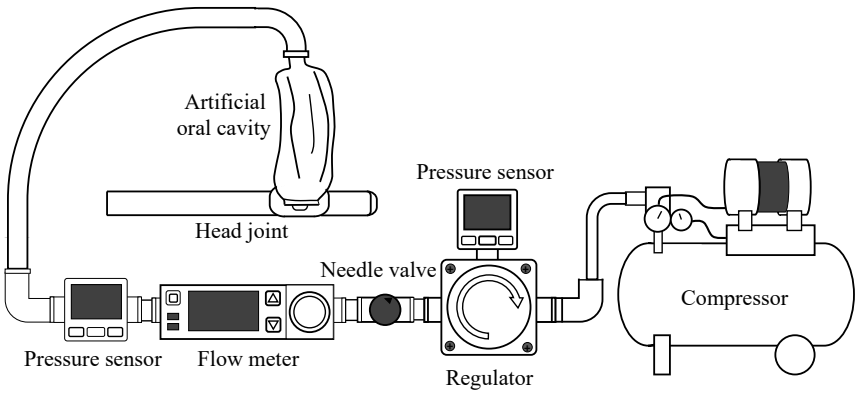

Figure 4.9 Schematic of artificial blowing.

4.4.2.B. Measurement Methods

The radiated sound was measured with a 1/2-inch omnidirectional microphone (RION UC-53A) positioned at 100 mm from the resonator end and a precision sound level meter (RION NL-31). The measurements for sound were performed three times for each blowing condition.

The velocity around the mouth opening was measured with a hot-wire anemometer. The probe was an I-type probe with a tungsten wire 5 μm in diameter and 1 mm in length. The wire was parallel to the spanwise (z_j) direction of the cavity exit; thus, the measured velocity was the absolute value of the synthetic vector of the streamwise (x_j) and the vertical (y_j) direction velocities. The measurement lines were $x_j / h = 1.0$, 2.0, and 5.0. The measurements with the hot-wire anemometer were performed under the conditions of three jet angles: $\theta_j = 39°$, which is the actual blowing condition, $\theta_j = 65°$, which is the upper limit of the practical range, and $\theta_j = 50°$, which is an angle between them. The

jet offset was fixed to zero, and the other blowing parameters were fixed to the actual blowing condition.

Tables 4.2 to 4.4 shows the measurement conditions for the radiated sound and the velocity. The results of Fourier transform were averaged 72 times.

Table 4.2 Measurement conditions for radiated sound

Condition	Value
Sampling frequency [Hz]	40000
Sampling time [s]	30
Averaging number N_{ave}	72
Frequency resolution for Fourier transform [Hz]	1.22

Table 4.3 Measurement conditions for velocity

Condition	Value
Minimum resolution of sampling [mm]	0.07 ($y_j / h = 0.058$)
Sampling frequency [Hz]	80000
Sampling time [s]	30
Averaging number N_{ave}	72
Frequency resolution for Fourier transform [Hz]	1.22

Table 4.4 Blowing condition for measurements with hot-wire anemometer

Parameter	Value
Jet angle θ_j [°]	39, 50, 65
Exit-edge distance l / h	5.6
Jet offset $y_{j,e} / h$	0
Flow rate Q [L/min]	16.0
Cross-sectional mean jet velocity at cavity exit $U_0 (= Q / S_0)$ [m/s]	21.5

To obtain periodical fluctuations of jet, the velocity measured with the hot-wire anemometer was phase averaged with reference to the pressure fluctuations of radiated sound. In a preliminary operation, the pressure fluctuation in the resonator nondimensionalized with the amplitude, $p'_{\mathrm{r}}(t) \,/\, p'_{\mathrm{r,amp}}$, was calculated from the pressure fluctuation of radiated sound based on the distance from the sound measurement point to the open end of the resonator ($z_{\mathrm{j}} = L$). The fundamental mode of $p'_{\mathrm{r}}(t) \,/\, p'_{\mathrm{r,amp}}$, $p'_{\mathrm{r,1}}(t) \big/ p'_{\mathrm{r,1,amp}}$, was extracted by the procedure described in Ref. [34]. The instant $t = 0$ is when $p'_{\mathrm{r,1}}(t) \big/ p'_{\mathrm{r,1,amp}}$ exhibits its minimum.

The obtained jet fluctuations were verified by comparing with results in preceding studies. Figure 4.10 shows that the velocity profiles at $x_{\mathrm{j}} \,/\, h = 1$ and 5. These profiles are top-hat-shapes (shapes similar to rectangular functions). Although parabolic profiles are observed in the computations for recorders [34] (see Fig. 3.8) under almost the same U_0, thinner shear layers are formed in the current oral cavity because the flow channel is shorter than the recorders. The line in each profile shows the displacement of jet, η, where η is defined as the distance from $y_{\mathrm{j,e}} = 0$ to the center of the half-value positions of the maximum velocity. The jet displacement (η) fluctuates outward and inward during each period.

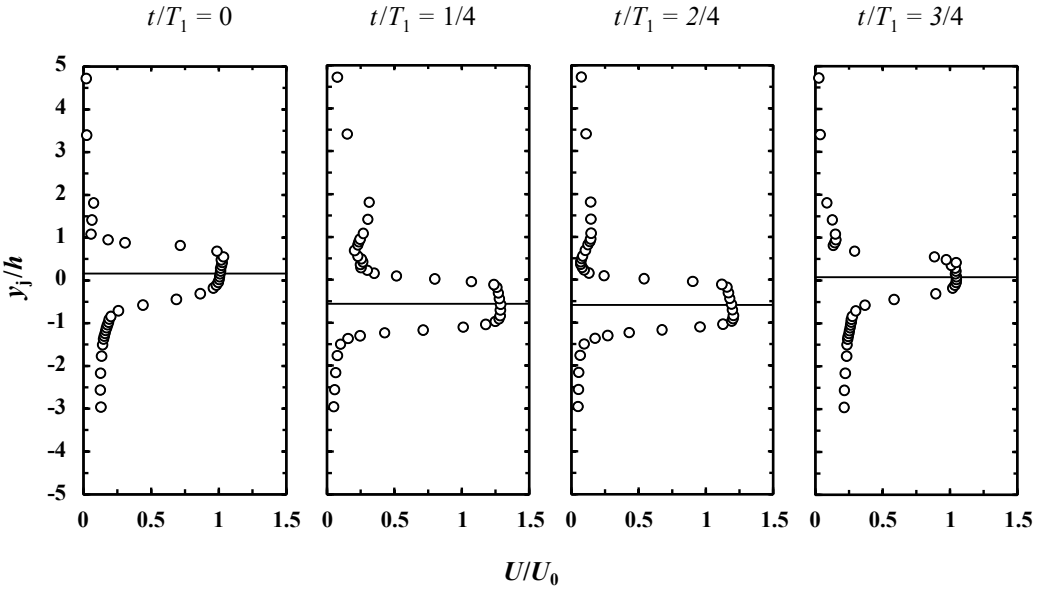

(a) $x_j / h = 1.0$

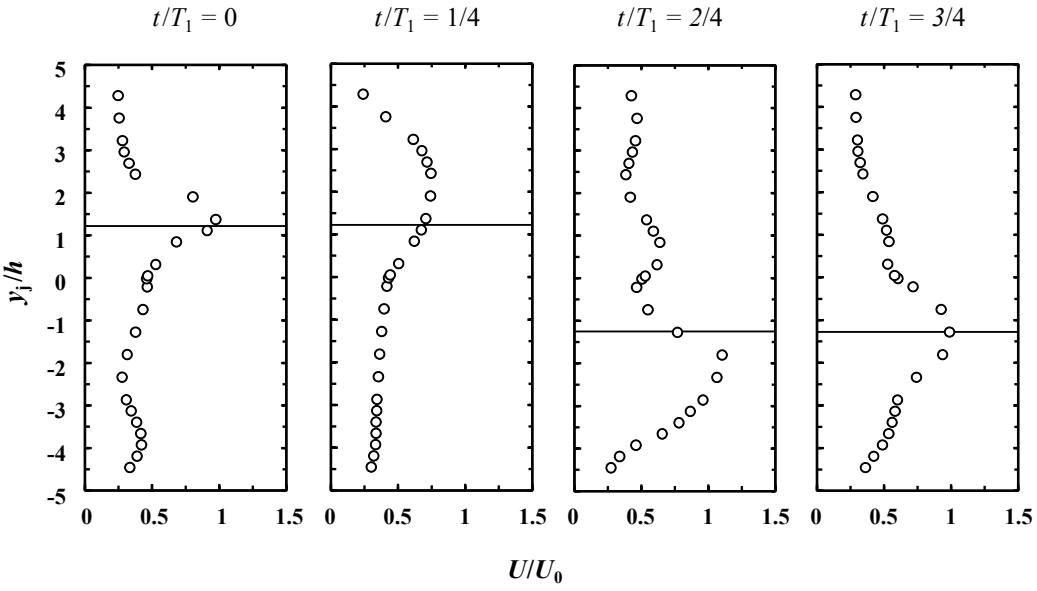

(b) $x_j / h = 5.0$

Figure 4.10 Periodical variations of velocity profiles, where the line in each profile shows the jet displacement (η). ($\theta_j = 39°,\ y_{j,e} = 0,\ l / h = 5.6,\ Q = 16$ L/min)

Figure 4.11 shows the periodical variations of jet displacement (η) at $x_j / h = 1$ and 5. The instant that η changes from increasing (decreasing) to decreasing (increasing) is delayed as the jet travels downstream (x_j increases) due to the convection of the jet fluctuations. The first mode of η was extracted by the same procedure in Ref. [34]. The convection velocity of the first mode of η, $U_{c,1}$, was estimated from the phase difference of the first modes of $\eta(t)$ between $x_j / h = 1$ and 5. The convection velocities were $U_{c,1} = 16.6$ m/s ($0.77U_0$), 16.5 m/s ($0.77U_0$), and 19.8 m/s ($0.92U_0$) for $\theta_j = 39°$, 50°, and 65°. The convection velocity is generally nondimensionalized with the maximum velocity at the exit, $U_{0,\max}$, [20, 23, 34, 63]. In the current experiments, $U_{0,\max}$ is unmeasurable because the cavity exit was too narrow to insert the probe; therefore, $U_{0,\max}$ was estimated from the reduction ratio of the maximum jet velocity between $x_j / h = 1$ and 2, $(U_{1h,\max} - U_{2h,\max}) / h$. The nondimensionalized convection velocity, $U_{c,1} / U_{0,\max}$, were respectively estimated to be 0.34 for $\theta_j = 39°$ and 50°, 0.65 for $\theta_j = 65°$. These values are almost within those in Refs. [20, 23, 34, 63].

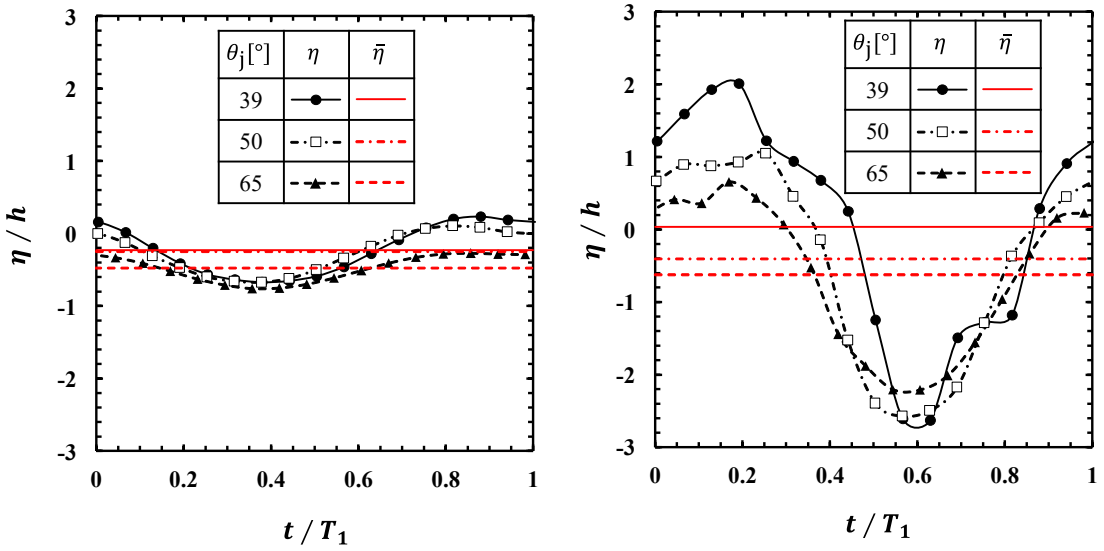

(a) $x_j / h = 1$ (b) $x_j / h = 5$

Figure 4.11 Periodical variations of jet displacement (η) at $x_j / h = 1$ and 5. ($y_{j,e} = 0$, $l / h = 5.6$, $Q = 16$ L/min)

Figure 4.12 shows the oscillations of jet displacement at the first mode nondimensionalized with the amplitude at the edge ($x_j / h = l / h$), $\eta_1(l,t) / \eta_{1,amp}$. These oscillations were estimated from the first modes of η at $x_j/h = 5$ by assuming that $U_{c,1}$ is constant between $x_j / h = 1$ and l / h. This figure also shows the nondimensional pressure oscillation at the first mode ($p'_{r,1}(t) / p'_{r,1,amp}$). The phase delays of $\eta_1(l,t) / \eta_{1,amp}$ from $p'_{r,1}(t) / p'_{r,1,amp}$ were 245°, 230°, and 225° for $\theta_j = 39°$, 50°, and 65°, respectively. The phase differences, 225° to 245°, are within the threshold for the acoustic power generation at 90°-270° [51] (see Sec. 2.2.1.A). By using the seal not to interfere with the mouth opening (see Fig. 4.8(b)), the acoustic power generation for the fundamental tone seems to be largely unaffected by changing the jet angle.

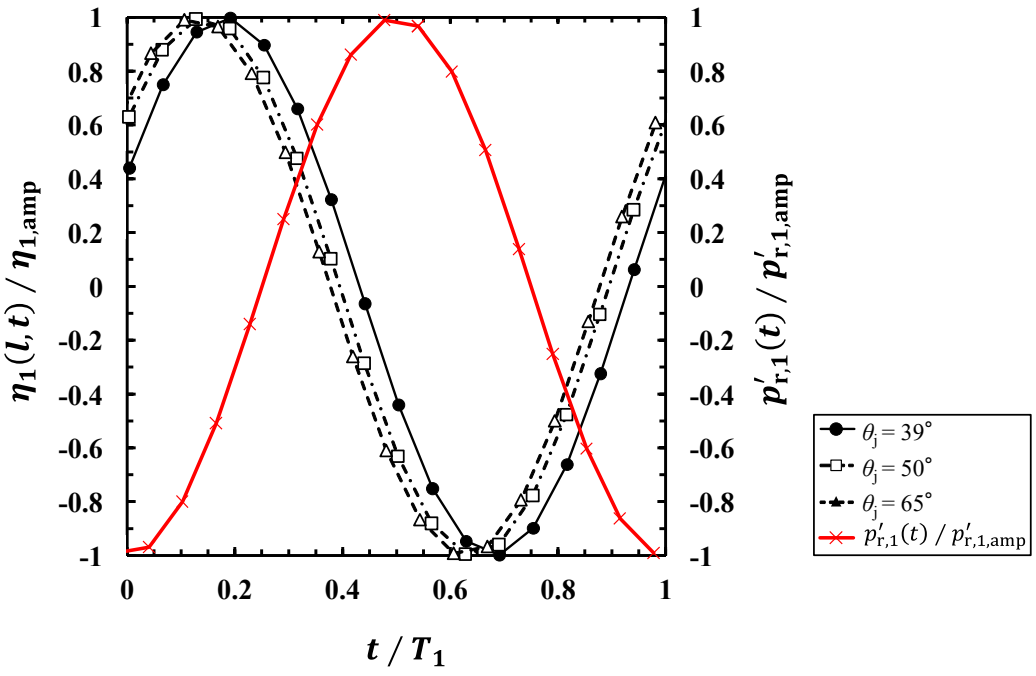

Figure 4.12 Estimated periodical variations of the first mode of η at the edge ($x_j / h = l / h$) and the pressure in the resonator (p'_r). ($y_{j,e} = 0$, $l / h = 5.6$, $Q = 16$ L/min)

The measurements for different channel length and shapes in Ref. [20] showed that the convection velocity depends mostly on the shear layer formation in the channel and increases when the jet gets sharper. To confirm the consistency between the changes of the velocity profile and the convection velocity, Fig. 4.13 shows the time-averaged velocity profile near the cavity exit ($x_j / h = 1.0$). The vertical axes show the relative height from the time average of η (jet fluctuation center), $\bar{\eta}$. The widths of 50% height of profile are $1.49h$ $1.37h$ and $1.26h$ for $\theta_j = 39°$, $50°$, and $65°$. The shear layer at $\theta_j = 65°$ is thinner than at $\theta_j = 39°$, $50°$. The velocity profile near the exit changes with the jet angles possibly because the jet may be affected by the acoustic oscillations. With increasing the jet angle, the channel becomes more vertical to the mouth opening (see Fig. 4.8(b)), which may change the effects of the acoustic oscillations on the jet near the exit. Since the shear layer at $\theta_j = 65°$ is thinner than the other jet angles, $U_{c,1} / U_{0,max}$, for $\theta_j = 65°$ is the largest. The convection velocities are consistent with the velocity profile. From these results, the periodical jet fluctuations obtained by phase averaging the measured velocity are a reasonable representation.

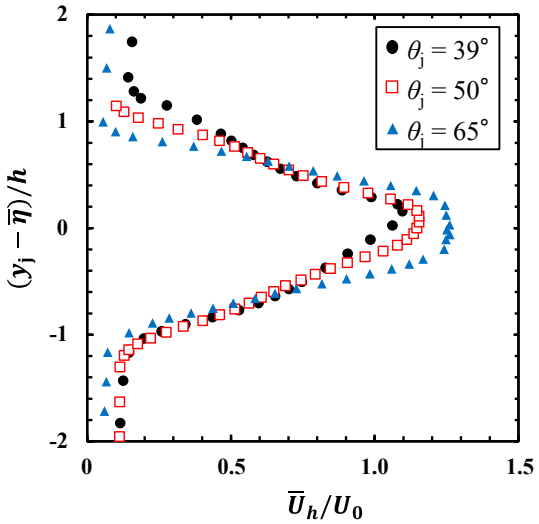

Figure 4.13 Time averaged velocity profiles at $x_j / h = 1$, where the vertical axes show relative height from the jet fluctuation center ($\bar{\eta}$). ($y_{j,e} = 0$, $l / h = 5.6$, $Q = 16$ L/min)

4.5. Results and Discussion

4.5.1. Effects of Blowing Conditions on Sound

This section shows the effects of blowing parameters, *viz*., the jet offset, the exit-edge distance, the flow rate, and the jet angle, on the harmonic structure. The harmonic structure is evaluated from ΔSPL ($\equiv$ SPL_2−SPL_3).

Figures 4.14 - 4.17 plots the variations of the SPLs of the fundamental frequency (SPL_1) and the second (SPL_2) and the third harmonic (SPL_3) with the blowing parameters. An error bar is shown for each measured value, which indicates the range of the measured value in three times of measurements. The second vertical axis shows ΔSPL. The line and the arrow in each figure indicate the actual blowing condition and the practical range in Table 4.1, respectively. All parameters other than the one being varied were fixed to the actual blowing condition. This study defined the practical range as that satisfying the following conditions in our experiments within the possible ranges shown in Refs. [20, 38, 54]: the SPL of the first acoustic mode is the largest, and the fundamental frequency is within ±10 cent of that radiated at the actual blowing condition. Compared to Refs. [20, 38, 54], the practical ranges for the parameters are limited. For example, human players can blow the flute with a lower jet velocity than the practical range in this study. This limitation is because the practical ranges were defined based on the current experiments under the condition that only a single parameter was varied independently, while Refs. [20, 38, 54] show the ranges for actual human playing.

Figure 4.14 shows the variation of harmonic structure with the jet offset ($y_{j,e}$). The variation of SPL_2 is almost symmetrical with respect to $y_{j,e} = 0$. This variation is consistent with the calculation [87] (see Sec. 2.3), which assumes a straight jet flow. Unlike SPL_2, the variation SPL_3 is not symmetrical with respect to $y_{j,e} = 0$. In $y_{j,e} > 0$ (the reference jet direction is directed to outside the edge), SPL_3 decreases as $y_{j,e}$ increases, while SPL_3 remains almost constant in $y_{j,e} < 0$. The condition under which SPL_3 remains almost constant is to be investigated in Sec. 4.5.2. Within the practical range ($0 \leq y_{j,e} / h \leq 1.5$), ΔSPL increases from about −1 to 28 dB as the jet offset increases.

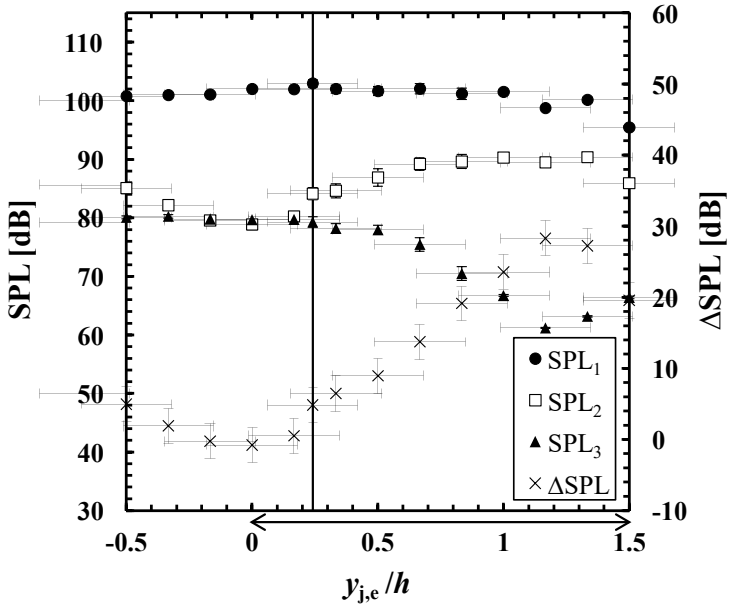

Figure 4.14 Variations of harmonic structure with the jet offset. Line and arrow show the actual blowing condition and the practical range, respectively. All parameters other than the one being varied were fixed to the actual blowing condition shown in Table 4.1 ($\theta_j = 39°, l/h = 5.6, Q = 16$ L/min). Error bar is shown for each measured value. $y_{j,e} > 0$ means that the reference jet direction is directed to outside the edge.

Figure 4.15 shows the variation of harmonic structure with the exit-edge distance (l). In $5.4 \le l/h \le 7.1$, SPL_1, SPL_2, and SPL_3 decrease with increasing the exit-edge distance. Around $l/h = 7.2$, which is outside the practical range, the fundamental frequency shifts from the first to the second acoustic mode. The exit-edge distance relates to the phase condition between the jet fluctuations at the edge and the pressure fluctuations in the resonator, $p_r(t)$. The phase delay of the jet fluctuations at the edge from $p_r(t)$ is approximated to be $\omega l / U_c$. The range of the nondimensional convection time for the acoustic power generation at the fundamental frequency is $0.25 < t_{c,1}/T_1 < 0.75$, where $t_{c,1}\left(= l/U_{c,1}\right)$ and T_1 are the convection time and the period of the fundamental frequency (see Sec. 2.2.1.A). As l/h increases from 5.4 to 7.2, $t_{c,1}/T_1$

is estimated to increase almost 0.1, where the convection velocity is assumed to be $U_{c,1} = 0.77U_0$ based on the estimation in Sec. 4.5.2. With this increase of l / h, SPL_1 decreases probably because t_c / T_1 deviates from the optimum condition ($t_c / T_1 = 0.5$). When $t_{c,1} / T_1$ is the upper limit of the range ($t_{c,1} / T_1 = 0.75$), the nondimensional convection time for the second mode of the jet oscillation $(t_{c,2} - T_2) / T_2$ is 0.5. There is a possibility that the nondimensional convection time $t_{c,1} / T_1$ probably becomes almost 0.75 at $l / h = 7.2$, and then the fundamental frequency shifted to the second acoustic mode, which is more appropriate phase condition than the first acoustic mode.

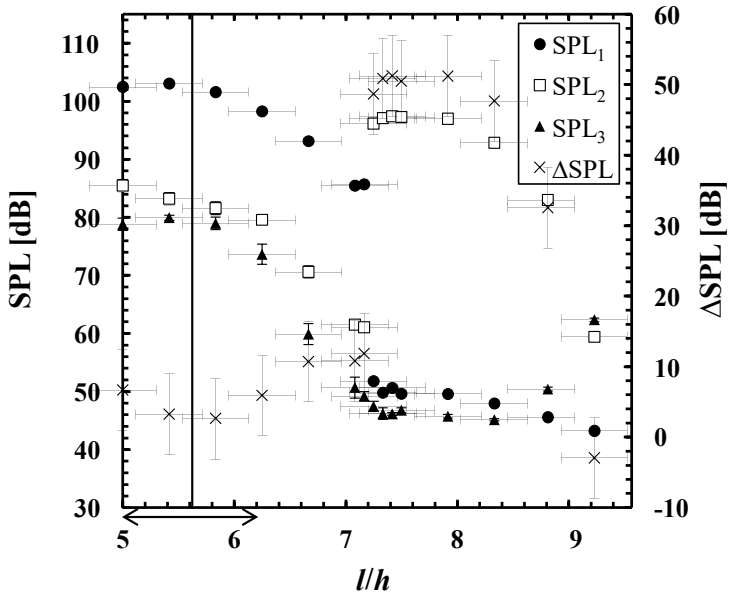

Figure 4.15 Variations of harmonic structure with the exit-edge distance. Line and arrow show the actual blowing condition and the practical range, respectively. All parameters other than the one being varied were fixed to the actual blowing condition shown in Table 4.1 ($\theta_j = 39°, y_j / h = 0.24, Q = 16$ L/min). Error bar is shown for each measured value.

Figure 4.16 shows the variation with the flow rate. SPL_1 and SPL_3 increase with increasing the flow rate in the practical range, while SPL_2 takes its minimum at 19 L/min.

Except for this local variation around $Q = 19$ L/min, SPL_2 also increases around the practical range. As the flow rate increases, the volume flow brought into the resonator increases to increase the SPLs. However, the local decrease of SPL_2 around $Q = 19$ L/min cannot be explained by the volume flow, because the volume flow increases continuously with Q. The nondimensional convection time of the second mode of the jet oscillations ($t_{c,2} / T_2$) was estimated from $U_0 (= Q / S_0)$, assuming $U_{c,2} = 0.77 U_0$. From this estimation, $t_{c,2} / T_2$ decreases 0.06 as the flow rate increases from $Q = 18$ to 20 L/min. The nondimensional convection time $t_{c,2} / T_2$ changes little in this range of Q and may not to be the cause of the local decrease of SPL_2. With increasing the jet velocity, the fluctuation center of the jet inclines [68]. As discussed later, the actual jet offset in the flow field is not always the coincidence with the jet offset defined without the head joint. Assuming that the actual jet offset changes with Q and becomes almost zero around $Q = 19$ L/min, SPL_2 and ΔSPL can exhibit their minimum around $Q = 19$ L/min. Except for the local decrease around $Q = 19$ L/min, ΔSPL remains almost constant in the practical range.

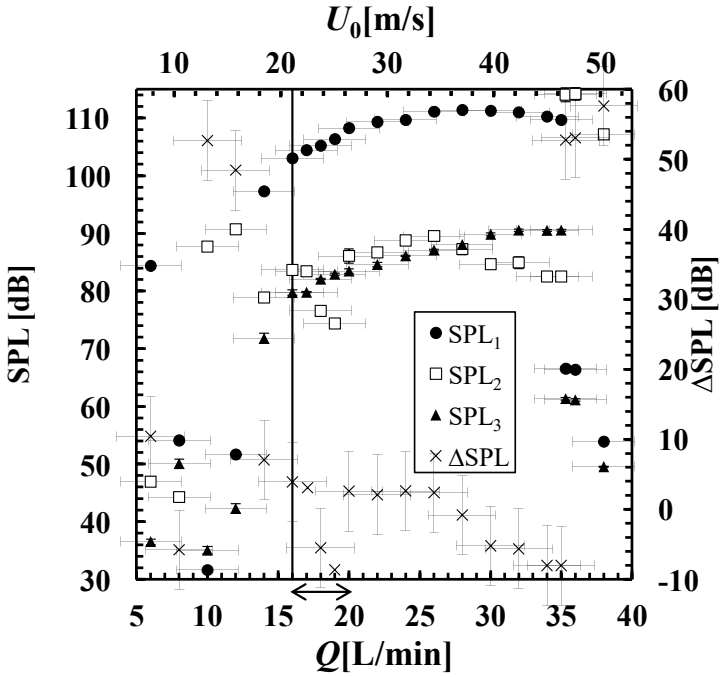

Figure 4.16 Variations of harmonic structure with the flow rate. Line and arrow show the actual blowing condition and the practical range, respectively. All parameters other than the one being varied were fixed to the actual blowing condition shown in Table 4.1 ($\theta_j = 39°, y_j / h = 0.24, l / h = 5.6$). Error bar is shown for each measured value.

Figure 4.17 shows the variation of harmonic structure with the jet angle. SPL_1 varies little with the jet angle; thus, the phase relation for the acoustic power generation seems to be largely unaffected. SPL_2 decreases with increasing the jet angle in $\theta_j < 45°$, while SPL_2 increases in $\theta_j > 45°$. SPL_2 changes about 10 dB with the jet angle, while SPL_3 changes about 3 dB. Since ΔSPL changes mainly due to the change of SPL_2 under this condition, ΔSPL exhibits its minimum at $\theta_j = 45°$.

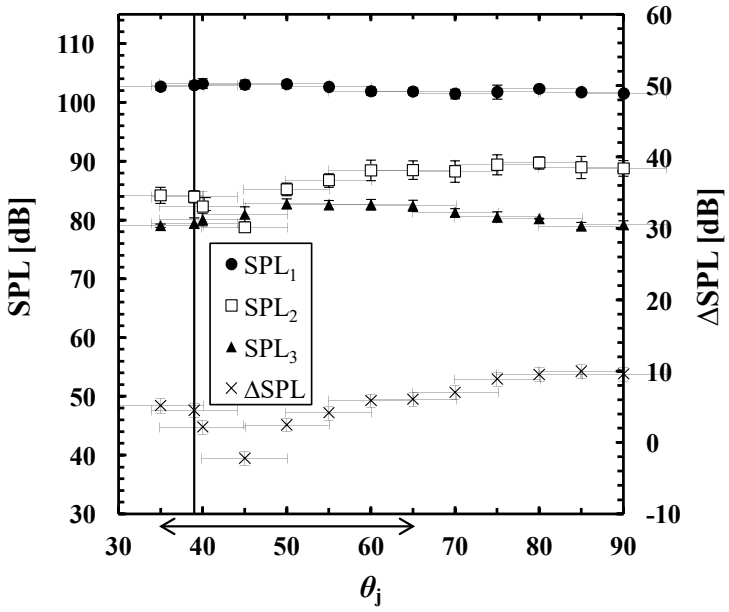

Figure 4.17 Variations of harmonic structure with the jet angle. Line and arrow show the actual blowing condition and the practical range, respectively. All parameters other than the one being varied were fixed to the actual blowing condition shown in Table 4.1 ($y_j / h = 0.24, l / h = 5.6, Q = 16$ L/min). Error bar is shown for each measured value.

Table 4.5 lists the variation of ΔSPL with the parameters in their practical ranges. The jet offset has the greatest effect on the harmonic structure; however, the effects of the jet angle is almost the same as that of the flow rate and larger than that of the exit-edge distance. The effect of the jet angle on timbre seems to be an important consideration for flute players.

Table 4.5 Variation of ΔSPL with parameters in practical range

Parameter	Variation range of ΔSPL in practical range [dB]		
	Min.	Max.	Diff.
Jet angle θ_j	−2.2	6.1	8.3
Exit-edge distance l / h	2.6	6.7	4.0
Jet offset $y_{j,e} / h$	−0.8	28.3	29.1
Flow rate Q	−5.5	3.9	9.4

In Fig. 4.17, the blowing parameters other than the jet angle were fixed to the actual blowing condition measured for one player. To confirm generality of the effects of the jet angle on harmonic structure, Fig. 4.18 shows the variations of the harmonic structure with the jet angle measured by fixing the jet offset to several values in the practical range: $y_{j,e} / h = 0.0, 0.17, 0.24, 1.0$. The jet angle that ΔSPL exhibits its minimum is $\theta_{j,min} = 39°$ for $y_{j,e} / h = 0.0$ and 0.17, $\theta_{j,min} = 45°$ for $y_{j,e} / h = 0.24$. As $y_{j,e} / h$ increases (decreases), the curve of ΔSPL seems to shift toward a larger (smaller) jet angle, and $\theta_{j,min}$ increases (decreases). For $y_{j,e} / h = 1.0$, ΔSPL decreases with increasing the jet angle. Assuming that the curve shifts toward a larger jet angle with increasing $y_{j,e} / h$, at $y_{j,e} / h = 1.0$, $\theta_{j,min}$ possibly exceeds the experimental range; therefore, $\theta_{j,min}$ does not exist at $y_{j,e} / h = 1.0$. The differences of the maximum and the minimum ΔSPL in the practical range are about 12, 8, and 17 dB for $y_{j,e} / h = 0.0, 0.17,$ and 1.0, respectively. ΔSPL varies with the jet angle in the range of not exceeding the variation of ΔSPL with the jet offset (about 30 dB).

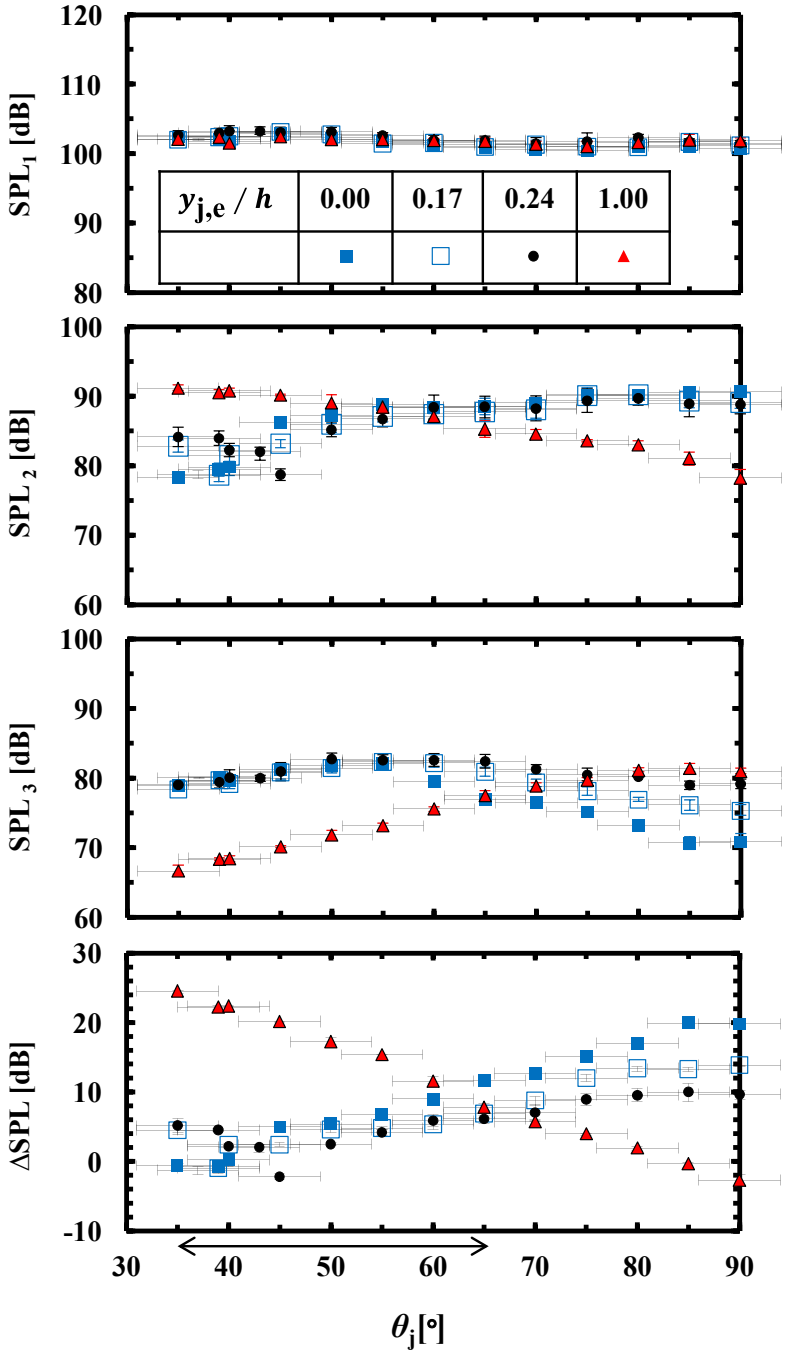

Figure 4.18 Variations of harmonic structure with jet angle, where the exit-edge distance and the flow rate were fixed to the actual blowing condition shown in Table 4.1 ($l / h = 5.6,\ Q = 16$ L/min). Arrow shows the practical range. Error bar is shown for each measured value.

4.5.2. Mechanism Whereby Jet Angle Affects Harmonic Structure

The blowing parameters are defined based on the reference jet direction measured without the flute head joint. However, the jet direction can be changed in the presence of the acoustic field as observed in the flow visualizations for flute-like instruments [24, 68, 25, 26]. Due to the change in the direction, the actual jet offset can be different from the jet offset $y_{j,e}$. This section estimates the change in the actual jet offset with the jet angle to show the mechanism whereby the jet angle affects the harmonic structure.

Figure 4.19 plots the variation of the SPLs of the harmonics with the jet offset. For $\theta_j = 39°, 50°,$ and $65°$, the jet offsets minimizing ΔSPL, $y_{j,e,min} / h$, were about 0.0, 0.5, and 0.7, respectively. As the jet angle increases, $y_{j,e,min} / h$ becomes large, implying that the curves of SPL_2 and SPL_3 shift toward the positive direction of $y_{j,e} / h$.

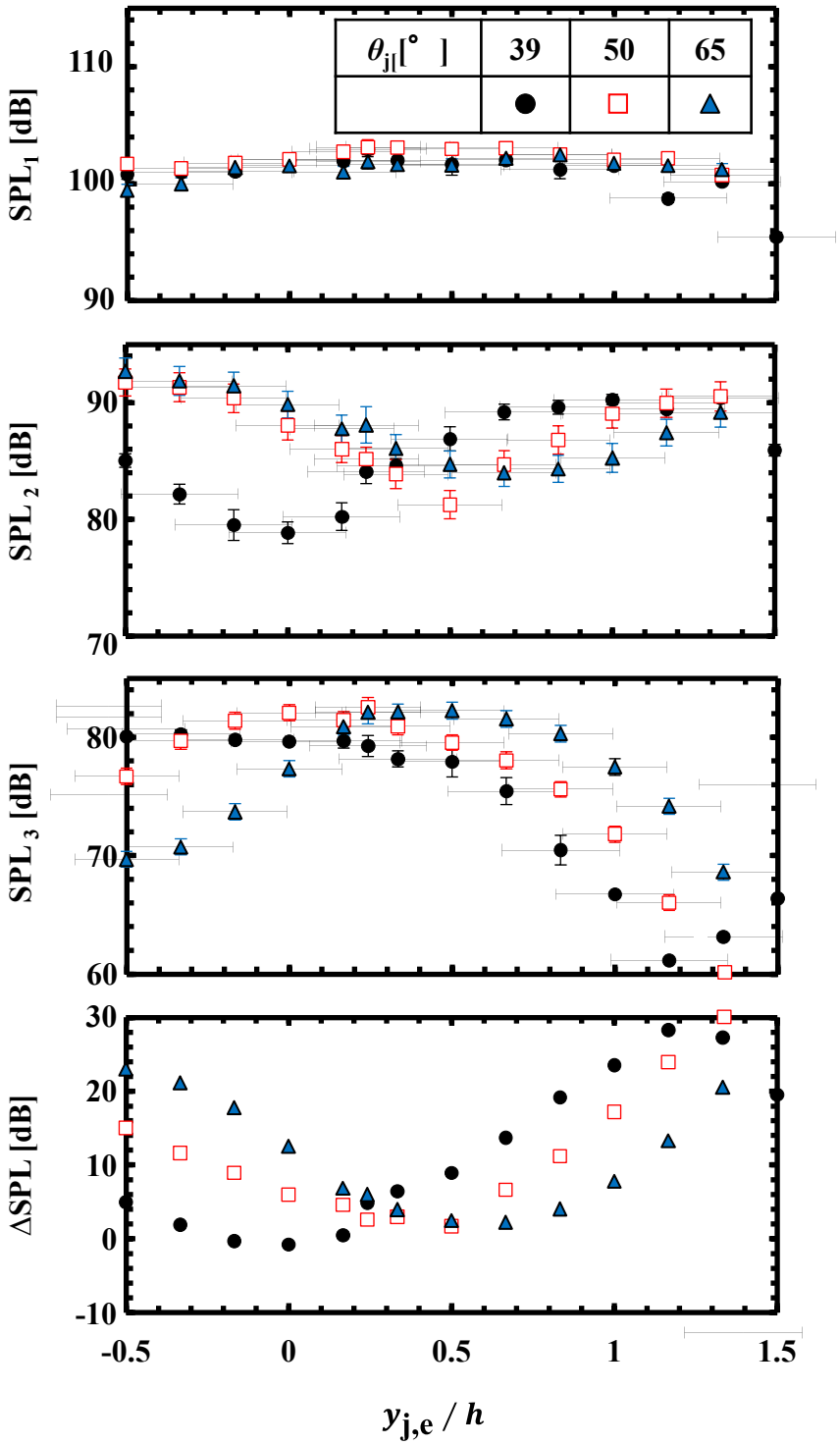

Figure 4.19 Variations of harmonic structure with jet offset, where the exit-edge distance and the flow rate were fixed to the actual blowing condition shown in Table 4.1 ($l / h = 5.6,\ Q = 16$ L/min). Error bar is shown for each measured value.

Figure 4.20 shows the spatial distribution of the jet fluctuation center ($\bar{\eta}$) in the flow field for $\theta_j = 39°,\ 50°$, and $65°$, where the horizontal axis is shown from the cavity exit ($x_j = 0$) to the edge ($x_j = l = 5.6h$). In these measurements, the jet offset was set to zero ($y_{j,e} / h = 0$), *i.e.*, the reference jet direction without the head joint was directed to the edge. The jet fluctuation center inclines outward ($\bar{\eta} > 0$) or inward ($\bar{\eta} < 0$) almost linearly toward downstream. The jet fluctuation center at the exit is estimated to be about $\bar{\eta}(0) = -0.3$ for all the jet angles by linear approximation between $x_j / h = 0$ to 2.0. During the jet traveling toward the edge, the jet fluctuation center inclines outward at $\theta_j = 39°$, while it inclines inward at $\theta_j = 50°$ and $65°$. Assuming that the jet travels with the same inclination of $\bar{\eta}$, the actual jet offsets to the edge, $y_{a,e}$, for $\theta_j = 39°,\ 50°$, and $65°$ were respectively estimated to be $y_{a,e} / h = 0.08, -0.42$, and -0.64 by linear approximation between $x_j / h = 2.0$ and l / h. As the jet angle increases, the jet fluctuation center inclines inward, resulting in the decrease in the actual jet offset. The absolute values of the actual jet offset, $|y_{a,e} / h|$, almost corresponded to $y_{j,e,min} / h$ of 0.0, 0.5, and 0.7 in Fig. 4.19. As the jet angle increases, the jet offset minimizing the ΔSPL ($y_{j,e,min} / h$) shifts outward ($y_{j,e,min} > 0$) by the same amount that the actual jet offset in the flow field shifts inward ($y_{a,e} < 0$) probably due to the decrease in the actual jet offset. This means that, to produce a harmonic structure similar to that radiated at a small jet angle, the jet offset must be increased to cancel out the decrease of the actual jet offset.

The changes of the harmonic structure with the jet angle in Fig. 4.18 also seems to be caused by the decrease in the actual jet offset. Figure 4.18 shows that, when the jet offset increases from $y_{j,e} / h = 0.17$ to 0.24, the curve of ΔSPL shifts toward a larger jet angle by about $\Delta\theta_{j,min} = 6°$. Under the condition of Fig. 4.18, the actual jet offset is estimated to decrease by about 0.07 when the jet angle increases by $6°$.

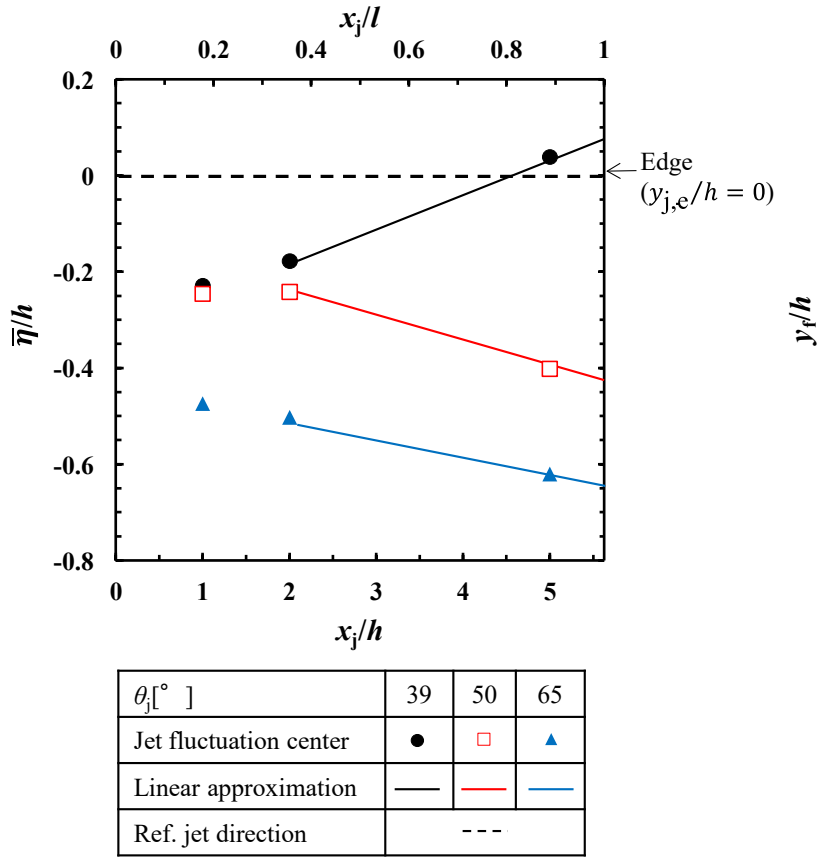

Figure 4.20 Spatial distributions of jet fluctuation center ($\overline{\eta}$) and the reference jet direction in the x_i–y_i coordinate system. ($y_{j,e} = 0$, $l / h = 5.6$, $Q = 16$ L/min)

To investigate the cause of the inward inclination of $\overline{\eta}$, Fig. 4.21 shows the periodical variations of the relative jet displacement near the edge ($x_j / h = 5$). This displacement is the relative displacement from the jet fluctuation center and nondimensionalized with the amplitude, $\xi = (\eta - \overline{\eta}) / \eta_{amp}$. This representation is to compare the speed of the change of the jet direction, independent of the jet amplitude. Table 4.6 shows the absolute value of the acceleration of ξ, $|d^2\xi / dt^2|$, at the moment when ξ becomes the maximum and the minimum. This acceleration is obtained by approximating ξ by a quadratic function in the range that ξ changes $\pm 1h$ from its maximum or minimum. The acceleration almost decreases as the jet angle increases. The difference in the acceleration between the jet angles is larger when ξ becomes its minimum than when ξ

becomes its maximum. As can be seen from the curve shapes of ξ, the change of the jet direction from inward to outward becomes slower as the jet angle increases. Therefore, as shown in Fig. 4.11(b), the time period that the jet displacement is lower than the edge height ($\eta < 0$) becomes longer as the jet angle increases. As a result, the jet fluctuation center becomes more inward as the jet angle increases. The cause of the deceleration is to be discussed in Sec. 5.5.2 in terms of the geometrical relationship between the jet and the edge.

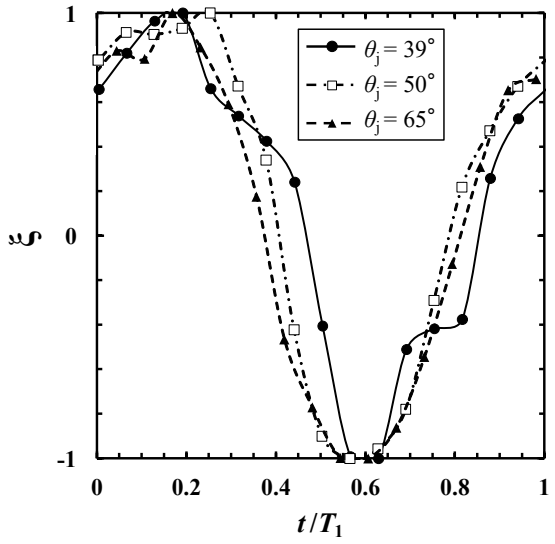

Figure 4.21 Periodical variations of the relative jet displacement from the jet fluctuation center nondimensionalized with the amplitude, $\xi = \left(\eta - \overline{\eta}\right) \ / \ \eta_{\mathrm{amp}}$, at $x_{\mathrm{j}} / h = 5$. ($y_{\mathrm{j,e}} = 0,\ l / h = 5.6,\ Q = 16$ L/min)

Table 4.6 Absolute value of the acceleration of the jet fluctuation, $|\mathrm{d}^2\xi / \mathrm{d}t^2|$, at the moment when ξ becomes the maximum ant the minimum

Jet angle θ_{j} [º]	At maximum ξ	At minimum ξ
39	24	138
50	15	54
65	15	42

The other factor that could relate to the SPLs of the harmonics is the amplitude of each mode of jet oscillations. As the jet amplitude of a certain mode near the edge increases, the volume flow entering the resonator at this mode increases; thus, the SPL of this acoustic mode increases. Figure 4.22 shows the relation between the relative jet amplitude of the second to the third mode, $|\eta_{\mathrm{amp},2}| / |\eta_{\mathrm{amp},3}|$, near the edge ($x_\mathrm{j} / h = 5$) and ΔSPL. The relative jet amplitude shows little correlation with ΔSPL. Therefore, the variation of ΔSPL with the jet angle is mainly caused by the decrease in the actual jet offset due to the inclination of the jet fluctuation center.

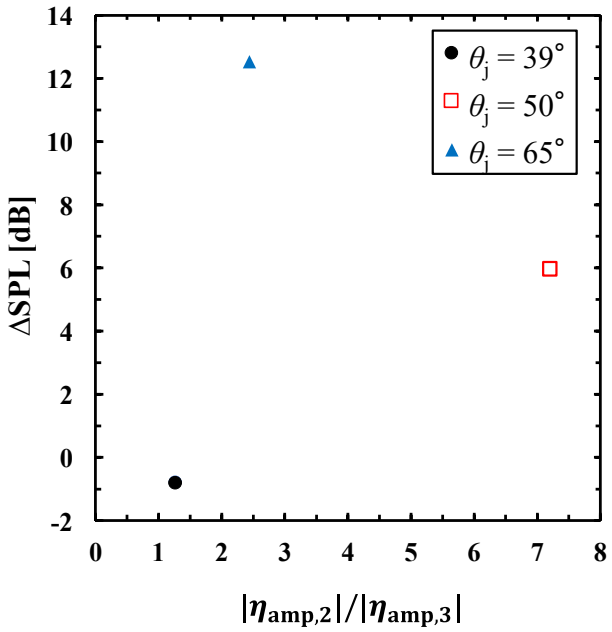

Figure 4.22 Relation between relative jet amplitude of second to third mode at $x_\mathrm{j} / h = 5$ and differential SPL of second to third harmonic. ($y_\mathrm{j,e} = 0$, $l / h = 5.6$, $Q = 16$ L/min)

The changes of ΔSPL with the jet angle is mainly due to the change of SPL_2 rather than SPL_3, as shown in Sec. 4.5.1. The condition under which SPL_3 hardly changes is also investigated. Figure 4.14 shows that SPL_3 remains almost constant for $y_\mathrm{j,e} / h < 0$. In Fig. 4.14, the jet angle was fixed to $\theta_\mathrm{j} = 39°$. At this jet angle, the actual jet offset

seems almost coincidence with the jet offset, where $y_{a,e} / h = 0.08$ under $y_{j,e} = 0$ (see Fig. 4.20). SPL_3 seems to remain almost constant for $y_{a,e} / h < 0$. This tendency of SPL_3 with the actual jet offset is also observed in Figs. 4.17 and 4.18. These figures show that, under the condition of $y_{j,e} / h = 0.24$, the jet angle that ΔSPL exhibits its minimum is $\theta_{j,min} = 45°$ and SPL_3 remains almost constant in $\theta_j > 45°$. From the discussions so far, the actual jet offset is expected to be zero around $\theta_j = 45°$, and the actual jet offset can be $y_{a,e} / h < 0$ in $\theta_j > 45°$ due to the inward inclination of the jet fluctuation center. Therefore, SPL_3 remains almost constant in $\theta_j > 45°$. These results confirm the tendency where SPL_3 remain almost constant for $y_{a,e} / h < 0$; however, it is not clear from this study whether only SPL_3 of the radiated sound is constant or SPL_3 of the internal sound source is also constant. Further investigations are required to clarify this mechanism.

4.5.3. Results of Measurements for a Flute Whole Body

The variations of harmonic structure with the jet angle were also measured for a flute with a body and a foot joint. The measurements were performed with the fingering of A4 (see Fig. 4.23). The exit-edge distance was fixed to the value shown in Table 4.1 ($l / h = 5.6$), which is within the possible ranges for A4 shown in Refs. [20, 38, 54]. The flow rate was fixed to $Q = 10$ L/min ($U_0 = 13.4$ m/s), where the fundamental frequency of radiated sounds was almost 440 Hz. Figure 4.24 shows the variations of the SPLs measured by fixing the jet offsets to the values in Fig. 4.18 ($y_{j,e} / h = 0.0, 0.17, 0.24, 1.0$). The jet angles that ΔSPL exhibits its minimum are respectively $\theta_{j,min} = 37°$ and $43°$ for $y_{j,e} / h = 0.17$ and 0.24, which are almost the same as in Fig. 4.18 measured for the head joint. In both the measurements for the A4 fingering and the head joint, the curve of ΔSPL shifts toward a larger jet angle by about $\Delta\theta_{j,min} = 6°$ for the increase of the jet offset by $\Delta y_{j,e} / h = 0.07$. From this result, for both the A4 fingering and the head joint, the actual jet offset probably changes by $\Delta y_{a,e} / h = -0.07$ when the jet angle changes by $\Delta\theta_j = 6°$.

The variations of harmonic structure with the jet angle were also investigated for the

fingerings of A4, A5 (880 Hz), and A6 (1760 Hz), as shown in Fig. 4.25. The exit-edge distance and the jet offset were fixed to the values shown in Table 4.1 ($l / h = 5.6$, $y_{j,e} / h = 0.24$), which are almost within the possible ranges for A4, A5, and A6 shown in Refs. [20, 38, 54]. The flow rate was fixed to $Q = 16$ L/min ($U_0 = 21.5$ m/s) for A5 and $Q = 32$ L/min ($U_0 = 43.0$ m/s) for A6. The radiated sounds were investigated within the range that the fundamental frequency is ± 10 cent of A4, A5, or A6. The jet angle that ΔSPL exhibits its minimum is around $\theta_j = 39°$ for all of A4, A5, and A6. There is no noticeable shift in the ΔSPL curve with the tone range. From these results, the variations of harmonic structure with the jet angle measured for the head joint can also occur over the flute's three ranges.

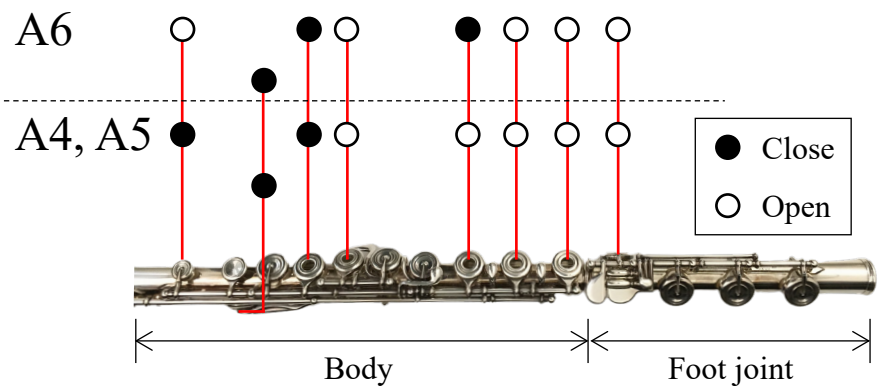

Figure4.23 Fingerings of A4, A5, and A6.

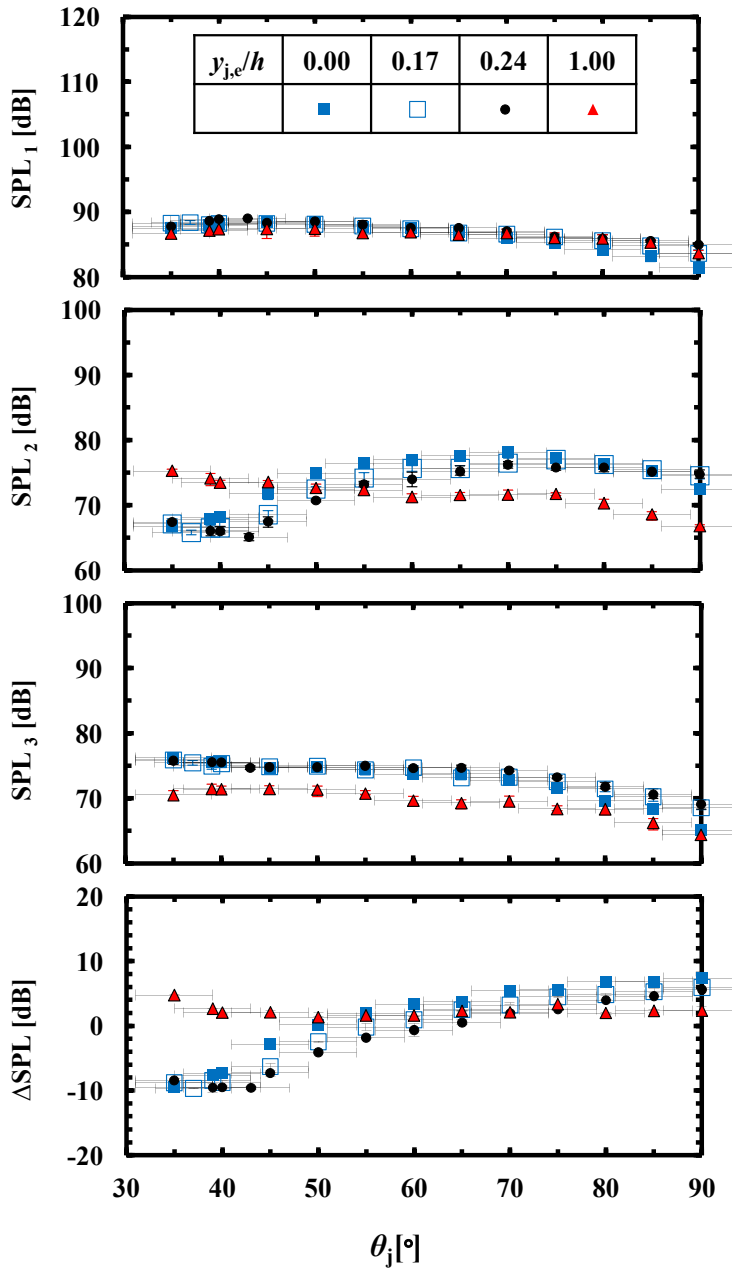

Figure 4.24 Variations of harmonic structure with jet angle measured for flute with A4 fingering. The exit-edge distance was fixed to the value shown in Table 4.1 (l / h = 5.6). Flow rate was fixed to Q = 10 L/min (U_0 = 13.4 m/s).

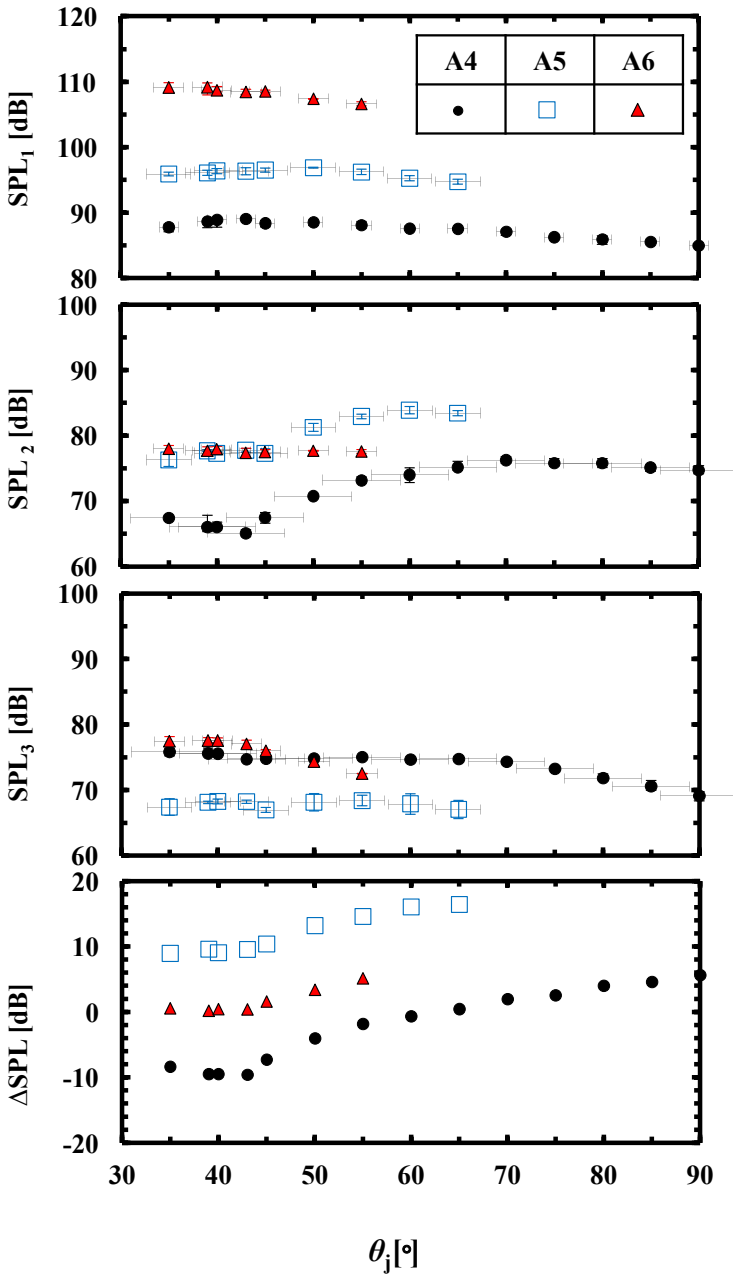

Figure 4.25 Variations of harmonic structure with jet angle measured for flute with A4, A5, and A6 fingering. The exit-edge distance and the jet offset were fixed to the values shown in Table 4.1 ($l / h = 5.6$, $y_{j,e} / h = 0.24$). The flow rate was fixed to $Q =$ 10 L/min ($U_0 = 13.4$ m/s) for A4, $Q = 16$ L/min ($U_0 = 21.5$ m/s) for A5, and $Q =$ 32 L/min ($U_0 = 43.0$ m/s) for A6.

4.6. Conclusion

This chapter showed the effects of the blowing parameters on the harmonic structure. The radiated sound showed that, within the practical ranges of the parameters, the harmonic structure varies markedly with the jet offset (ΔSPL $\approx$ 30 dB). Compared to the jet offset, the change of the harmonic structure with the jet angle was less (ΔSPL $\approx$ 10 dB); however, this change was almost equal with the change with the flow rate and comparably larger than that with the distance (ΔSPL $\approx$ 5 dB). The effect of the jet angle on timbre seems to be an important consideration for flute players.

The mechanism whereby the harmonic structure changes with the jet angle was investigated based on both the measured acoustic and flow field. Periodical jet fluctuations in the flow field were determined by phase-averaging the measured values obtained with a hot-wire anemometer. The spatial distribution of the jet fluctuation centers (time-averaged jet displacements) showed that, with increasing the jet angle, the jet fluctuation center inclines inward. This inclination seems to be caused by the deceleration of the jet fluctuation when the jet changes its direction from inward to outward. As the jet angle increases, this fluctuation was found to decelerate more. Due to this deceleration, the time period that the jet displacement is lower than the edge height becomes longer; as a result, the jet fluctuation center becomes inward, and the actual jet offset decreases. The radiated sound showed that, when increasing the jet angle, the curve of ΔSPL with the jet offset shifted toward a larger jet offset. This shift was almost the same amount as the decrease of the actual jet offset in the flow field. This indicates that, to produce a harmonic structure similar to that radiated at a small jet angle, the jet offset needs to be increased (the jet needs to be directed to the outside the edge) to cancel out the decrease of the actual jet offset. The amplitude of each mode of jet oscillation showed little correlation to the variation of the harmonic structure with the jet angle. The variations of the harmonic structure with the jet angle is mainly caused by the change of the actual jet offset due to the inclination of the jet fluctuation center.

In actual performances, when a player changes the air-stream direction, other

conditions, like lip shapes and the jet offset, are possibly changed [38]. For experimental results to be applicable to actual performances, it is necessary to investigate whether harmonic structure can be controlled more effectively by adjusting the jet angle or other conditions.

5. Effects of Geometrical Relation Between Jet Direction and Edge on Jet Fluctuations and Sound

5.1. Introduction

The effects of the geometrical relationship between the jet direction and the edge on the jet fluctuations and the sound were investigated. This relationship changes depending on the jet offset and the jet angle. Figure 5.1 illustrates the jet direction when the jet offset and the jet angle are changed, assuming that the jet fluctuates inward and outward at the same angle around the jet fluctuation center. The angle between the instantaneous jet direction and the wall of edge does not change with the jet offset but changes with the jet angle. The distance from the jet exit and the position where the jet impinges on the wall changes with both the jet offset and the jet angle. Due to these changes, the effects of wall on the jet fluctuations can change. To visualize and compare the jet fluctuations, this study performs direct aeroacoustic simulations on the flute under the conditions of two jet offsets (the relative height of the jet to the edge). Then, the discussion on the changes of jet fluctuations with the jet offset is applied to the discussion on the changes with the jet angle observed in Chap. 4.

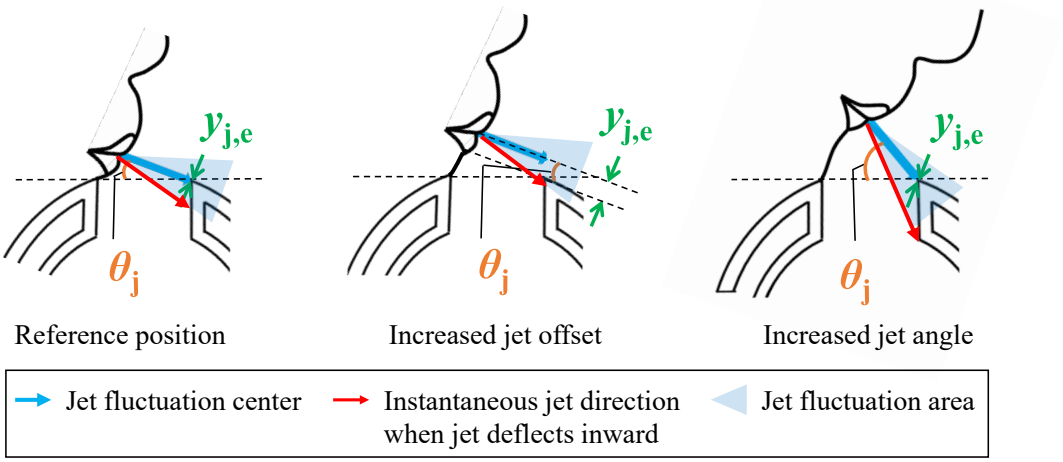

Figure 5.1 Schematic of instantaneous jet direction when the jet offset and the jet angle are changed, assuming that the jet fluctuates inward and outward at the same angle in the jet fluctuation area around the jet fluctuation center.

5.2. Chapter Layout

The blowing conditions and the computational methods are shown in Sec. 5.3. The computational results are validated with experimental results in this section. The changes of the radiated sound and the jet fluctuations with the jet offset and their relevancy are shown in Sec. 5.4. The cause of the changes of the jet fluctuations is discussed from the instantaneous jet direction in Sec. 5.5. This discussion is also applied for the discussion on the cause of the inward inclination of the jet fluctuation center with the jet angle observed in Chap. 4.

5.3. Blowing Conditions and Computational Methodologies

5.3.1. Blowing Conditions

The computations were performed under the conditions of the jet offset (relative height of the jet from the edge) $y_{j,e}/h = 0$ and 0.37. The definitions of blowing condition were the same as in Chap. 4. The other blowing parameters than the jet offset were fixed to the values of the actual blowing condition in Table 4.1 (see Table 5.1).

Table 5.1 Blowing condition for computation

Blowing condition	Value
Jet angle θ_j [º]	39
Exit-edge distance l / h	5.6
Jet offset $y_{j,e} / h$	0, 0.37
Flow rate Q [L/min]	16.0
Cross-sectional mean jet velocity at cavity exit U_0 [m/s]	21.5

5.3.2. Computational Methodologies

The governing equations, the computational scheme, and boundary conditions were the same with those in Chap. 3. The shapes of the flute head joint and around the cavity exit were reproduced from the actual ones used in the experiments in Chap. 4. The angle between the inner and the outer wall of the edge is about 40°. Figure 5.2(a) shows the whole view of the computational domain. The minimum grid spacing is 0.05 mm around the cavity exit center, and the number of grid points is about 1.5×10^8. Figure 5.2(b) shows the cross section of the cavity exit center ($z_j = z_f = 0$). The shape of the cavity was modified by cutting at about 30 mm from the exit to reduce computational resources. A duct was connected on the cut surface, and velocity was given uniformly. In the computation, the relative position of the oral cavity from the flute was adjusted so that both the blowout center and the direction of the jet are almost correspond to those in the experiments under the reference condition in Table 5.2. The relative position of the oral cavity from the flute is shown in Table 5.3. This table is shown in the x_f–y_f coordinate system (see Fig. 5.2 (b)) whose origin is the edge and x_f-direction is the direction from the edge to outside the flute along the horizontal line of mouth opening. At this blowing condition, the angle between the reference jet direction and the inner wall of the flute (θ_{iw}) is 140°, and the angle between the reference jet direction and the outer wall (θ_{ow}) is 181°. This position of the oral cavity and the flute is defined as the equivalent position

to Table 5.2 in the computation. With reference to this position, the jet offset was varied.

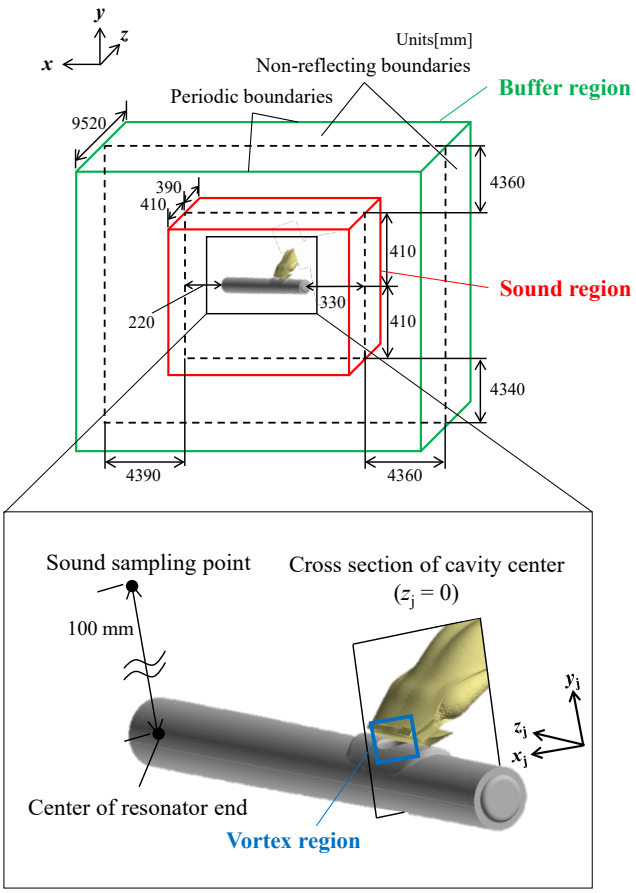

(a) Whole view

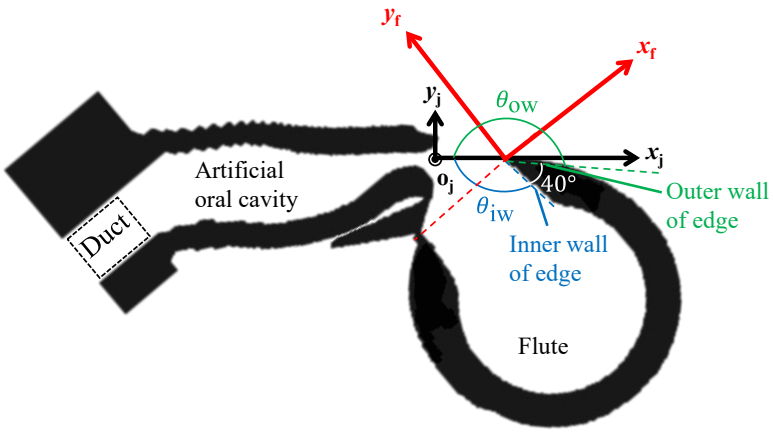

(b) Cross section of cavity center ($z_j = z_f = 0$)

Figure 5.2 Geometry of computational model.

Table 5.2 Reference blowing condition for experiment

Blowing condition	Value
Jet angle θ_j [°]	39
Lip to edge distance l / h	5.6
Jet offset $y_{j,e} / h$	0
Flow rate Q [L/min]	16.0
Cross-sectional mean jet velocity at cavity exit U_0 [m/s]	21.5

Table 5.3 Geometrical condition equivalent to Table 5.2

Geometrical condition		Comp. case 1	Exp.
Cavity exit center ($z_f = 0$)	x_f	−5.57	−5.25
	y_f	3.94	4.25
Angle between normal direction of reference line of cavity exit and horizontal line of mouth opening ($\theta_j + \theta_i$) [°]		46	53

5.3.3. Validation of Computational Methods

5.3.3.A. Comparison with Experimental Results

The radiated sound and the flow field predicted by the computation were validated with those measured by the experiments in Chap. 4 under the condition in Table 5.2.

Figure 5.3 shows the sound pressure spectra of the radiated sound. The predicted frequency and SPL of the fundamental tone by the computation are almost the same as those in the experiments. The acoustic radiation of the fundamental tone is nearly reproduced by the computation. The peaks of the second and the third harmonic appear at the frequencies twice and three times the fundamental frequency. The differential sound pressure level of the second to the third harmonic (ΔSPL) was 4.0 and 1.6 dB in the computation and the experiments, respectively. The harmonic structure of the radiated

sound, in which the second harmonic is more predominant than the third harmonic, is nearly reproduced by the computation.

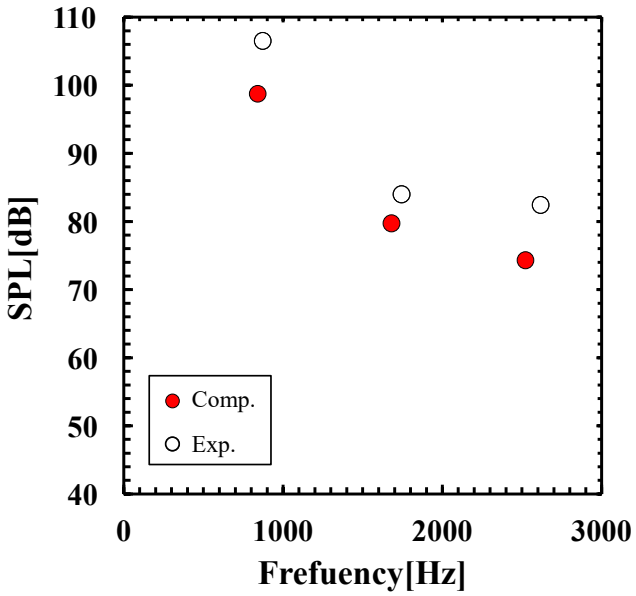

Figure 5.3 Sound pressure spectra of radiated sound. ($\theta_j = 39°, y_{j,e} = 0, l/h = 5.6, Q = 16$ L/min)

Figure 5.4 shows the periodical variations of velocity profiles in the flow field at $x_j/h = 1$ and 5. The velocity profiles at $x_j/h = 1$ are top-hat-shapes both in the computation and the experiments. The lines in the figure show the jet displacement (η), where η is defined as the distance from $y_{j,e} = 0$ to the center of the half-value positions of the maximum velocity, same as in Chap. 4. In the experiments, η at $x_j/h = 5$ are determined because the profiles are smooth due to the phase average (see Sec.4.4.2.B). In the computation, η at $x_j/h = 5$ is not determined for all of profiles because the velocity profile is divided into multiple peaks as observed in $t/T_1 = 3/4$. Therefore, η of computational results are shown from $x_j/h = 0$ to 4.

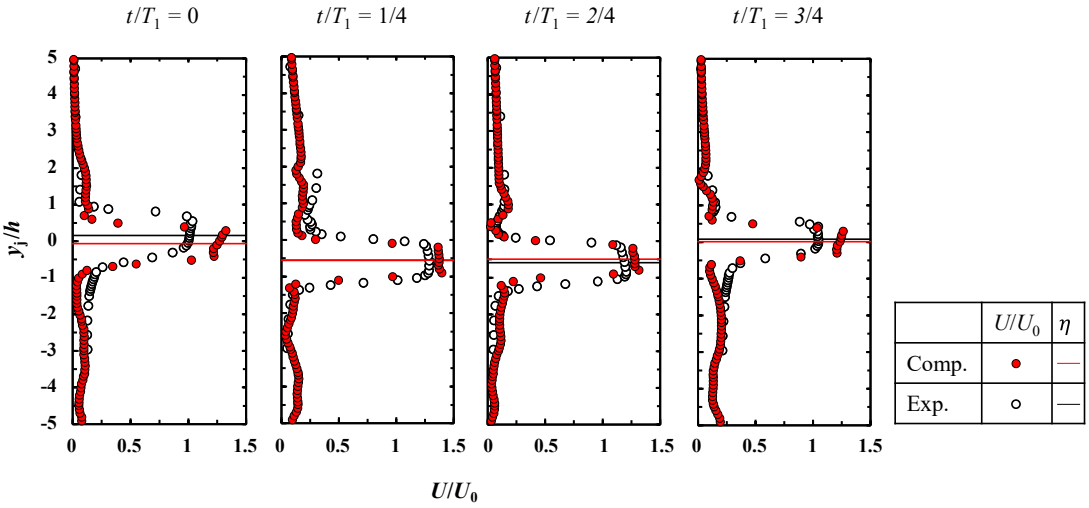

(a) $x_j / h = 1.0$

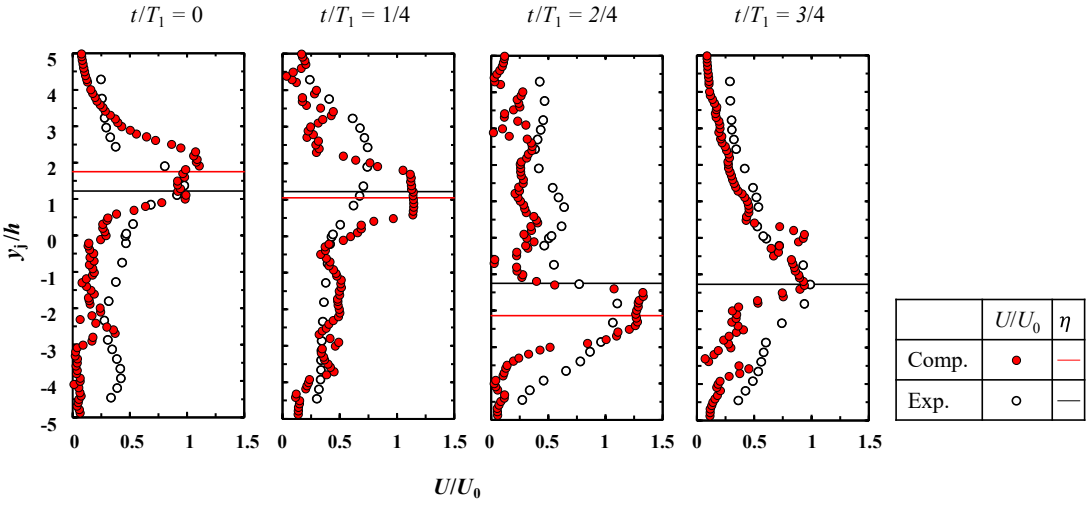

(b) $x_j / h = 5.0$

Figure 5.4 Periodical variations of velocity profiles. ($\theta_j = 39°, y_{j,e} = 0, l / h = 5.6, Q = 16$ L/min)

To investigate the actual jet offset, the spatial distributions of the jet fluctuation center $\overline{\eta}(x_j)$, which is the time average of $\eta(x_j, t)$, are obtained (see Fig. 5.5). The jet fluctuation center inclines outward in both the computation and the experiments. The time-averaged jet direction seems to be almost reproduced by the computation. By linearly

approximating $\bar{\eta}$, the values of actual jet offset (the relative height of the temporal mean position of jet fluctuation to the edge) were estimated to be $y_{a,e}/h = -0.1$ and 0.1 for the computation and the experiments, respectively. Since $|y_{a,e}|$ are almost the same in the computation and the experiments, the harmonic structures of the radiated sound are almost the same in the two. This denotes that the flow field predicted by the computation is consistent with the harmonic structure.

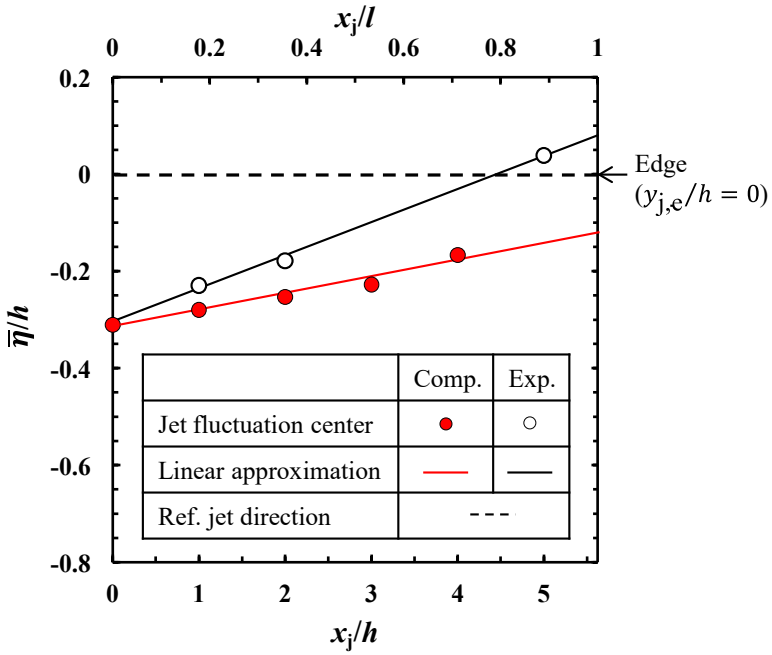

Figure 5.5 Spatial distributions of jet fluctuation center ($\bar{\eta}$), where lines show linear approximation of $\bar{\eta}$. ($\theta_j = 39°, y_{j,e} = 0, l/h = 5.6, Q = 16$ L/min)

5.3.3.B. Effects of Modification of Cavity Shape

The effects of the modification of cavity shape were verified in preliminary computations. Without the modification, the air flow passes through the bent of the throat (see Fig. 5.6); thus, the velocity on the upper jaw side is probably larger than the lower side. The preliminary computations were performed under the conditions that the velocity in the duct was given uniformly and non-uniformly. In the non-uniform condition, the

velocity for the upper and the lower side of the duct was given $14:9$ and the area of the upper and the lower side of a duct surface was $1:4$. The blowing condition for the preliminary computations is shown in Table 5.4.

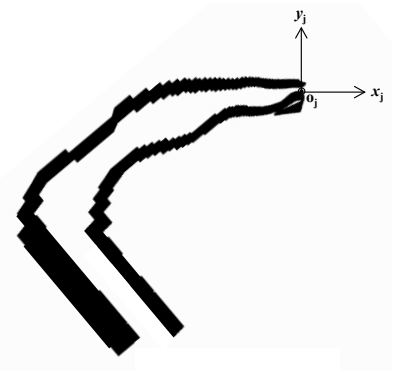

Figure 5.6 Artificial oral cavity without modification.

Table 5.4 Blowing condition for preliminary computation

Blowing condition	Value
Jet angle θ_j [º]	46
Lip to edge distance l / h	5.7
Jet offset $y_{j,e} / h$	-1.1
Flow rate Q [L/min]	16.0
Cross-sectional mean jet velocity at cavity exit U_0 [m/s]	21.5

Figure 5.7 shows the sound pressure spectra of the radiated sound. The frequencies and the SPLs of the fundamental tone, the second, and the third hormonic are almost the same under the uniform and the non-uniform condition. Figure 5.8 shows the spatial distributions of the jet fluctuation center ($\overline{\eta}(x_j)$). The jet fluctuation center inclines inward by almost the same inclination under the both conditions. From these results, the modification of cavity shape seems to affect little with the radiated sound and the time-averaged jet direction.

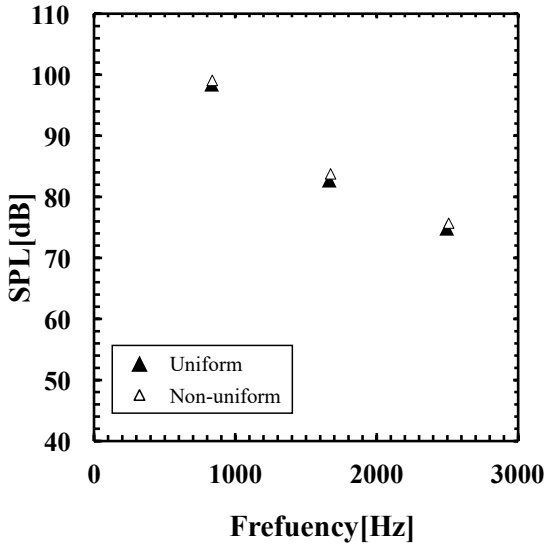

Figure 5.7 Sound pressure spectra of radiated sound under the conditions that the velocity in the duct was given uniformly and non-uniformly. ($\theta_{\mathrm{j}} = 46°, y_{\mathrm{j,e}} / h = -1.1, l / h = 5.7, Q = 16$ L/min)

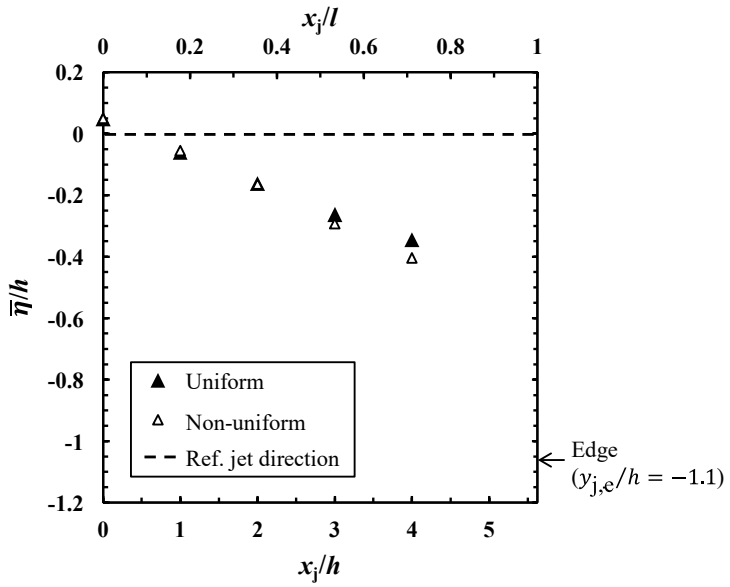

Figure 5.8 Spatial distributions of jet fluctuation center ($\overline{\eta}$) under the conditions that the velocity in the duct was given uniformly and non-uniformly. ($\theta_{\mathrm{j}} = 46°, y_{\mathrm{j,e}} / h = -1.1, l / h = 5.7, Q = 16$ L/min)

5.4. Results: Changes of Acoustic and Flow Field with Jet Offset

Figure 5.9 shows the sound pressure levels of the radiated sound under the jet offset $y_{j,e}/h = 0$ and 0.37. The fundamental frequency is about 840 Hz both in the two jet offsets. The SPLs of the fundamental frequency (SPL_1) and the second (SPL_2) and the third harmonic (SPL_3) are larger in $y_{j,e}/h = 0$ than those in $y_{j,e}/h = 0.37$. The ΔSPL ($\equiv SPL_2 - SPL_3$) is 5.4 and -0.4 dB for $y_{j,e}/h = 0$ and 0.37, respectively. The second harmonic is more predominant in $y_{j,e}/h = 0$ than in $y_{j,e}/h = 0.37$.

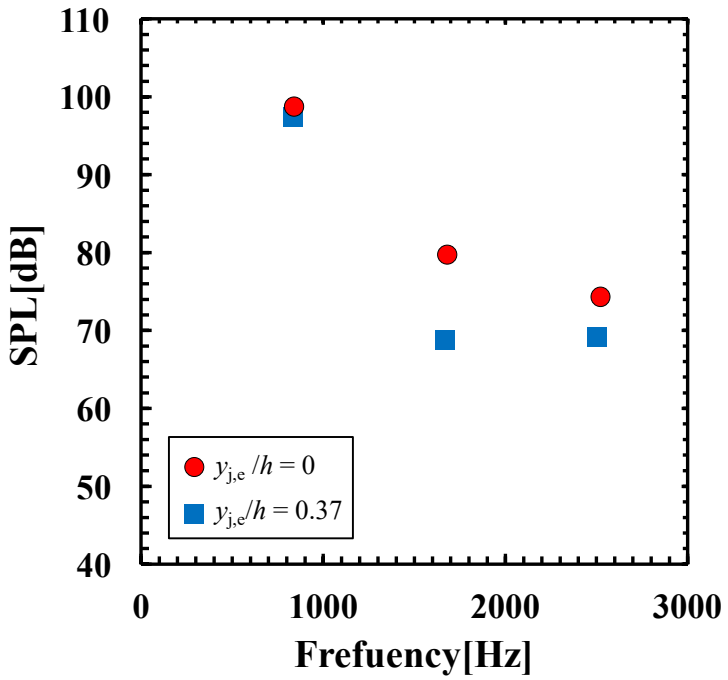

Figure 5.9 Sound pressure levels of radiated sound. ($\theta_j = 39°, l/h = 5.6, Q = 16$ L/min).

Figure 5.10(a) shows the spatial distributions of jet fluctuation center ($\bar{\eta}$) in the x_j-y_j coordinate system. In the upstream ($x_j/l < 0.5$), $\bar{\eta}$ inclines outward at almost the same inclination in both $y_{j,e}/h = 0$ and 0.37. In the downstream ($x_j/l > 0.5$), the inclination of $\bar{\eta}$ is almost the same as the inclination in the upstream in $y_{j,e}/h = 0$,

while the inclination of $\overline{\eta}$ changes inward in $y_{\mathrm{j,e}} / h = 0.37$. The actual jet offset (the relative height of $\overline{\eta}$ from the edge), $y_{a,\mathrm{e}}$, for $y_{\mathrm{j,e}} / h = 0$ and 0.37 were respectively estimated to be $y_{a,\mathrm{e}} / h = -0.07$ and 0.06 from the linear approximation of $\overline{\eta}$ between $x_{\mathrm{j}} / h = 3$ $(x_{\mathrm{j}} / l = 0.53)$ and $x_{\mathrm{j}} / h = 4$ $\left(x_{\mathrm{j}} / l = 0.71\right)$, where the jet fluctuation center is assumed to incline with the same inclination in the downstream. The absolute values of actual jet offset for the two jet offsets are almost zero. Figure 5.10(b) shows the spatial distributions of $\overline{\eta}$ in the x_{f}-y_{f} coordinate system, where the x_{f}- and the y_{f}- axes are at the same scale to show the inclinations of the jet and the edge. The directions of $\overline{\eta}$ of the two jet offsets get closer as they approach the edge. The conditions of $y_{\mathrm{j,e}} / h = 0$ and 0.37 are the conditions that the absolute values of actual jet offset are almost the same but the direction of jet to the edge is different. This indicates that the difference in the harmonic structure between the two jet offsets is not explained only by the actual jet offset.

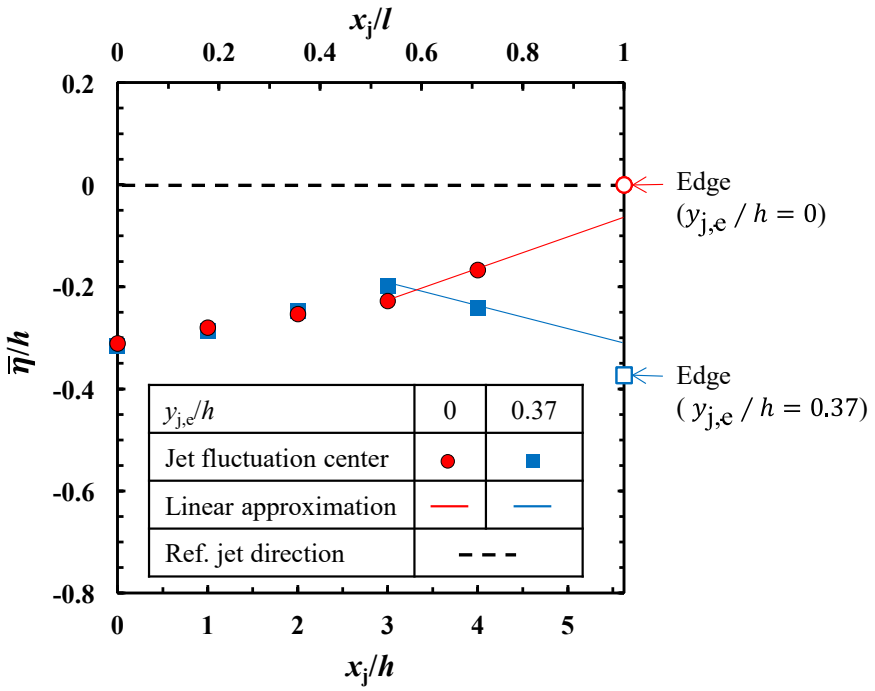

(a) x_j−y_j coordinate system

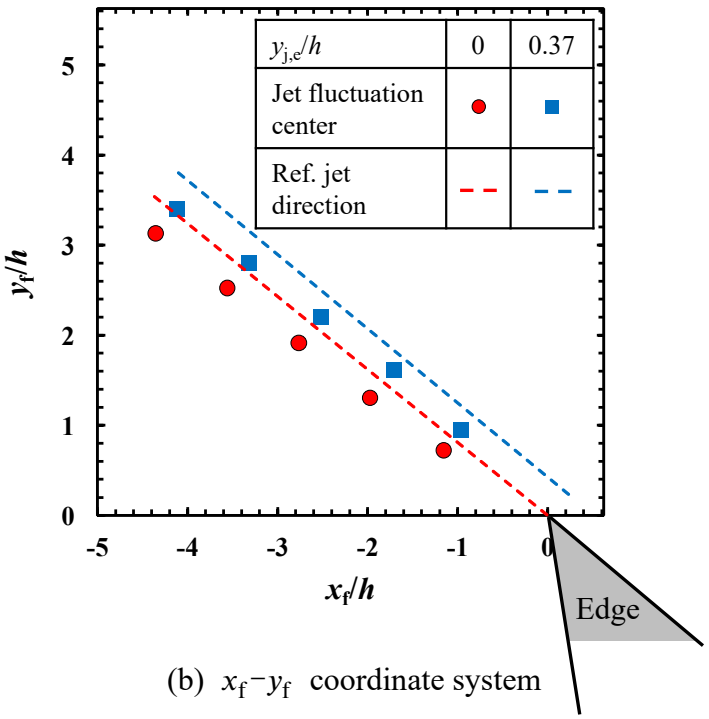

(b) x_f−y_f coordinate system

Figure 5.10 Spatial distributions of jet fluctuation center ($\bar{\eta}$) and the reference jet direction in the x_j-y_j coordinate system (a) and the x_f-y_f coordinate system (b). ($\theta_j = 39°, l/h = 5.6, Q = 16$ L/min).

The cause of the difference in the harmonic structure is investigated from the temporal jet fluctuations. Figure 5.11 shows the vorticity and the pressure during one cycle under $y_{j,e} / h = 0$ and 0.37. Under both the two jet offsets, the jet deflects outward the edge when the pressure becomes low ($t / T = 0$), while the jet deflects inward when the pressure becomes high ($t / T = 2 / 4$). This phase relationship between the jet and the pressure fluctuations is favorable for acoustic power generation in the volume-flow model [2, 8, 15, 60, 69, 71, 73]. Comparing the jet fluctuations between the jet offsets, the jet periodically leaves from the edge in $y_{j,e} / h = 0$, while the upper or the lower side of shear layer of jet almost always hits the edge in $y_{j,e} / h = 0.37$; the amplitude of $y_{j,e} / h = 0.37$ is smaller than that of $y_{j,e} / h = 0$. When the jet deflects outward ($t / T = 0$), in $y_{j,e} / h = 0.37$, the lower side of shear layer separates into two layers from around the center of mouth opening ($x_j / l = 0.5$). The upper side of shear layer and the upper side of the separated shear layer deflect outward. The lower side of the separated shear layer goes straight, implying that this flow is affected little by the fluctuation in the upstream. The separation of shear layer seems to be caused while the lower side of shear layer deflects outward (between $t / T = 3/4$ of the previous cycle and $t / T = 0$). Due to the separation, over one cycle, the lower side of the jet in the downstream is disturbed more in $y_{j,e} / h = 0.37$ than in $y_{j,e} / h = 0.37$.

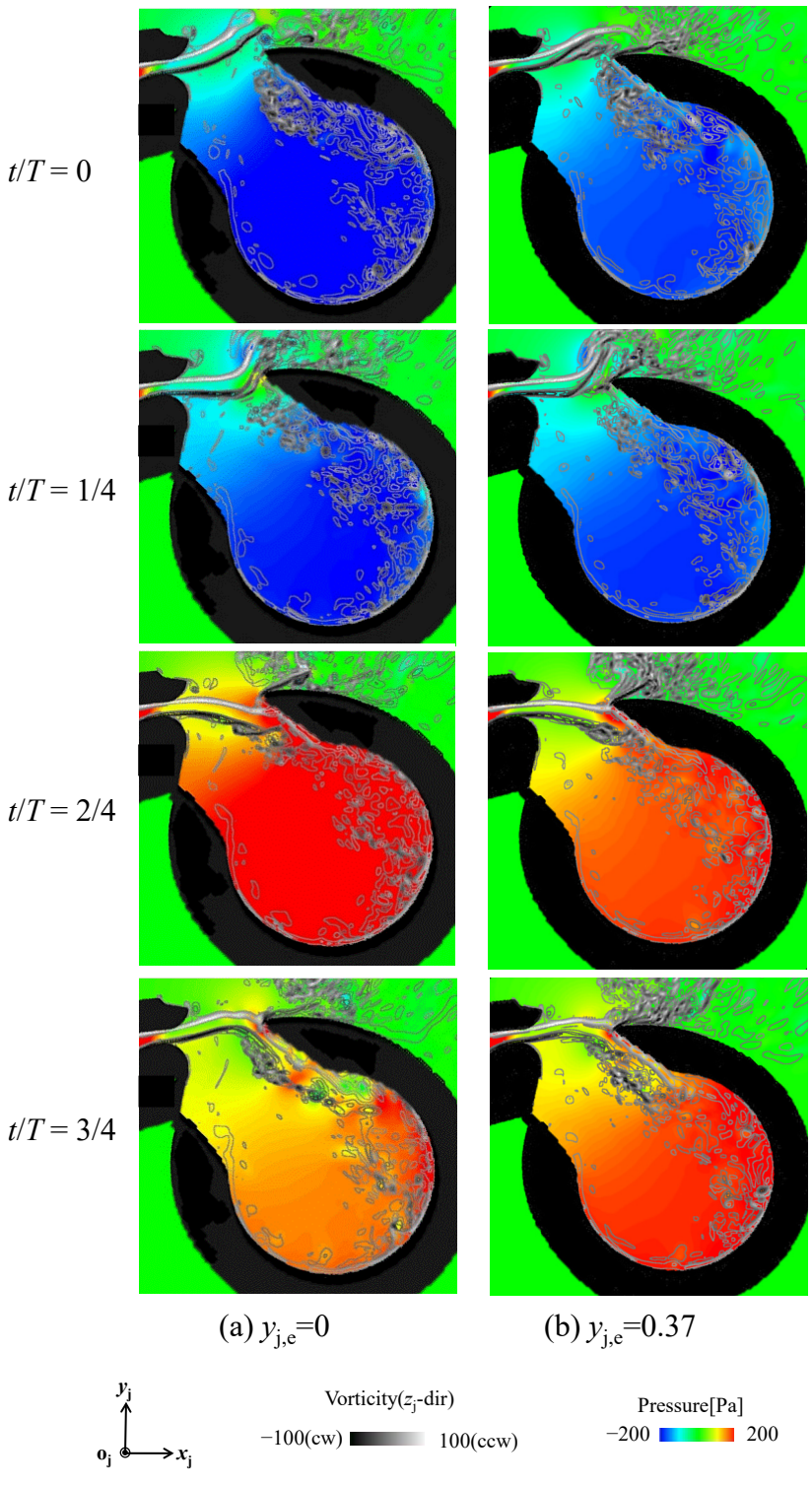

Figure 5.11 Temporal variation of flow field at $z_j = z_f = 0$ cross section, where vorticity and pressure are respectively shown by contour and color. ($\theta_j = 39°, l / h = 5.6, Q = 16$ L/min)

Figure 5.12 shows the amplitude of the first mode of jet fluctuations, $\eta_{\mathrm{amp},1} / h$, and the relative amplitude of the second and the third mode to the first mode, $\eta_{\mathrm{amp},2} / \eta_{\mathrm{amp},1}$ and $\eta_{\mathrm{amp},3} / \eta_{\mathrm{amp},1}$, from the exit to downstream. In the upstream ($x_{\mathrm{j}} / l < 0.5$), $\eta_{\mathrm{amp},1} / h$ of $y_{\mathrm{j,e}} / h = 0$ and 0.37 are almost the same. In the downstream ($0.5 < x_{\mathrm{j}} / l$), $\eta_{\mathrm{amp},1} / h$ of $y_{\mathrm{j,e}} / h = 0.37$ is smaller than that of $y_{\mathrm{j,e}} / h = 0$, where the amplification of the fluctuation is suppressed in $y_{\mathrm{j,e}} / h = 0.37$. Since the amplitude of the first mode is about 10 times larger than that of the higher modes, the entire jet amplitude is almost determined from $\eta_{\mathrm{amp},1} / h$. The jet amplitude in the visualization (Fig. 5.11) is larger in $y_{\mathrm{j,e}} / h = 0$ because $\eta_{\mathrm{amp},1} / h$ is larger. Also, $\eta_{\mathrm{amp},2} / \eta_{\mathrm{amp},1}$ and $\eta_{\mathrm{amp},3} / \eta_{\mathrm{amp},1}$ of $y_{\mathrm{j,e}} / h = 0$ are almost amplified toward the downstream, while those of $y_{\mathrm{j,e}} / h = 0.37$ are attenuated in the downstream. In the downstream of $y_{\mathrm{j,e}} / h = 0.37$, this lower side of the separated shear layer seems to be affected little by the fluctuation in the upstream (see Fig.5.11); therefore, the amplitude of entire jet, which includes the upper shear layer and the separated lower shear layers, becomes small, and the higher modes of fluctuations are suppressed. For the same reason, the jet fluctuation center in the downstream of $y_{\mathrm{j,e}} / h = 0.37$ gets closer to the edge height (see Fig. 5.10(a)).

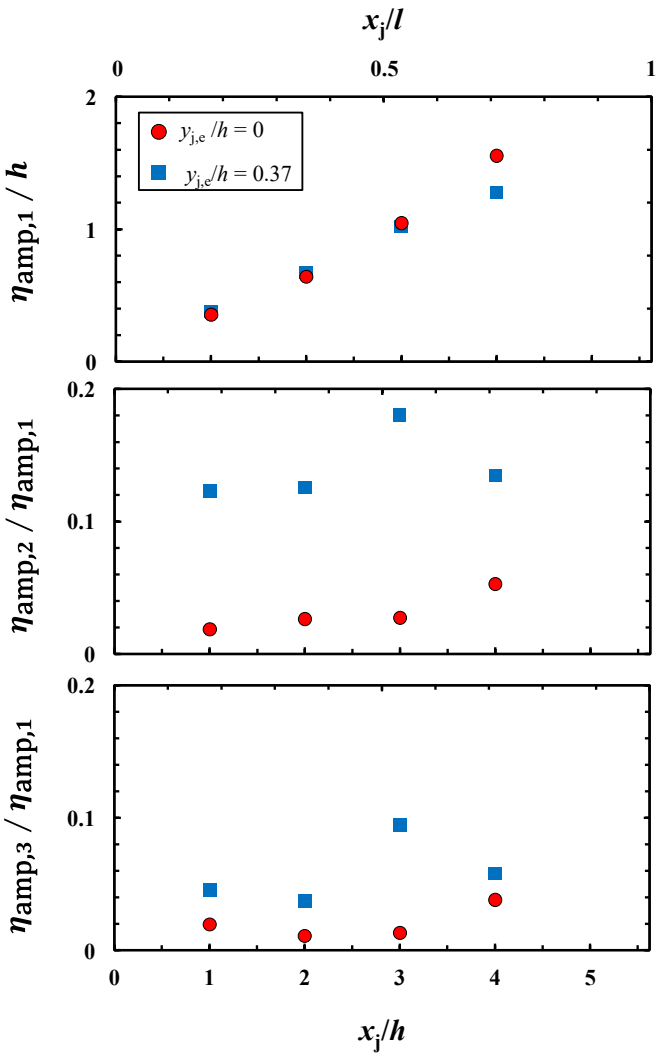

Figure 5.12 Amplitude of the first mode of jet fluctuations, $\eta_{amp,1} / h$, and the relative amplitude of the second and the third mode to the first mode, $\eta_{amp,2} / \eta_{amp,1}$ and $\eta_{amp,3} / \eta_{amp,1}$, from the exit to downstream. ($\theta_j = 39°, l / h = 5.6, Q = 16$ L/min).

As the result that these jet fluctuations reach the edge, the temporal fluctuations of the flow rate entering the resonator are as shown in Fig. 5.13(a). In this figure, the temporal variation of the flow rate is calculated by integrating the streamwise velocity (U) at the spanwise center of the edge ($x_j = l, z_j = 0$) in the y_j-direction:

$$S_{\mathrm{in}}(t) \equiv \int_{y_{\mathrm{j,lower}}}^{0} U(t)\mathrm{d}y_{\mathrm{j}}, \tag{5.1}$$

where $y_{\mathrm{j,lower}}$, is the lowest y_{j} where the time-averaged velocity ($\bar{U}$) is beyond 50% of the maximum $\bar{U}$. The value of S_{in} is nondimensionalized with the reference value, $S_0(\equiv U_0 h)$. Figure 5.13(a) shows that the amplitude of S_{in} of $y_{\mathrm{j,e}} / h = 0.37$ is smaller than that of $y_{\mathrm{j,e}} / h = 0$ because the jet amplitude is smaller. Since the amplitude of S_{in} is smaller, the SPLs of the radiated sound of $y_{\mathrm{j,e}} / h = 0.37$ is smaller. Figure 5.13(b) shows the Fourier transform of S_{in}, where the amplitude of S_{in} at the nth mode is nondimensionalized with the amplitude at the first mode, $S_{\mathrm{in},n} / S_1$. The relative amplitudes $S_{\mathrm{in},2} / S_1$ and $S_{\mathrm{in},3} / S_1$ of $y_{\mathrm{j,e}} / h = 0.37$ are smaller than those of $y_{\mathrm{j,e}}/h = 0$. This is because the amplitudes of the second and the third mode of jet fluctuations are attenuated in the downstream (see Fig. 5.12). Comparing $S_{\mathrm{in},2} / S_1$ and $S_{\mathrm{in},3} / S_1$, $S_{\mathrm{in},2} / S_1$ is larger than $S_{\mathrm{in},3} / S_1$ in $y_{\mathrm{j,e}} / h = 0$, while $S_{\mathrm{in},2} / S_1$ and $S_{\mathrm{in},3} / S_1$ are comparable in $y_{\mathrm{j,e}} / h = 0.37$. The predominancy of the second mode in $y_{\mathrm{j,e}} / h = 0$ is caused because S_{in} has the two peaks in Fig. 5.13(a): around when the jet deflects inward ($t / T_1 = 0.4$) and around when the jet changes its direction from inward to outward ($t / T_1 = 0.8$). Figure 5.14 shows the temporal fluctuation of the jet displacement (η) at $x_{\mathrm{j}} / h = 4$. Since the fluctuation of the jet displacement of $y_{\mathrm{j,e}} / h = 0$ does not have a second peak, the second peak of S_{in} is produced by the jet fluctuation around the edge not by the fluctuation upstream. The visualization in Fig. 5.11 showed that the lower side of the jet is disturbed little in $y_{\mathrm{j,e}} / h = 0$. Therefore, in $y_{\mathrm{j,e}} / h = 0$, the lower side of the jet impinges on the edge with a higher velocity than in $y_{\mathrm{j,e}} / h = 0.37$, and a reverse flow caused by the impingement may produce the temporal increase of the flow rate (S_{in}). The predominancy of the second to the third mode fluctuation of S_{in} is consistent with the harmonic structure of the radiated sound. This result denotes that the harmonic structure changes with the temporal fluctuations of jet, even though the actual jet offset does not change.

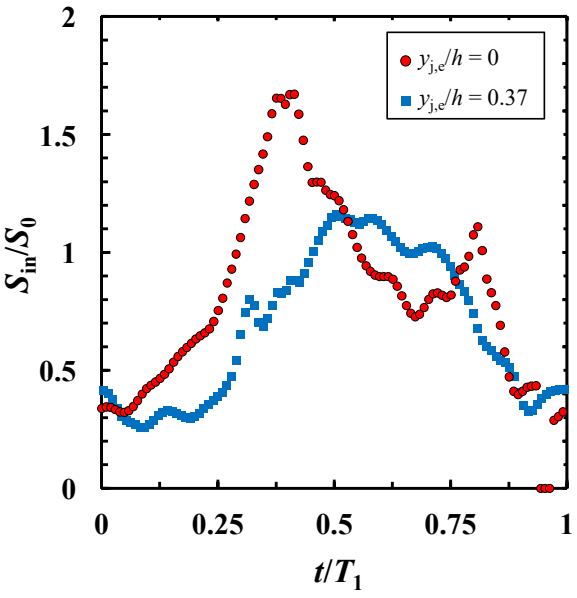

(a) Temporal variations

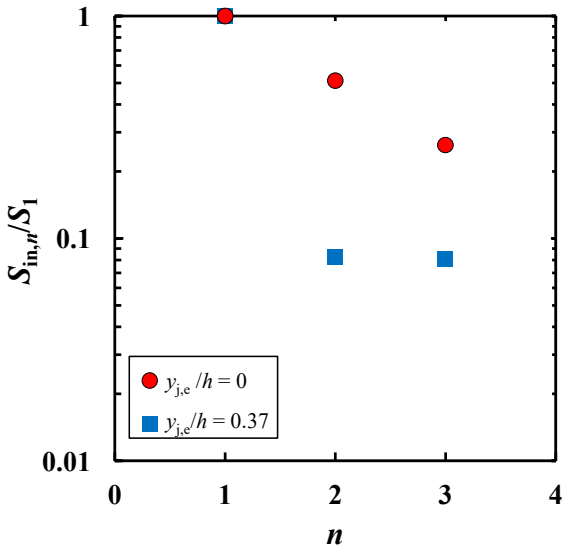

(b) Fourier transform

Figure 5.13 Temporal variations and Fourier transform of S_{in}, where S_0 is the reference value of S_{in}, $S_0 (\equiv U_0 h)$, and $S_{\text{in},n}$ is the nth mode of S_{in}. ($\theta_{\text{j}} = 39°, l / h = 5.6, Q = 16$ L/min)

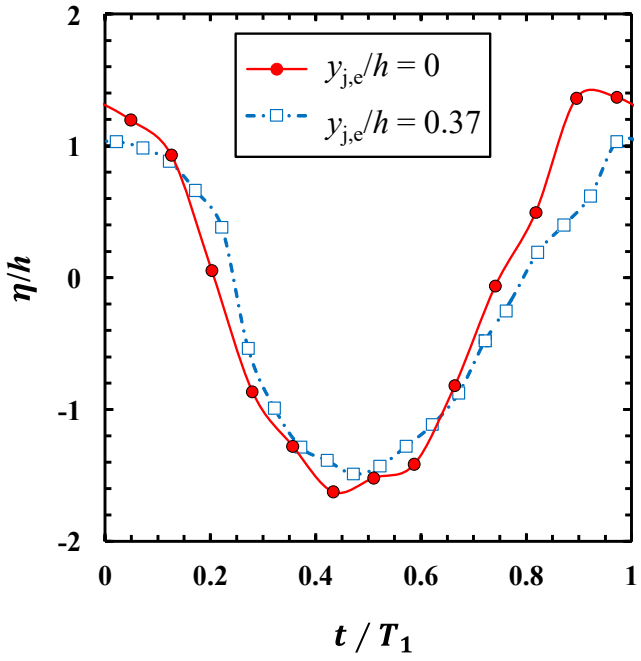

Figure 5.14 Temporal fluctuations of the jet displacement (η) at $x_j / h = 4$.

5.5. Discussion: Effects of Instantaneous Jet Direction on Jet Fluctuations

5.5.1. Jet Offset

To clarify the cause of flow separation in $y_{j,e} / h = 0.37$, Fig. 5.15 illustrates the instantaneous jet direction in the upstream for $y_{j,e} / h = 0$ and $y_{j,e} / h = 0.37$ while the jet changes its direction from inward to outward. The fluctuation angle of jet is estimated to be about $20°$ from the jet amplitude at $x_j / h = 2$. The shaded area shows the jet fluctuation area when the jet fluctuates inward and outward by $20°$ around the jet fluctuation center. Figure 5.15 shows that, when the jet deflects inward at the same angle within the jet fluctuation area, the jet hits a higher position on the inner wall of the edge in $y_{j,e} / h = 0.37$ than in $y_{j,e} / h = 0$. The distance from the jet blowout center to the wall is shorter in $y_{j,e} / h = 0.37$. The jet can be affected by the high pressure formed by the impingement of the jet to the wall from a more upstream position in $y_{j,e} / h = 0.37$ than in $y_{j,e} / h = 0$. Probably due to this effect, in $y_{j,e} / h = 0.37$, the flow is further

disturbed, resulting in the separation of the lower shear layer.

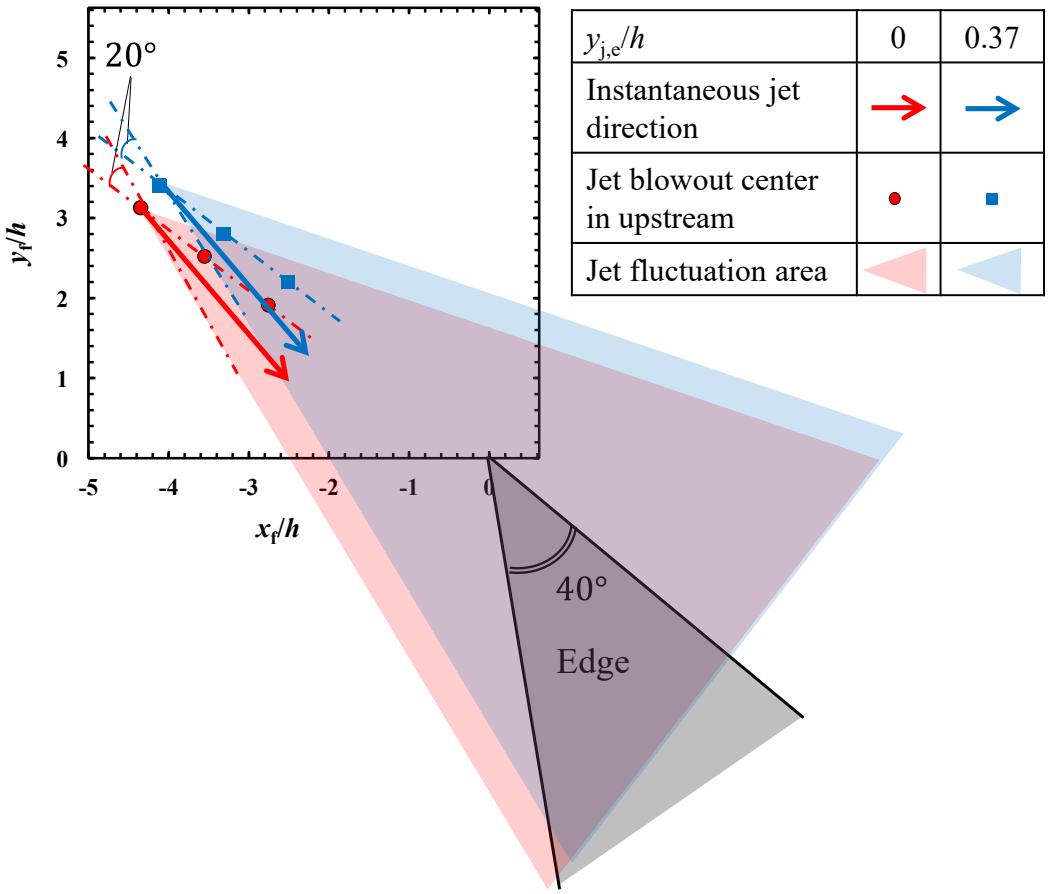

Figure 5.15 Schematic of instantaneous jet direction in upstream for $y_{j,e}/h = 0$ and $y_{j,e}/h = 0.37$ while the jet changes its direction from inward to outward. The shaded area shows the jet fluctuation area when the jet fluctuates inward and outward by $20°$ around the jet fluctuation center.

5.5.2. Jet Angle

In Chap. 4, the speed of the change in the jet direction from inward to outward decreases as the jet angle increases. To clarify the cause of this deceleration, Fig. 5.16 illustrates the instantaneous jet direction in the upstream for $\theta_j = 39°$, $50°$, and $65°$ when the jet deflects most inward in one cycle. The jet fluctuation area is estimated by the same way as in Sec. 5.5.1. As the jet angle increases, the jet direction approaches the

inner wall of edge. The vertical fluctuation of jet decelerates probably due to the heigh pressure near the wall. As a result, $|d^2\xi / dt^2|$ at the moment when the jet changes its direction from inward to outward decreases as the jet angle increases.

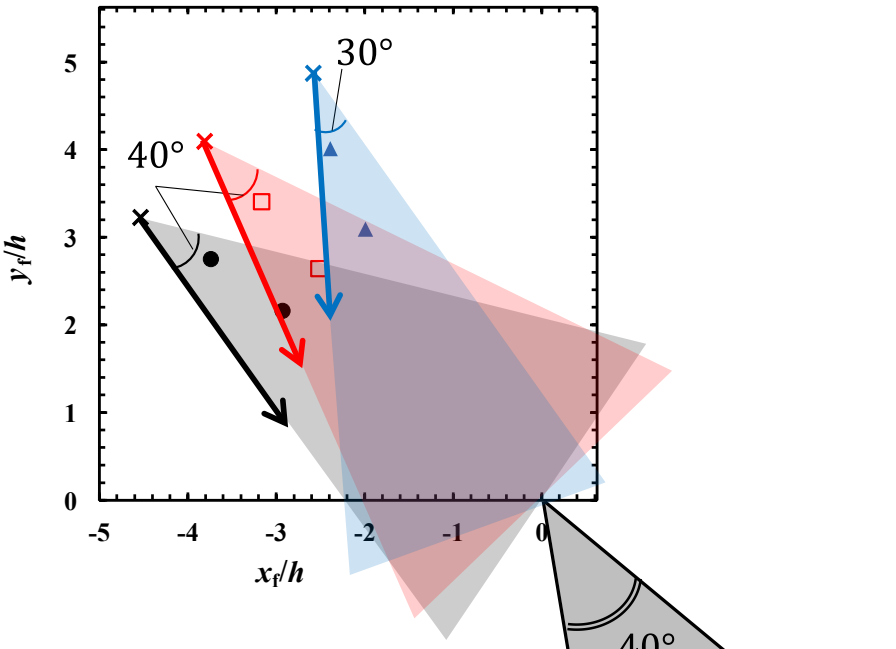

θ_j[°]	39	50	65
Instantaneous jet direction	→	→	→
Jet blowout center (estimated)	×	×	×
Jet fluctuation center (measured)	●	□	▲
Jet fluctuation area	◀	◀	◀

Figure 5.16 Schematic of instantaneous jet direction in upstream for $\theta_j = 39°$, 50°, and 65° when the jet deflects most inward in one cycle.

5.6. Conclusion

To clarify the effects of the geometrical relationship between the jet direction and the edge on the jet fluctuations and the sound, direct aeroacoustic simulations on the flute were performed. Under the conditions of the two jet offsets (the relative height of the jet to the edge) investigated, the absolute values of actual jet offset are almost the same for the two jet offsets but the harmonic structure of the radiated sound and the jet direction to the edge were different.

The temporal fluctuation of flow rate entering the resonator was found to consistent with the radiated sound, where the amplitudes and the relative amplitude of the second to the third mode are larger in the smaller jet offset. Even though the actual jet offset does not change, the flow rate entering the resonator changes, and thus the harmonic structure changes.

The flow rate entering the resonator depends on the temporal jet fluctuations, which is affected by the geometrical relationship between the jet and the edge. The jet visualization showed that the shear layer of the jet is separated in the larger jet offset probably during this shear layer crosses the edge. Due to the separation, over one cycle, the lower side of the jet in the downstream is disturbed more in the larger jet offset than in the smaller jet offset. The separated lower shear layer was found to go straight without fluctuating. This implies that this layer is affected little by the fluctuation in the upstream. Since this flow is not fluctuating, the amplitude of entire jet becomes small, the higher modes of fluctuation are suppressed. As a result, the amplitude of the flow rate becomes small in the larger jet offset. Also, in the smaller jet offset, the flow rate fluctuation was found to have the second peak around when the jet passes the edge, which results in the predominance of the second mode in the flow rate. This second peak is produced possibly due to a reverse flow caused by the jet impinges on the edge without being disturbed. From these, the flow separation seems to affect the temporal fluctuation of flow rate.

To clarify the cause of flow separation, the geometrical relationship between the instantaneous jet direction and the edge was investigated. Based on this relationship, as

the jet offset increases, the jet impinges on the inner wall of edge in a shorter distance, where the jet is expected to be affected by the high pressure around the edge wall from a more upstream position. As a result, the jet is disturbed more, resulting in the separation.

Based on the geometrical relationship, the cause of the deceleration of vertical fluctuation of jet with the jet angle, observed in Chap. 4, was also investigated. When the jet deflects inward, the distance between the jet and the inner wall of edge is estimated to decrease as the jet angle increases. The vertical fluctuation of jet decelerates probably due to the heigh pressure near the wall.

Due to the effects of the wall, the jet fluctuation changes, resulting in a change of the harmonic structure. To clarify the cause of the change of the jet fluctuation, estimation of the geometrical relationship between the instantaneous jet direction and the edge inclination seems to be useful.

6. Conclusion

The objective of this study was to elucidate the mechanism by which the radiated sound changes with various conditions of blowing and the instrument's shapes. Focusing on the interaction between the airflow and the sound of flute-like instruments, the following findings were presented.

Analysis for Sound Change Mechanism: Formulation and Quantification of Jet Fluctuations by Direct Aeroacoustic Simulations

An analytical method for quantifying jet fluctuation characteristics was proposed to determine which of condition of blowing and shapes mainly contribute to a sound change under conditions where multiple parameters change simultaneously. The jet fluctuations of the first and the second mode in two recorders were decomposed into the acoustic and the fluid dynamic oscillations, and their characteristics (the convection velocity, the amplification rate, the acoustic feedback effects, and the actual jet offset) were quantified. This analytical method was found to be useful for investigating sound change mechanisms.

Effects of Jet Angle on Harmonic Structure and Jet Fluctuations in the Flute

The radiated sound showed that, within the practical range of the blowing parameters, the harmonic structure (SPL difference between the second and the third harmonic) varies markedly with the jet offset. Compared to the jet offset, the change of the harmonic structure with the jet angle was less; however, this change was almost equal with the change with the flow rate and comparably larger than the distance. The effect of the jet angle on timbre seems to be an important consideration for flute players. The flow field showed that the jet fluctuation center (time-averaged jet displacement) inclines inward with increasing the jet angle. This inclination seems to occur because of the deceleration

of the fluctuation of jet when changing direction from inward to outward. The variation of the harmonic structure with the jet angle is mainly caused by the change of the actual jet offset due to the inclination of the jet fluctuation center rather than the changes of fluctuating component of the jet.

Effects of Geometrical Relation Between Jet Direction and Edge on Jet Fluctuations and Sound

The geometrical relationship between the jet and the edge affects the position of the jet fluctuation center as well as the temporal jet fluctuation. Even if the actual jet offset (the relative height of the temporal mean position of the jet fluctuation to the edge) does not change, the harmonic structure changes due to the changes of the temporal jet fluctuation. To clarify the cause of changes of jet fluctuations, estimating the instantaneous jet direction seems to be useful to understand the effects of the edge wall on the jet.

In conclusion, this study presented knowledge for elucidating the mechanism of the sound change. The followings are future works that require the further development of research on flute-like instruments.

- Measurements of player's techniques for changing sound

  In addition to the findings of this study, investigating which/how much blowing parameters professional players change with musical requirements may allow a scientific explanation of playing methods.

- Elucidation of noise generation mechanism

  When playing flute-like instruments, especially the flute and shakuhachi, noise is also generated. Although this study focuses on the fundamental tome and their harmonics, investigations on noise generation mechanism seem to be useful to control the sound.

Bibliography

1. R. Maeda. *Huruto no shozo – so no rekisiteki hensen* (in Japanese) [Portrait of flute - Its historical changes]. Tokyo shoseki, Tokyo, 2006.
2. N. H. Fletcher and T. D. Rossing. *The physics of musical instruments*. 2nd edition, Springer verlag, New York, 1998.
3. H. Altès. *Célèbre méthode complete.* Millereau, Paris, 1880 (reprinted by Alphonse Leduc, Paris, 2005).
4. W. Trevor. *A practice book for the flute.* Omnibus edition, Novello publishing Ltd., 2015.
5. T. Boehm. *The flute and flute-playing* (translated by D. C. Miller with a new introduction by S. Baron. Dover, New York, 1964, reprinted in 2011).
6. A. Michalke. On spatially growing disturbances in an inviscid shear layer. *J. Fluid Mech.* **23**, 521-544, 1965.
7. P. Freymuth. On transition in a separated laminar boundary layer. *J. Fluid Mech.* **25**, 683-704, 1966.
8. J. W. Coltman. Sounding mechanism of the flute and organ pipe. *J. Acoust. Soc. Am.* **44**, 983-992, 1968.
9. N. H. Fletcher. Sound production by organ flue pipes. *J. Acoust. Soc. Am.* **60**(4), 926-936, 1976.
10. N. H. Fletcher and S. Thwaites. Wave propagation on an acoustically perturbed jet. *Acustica* **42**(5), 323-334, 1979.
11. S. Yoshikawa, H. Tashiro, Y. Sakamoto. Experimental examination of vortex-sound generation in an organ pipe: A proposal of jet vortex-layer formation model. *J. Sound and Vib.* **331**, 2558-2577, 2012.
12. N. H. Fletcher and Lorna M. Douglas. Harmonic generation in organ pipes, recorders, and flutes. *J. Acoust. Soc. Am.* **68**(3), 767-771, 1980.

13. R. Auvray, A. Ernoult, and B. Fabre. Time-domain simulation of flute-like instruments: Comparison of jet-drive and discrete-vortex models. *J. Acoust. Soc. Am*. **136**, 389-400, 2014.
14. A. H. Benade. *Fundamentals of musical acoustics*. 2nd edition, Dover, New York, 1990.
15. J. W. Coltman. Jet drive mechanism in edge tones and organ pipes. *J. Acoust. Soc. Am.* **60** (3), 725-733, 1976.
16. B. Fabre. Flute-like instruments, in *Acoustics of musical instruments* (edited by A. Chaigne, J. Kergomard), Chap. 10. Springer Verlag, New York, 2016.
17. B. Fabre, J. Gilbert, A. Hirschberg, and X. Pelorson. Aeroacoustics of musical instruments. *Ann. Rev. Fluid Mech*. **44**, 1-25, 2012.
18. L. Rayleigh. *The theory of sound,* Vol. 2, Chap. 21. 2nd edition, Macmillan, New York, 1894 (reprinted by Dover, New York, 1945).
19. M. P. Verge, R. Caussé, B. Fabre, A. Hirschberg, A. P. J. Wijnands, and A. van Steenbergen. Jet oscillations and jet drive in recorder-like instruments. *Acta Acust.* **2**, 403-419, 1994.
20. P. de la Cuadra. The sound of oscillating air jets: Physics, modeling and simulation in flute-like instruments. Ph.D. thesis, Stanford university, 2005.
21. S. Thwaites and N. H. Fletcher. Wave propagation on turbulent jets. *Acustica* **45**, 175-179, 1980.
22. S. Thwaites and N. H. Fletcher. Wave propagation on turbulent jets: II Growth. *Acustica* **51**, 44-49, 1982.
23. S. Yoshikawa. Jet-wave amplification in organ pipes. *J. Acoust. Soc. Am.* **103**(5), 2706-2717, 1998.
24. M. P. Verge, B. Fabre, A. Hirschberg and A. P. J. Wijnands. Sound production in recorder-like instrument. I- Dimensionless amplitude of the internal acoustic field. *J. Acoust. Soc. Am*. **101**, 2914-2924, 1997.

25. M. P. Verge, B. Fabre, W. E. A. Mahu, A. Hirschberg, R. R. van Hassel, and A. P. J. Wijnands. Jet formation and jet velocity fluctuations in a flue organ pipe. *J. Acoust. Soc. Am*. **95**, 1119-1132, 1994.
26. R. Auvray and B. Fabre. Specific features of a stopped pipe blown by a turbulent jet: Aeroacoustics of the panpipes. *J. Acoust. Soc. Am*. **139**, 3214-3225, 2016.
27. M. P. Verge, A. Hirschberg, and R. Caussé. Sound production in recorderlike instruments. II. A simulation model. *J. Acoust. Soc. Am.* **101**(5), 2925-2939, 1997.
28. S. Terrien, R. Blandin, C. Vergez and B. Fabre. Regime change thresholds in flute-like instruments: influence of the mouth pressure dynamics. *Acta Acust.* **101**(2), 300-316, 2015.
29. S. Terrien, C. Vergez and B. Fabre. Flute-like instruments: a toy model investigated through numerical continuation. *J. Sound Vib.* **332**(15), 3833-3848, 2013.
30. R. Auvray, B. Fabre and P.-Y. Lagée. Regime change and oscillation thresholds in recorder-like instruments. *J. Acoust. Soc. Am*. **131**(2), 1574-1585, 2012.
31. J. W. Coltman. Time-domain simulation of the flute. *J. Acoust. Soc. Am*. **92**(1), 69-73, 1992.
32. H. Yokoyama, A. Miki, H. Onitsuka, and A. Iida. Direct numerical simulation of fluid-acoustic interactions in a recorder with tone holes. *J. Acoust. Soc. Am.* **138**, 858-873, 2015.
33. H. Yokoyama, R. Hamasuna, A. Miki, H. Onitsuka, and A. Iida. Direct aeroacoustic simulation related with mode change in a recorder. Proc. European Congress on Computational Methods in Applied Sciences and Engineering, 1315-1324, 2016.
34. K. Onogi, H. Yokoyama, and A. Iida. Analysis of jet oscillations with acoustic radiation in the recorder by direct aeroacoustic simulations. *J. Acoust. Soc. Am.* **146**, 1427−1437, 2019.
35. N. Giordano. Simulation studies of a recorder in three dimensions. *J. Acoust. Soc. Am.* **135**(2), 906-916, 2014.

36. N. Giordano. Computational study of the piccolo: Evidence for chaotic tones. *J. Acoust. Soc. Am.* **140**(3), 1887-1893, 2016.
37. M. Miyamoto, Y. Ito, T. Iwasaki, T. Akamura, K. Takahashi, T. Takami, T. Kobayashi, A. Nishida, and M. Aoyagi, Numerical study on acoustic oscillations of 2D and 3D flue organ pipe like instruments with compressible LES. *Acta Acust.* **99** (1), 154-171, 2013.
38. Y. Ando. Drive conditions of a flute and their influences upon sound pressure level and fundamental frequency of generated tone: an experimental study of a flute I. *J. Acoust. Soc. Jpn*. **26**, 253−260, 1970.
39. K. Onogi, H. Yokoyama, and A. Iida. Effects of jet angle on harmonic structure of sound radiating from the flute. *Acta Acust*. **5**(11), 2021.
40. Y. Ando. *Shimban gakki no onkyogaku* (in Japanese) [New edition: Acoustics of musical instruments]. Ongaku no tomo sha, Tokyo, 1996.
41. J. W. Coltman. Resonance and Sounding Frequencies of the Flute. *J. Acoust. Soc. Am.* **40**(1), 99-107, 1966.
42. Y. Ando. Drive conditions of a flute and their influences upon harmonic structure of generated tone: an experimental study of a flute II. *J. Acoust. Soc. Jpn.* **26**, 297−305, 1970.
43. N. H. Fletcher. Nonlinear interactions in organ flue pipes. *J. Acoust. Soc. Am.* **56**(2), 645-652, 1974.
44. C. Ségoufin, B. Fabre, M. P. Verge, A. Hirschberg and A.P. J. Wijnands. Experimental Study of the Influence of the Mouth Geometry on Sound Production in a Recorder-like Instument: Windway Length and Chamfers. *Acta Acust.* **86**, 649-661, 2000.
45. Y. Sawada and S. Sakaba. On the transition between the sounding modes of a flute. *J. Acoust. Soc. Am.* **67**, 1790-1784, 1980.

46. D. Ferrand, C. Vergez, B. Fabre and F. Blanc. High-precision regulation of a pressure controlled artificial mouth: the case of recorder-like musical instruments. *Acta Acust.* **96**(4), 701-712, 2010.
47. A. Ernoult and B. Fabre. Window Impedance of Recorder-Like Instruments. *Acta Acust*. **103**, 106-116, 2017.
48. A. Ernoult, P. de la Cuadra and B. Fabre. An Inclined Plane: A Simple Model for the Acoustic Influence of the Flutist's Face. *Acta Acust.* **104**, 496-508, 2018.
49. J. -P. Dalmont, C. J. Nederveen, and N. Joly. Radiation impedance of tubes with different flanges: numerical and experimental investigations. *J. Sound and Vib*. **244**(3), 505-534, 2001.
50. J. W. Coltman. Acoustics of the flute. *Phys. Today* **21**(11), 25-32, 1968.
51. N. H. Fletcher. The nonlinear physics of musical instruments. *Rep. Prog. Phys.* **62** 723-764, 1999.
52. N. H. Fletcher. Acoustical correlates of flute performance technique. *J. Acoust. Soc. Am.* **57**(1), 233-237, 1975.
53. I. Cossette, B. Fabre, V. Fréour, N. Mountgermont and P. Monaco. From breath to sound: linking respiratory mechanics to aeroacoustic sound production in flutes. *Acta Acust.* **96**, 654-667, 2010.
54. C. Vauthrin, B. Fabre, and I. Cossette. How does a flute player adapt his breathing and playing to musical tasks?. *Acta Acust*. **101**, 224-237, 2015.
55. T. Shakouchi. *Hunryu kogaku – Kiso to oyo* (in Japanese) [Jet flow engineering – Fundamentals and application]. Morikita publishing, Tokyo, 2004.
56. W. K. Blake. Shear layer instability, flow tones and jet, in *Mechanics of Flow-Induced Sound and Vibration*, Vol. I, Chap. 3. Academic Press, 1986.
57. P. Freymuth. Diss. Technische Universität Berlin, 1965.
58. G. E. Mattingly and W. O. Criminale, Jr. Disturbance characteristics in a plane jet. *Phys. Fluids* **14**(11), 2258–2264, 1971.

59. S. Yoshikawa. Fluid dynamic model for wind instrument, in *Aeroacoustics of sound sources* (edited by S. Yoshikawa and H. Wada), Chap. 7. Corona, Tokyo, 2007.
60. S. Yoshikawa, J. Saneyoshi. Feedback excitation mechanism in organ pipes. *J. Acoust. Soc. Jpn.* (E)**1**, 175-191, 1980.
61. M.P. Verge. Aeroacoustics of confined jets: with application to the physical modeling of recorder-like instruments. Ph.D. thesis, Eindhoven University of technology, 1995.
62. A. Powell. On edge tones and associated phenomena. *Acustica* **3**, 233-243, 1953.
63. P. de la Cuadra, C. Vergez and B. Fabre. Visualization and analysis of jet oscillation under transverse acoustic perturbation. *J. Flow Vis Image Process*. **14**(7), 355−374, 2007.
64. P. G. Drazin and L. N. Howard. Hydrodynamic stability of parallel flow of inviscid fluid. *Adv. Appl. Mech*. **9**, 1-89, 1966.
65. P. Savic. On acoustically effective vortex motion in gaseous jets. *Phil. Mag*. **32**, 245-252, 1941.
66. A. A. Townsend. *The structure of turbulent shear flow*. Cambridge univ. press, Cambridge, 1956.
67. C. Ségoufin, B. Fabre and L. de Lacombe. Experimental investigation of the flue channel geometry influence on edge-tone oscillations. *Acta Acoustica* **90**, 966-975, 2004.
68. B. Fabre and A. Hirschberg. Physical modeling of flue instruments: a review of lumped models. *Acta Acust*. **86**, 599-610, 2000.
69. S. A. Elder. On the mechanism of sound production in organ pipes. *J. Acoust. Soc. Am.* **54**, 1554-1564, 1973.
70. H. Helmholtz. *On the Sensations of Tone* (translated by A. J. Ellis). Springer, 1863 (reprinted by Dover, New York, 1954).
71. N. H. Fletcher. Jet drive mechanism in organ pipes. *J. Acoust. Soc. Am.* **60**, 481-483, 1976.

72. S. Yoshikawa. Vortices on sound generation and dissipation in musical flue, in *Vortex Dynamics Theories and Applications* (edited by Z. Harun), Chap. 3, IntechOpen, London, 2020.
73. L. Cremer and H. Ising. Die selbsterregten Schwingungen von Orgelpfeifen (in German) [The self-excited oscillation of organ pipes]. *Acustica* **19**(3), 143-153, 1967.
74. S. Thwaites and N. H. Fletcher. Acoustic admittance of organ pipe jets. *J. Acoust. Soc. Am.* **74**(2), 400-408, 1983.
75. J. W. Coltman. Flute scales - pitch and intonation. *The Instrumentalist*, 1976.
76. J. W. Coltman. Momentum transfer in jet excitation of flute-like instruments. *J. Acoust. Soc. Am.* **69**, 1164-1168, 1981.
77. S. Dequand, J. F. H. Willems, M. Leroux, R. Vullings, M. van Weert, C. Thieulot, and A. Hirschberg. Simplified models of flue instruments: Influence of mouth geometry on the sound source. *J. Acoust. Soc. Am*. **113**(3), 1724-1735, 2003.
78. DK. Holger, TA. Wilson, and GS. Beavers. Fluid mechanics of the edgetone. *J. Acoust. Soc. Am*. **62**(5), 1116-1128, 1977.
79. DK. Holger, TA. Wilson, and GS. Beavers. The amplitude of edgetone sound. *J. Acoust. Soc. Am*. **67**(5), 1507-1511, 1980.
80. M. S. Howe. Contributions to the theory of aerodynamic sound, with application to excess jet noise and the theory of the flute. *J. Fluid Mech.* **71**(4), 625-673, 1975.
81. M. Meissner. Aerodynamicaly excited acoustic oscillations in cavity resonator exposed to an air jet. *Acta Acust.* **88**, 170-180, 2002.
82. M. S. Howe. The dissipation of sound at an edge. *J. Sound Vib*. **70**(3), 407-411, 1980.
83. M. P. Verge, B. Fabre, W. E. A. Mahu, A. Hirschberg, R. van Hassel, A. P. J. Wijinands, J.J. de Vries, and C.J. Hogendoorn. Jet formation and jet velocity fluctuations in a flue organ pipe. *J. Acoust. Soc. Am.* **95**, 1119-1132, 1994.

84. B. Fabre, A. Hirschberg, and A. P. J. Wijnands. Vortex shedding in steady oscillation of a flue organ pipe. *Acta acust.* **82**, 863-877, 1996.

85. U. Ingard and H. Ising. Acoustic nonlinearity of an orifice. *J. Acoust. Soc. Am.* **42**, 6-17, 1967.

86. B. Fabre. La production de son dans les instruments à embouchure de flûte: modèle aéro-acoustique pour la simulation temporelle (in French). Ph.D. thesis, Université du Maine, le Mans, France, 1992.

87. S. Yoshikawa. Harmonic generation mechanism in organ pipes. *J. Acoust. Soc. Jpn.* (E)**5**(1), 17-29, 1984.

88. J. W. Coltman. Jet offset, harmonic content, and warble in the flute. *J. Acoust. Soc. Am.* **120**(4), 2312-2319, 2006.

89. W. G. Bickley. The plane jet. *Philos. Mag. J. Science* **23**, 727-731, 1937.

90. P. Angot, C. H. Bruneau, and P. Frabrie. A penalization method to take into account obstacles in viscous flows. *Numer. Math*. **81**, 497–520, 1999.

91. Q. Liu and O. V. Vasilyev. A Brinkman penalization method for compressible flows in complex geometries. *J. Comp. Phys*. **227**, 946–966, 2007.

92. R. Mittal and G. Iaccarino. Immersed boundary methods. *Annu. Rev. Fluid Mech*. **37**, 239–261, 2005.

93. S. K. Lele. Compact finite difference schemes with spectral-like resolution. *J. Comp. Phys.* **103**, 16-19, 1992.

94. A. Jameson, T. J. Baker. Solution of the Euler equations for complex configurations. *AIAA Paper* 83-1929, 293-302, 1983.

95. K. Matsuura and C. Kato. Large-eddy simulation of compressible transitional flows in a low-pressure turbine cascade. *AIAA J.* **45**, 442-457, 2007.

96. D. V. Gaitonde and M. R. Visbal. Pade-type higher-order boundary filters for the Navier-Stokes equations. *AIAA J*. **38**, 2103–2112, 2000.

97. T. Colonius, S. K. Lele, and P. Moin. Boundary conditions for direct computation of aerodynamic sound generation. *AIAA J.* **31**(9), 1574-1582, 1993.

98. K. W. Thompson. Time dependent boundary conditions for hyperbolic systems. *J. Comp. Phys.* **68**, 1-24, 1987.
99. T. J. Poinsot and S. K. Lele. Boundary conditions for direct simulations of compressible viscous flows. *J. Comp. Phys.* **101**, 104-129, 1992.
100. J. W. Kim and D. J. Lee. Generalized characteristic boundary conditions for computational aeroacoustics. *AIAA J.* **38** (11), 2040-2049, 2000.
101. T. Matsuno, S. Honami, K. Fujii, S. Sekimoto, and A. Iida. Flow measurement technique. *J. Plasma Fusion Res*. **91**, 661-664, 2015.
102. K. Arimoto. Experimental study on the temporal fluctuation of harmonics in flute sounds. Proc. International Symposium on Music Acoustics, 2019.
103. N. H. Fletcher. Stopped-pipe wind instruments: acoustics of the panpipes. *J. Acoust. Soc. Am.* **117**, 370-374, 2005.